Xinying Zhu

Application of the CIP Method to Strongly Nonlinear Wave-Body Interaction Problems

Doctoral thesis
for the degree of doktor ingeniør

Trondheim, February 2006

Norwegian University of
Science and Technology
Faculty of Engineering Science and Technology
Department of Marine Technology

NTNU
Innovation and Creativity

NTNU
Norwegian University of Science and Technology

Doctoral thesis
for the degree of doktor ingeniør

Faculty of Engineering Science and Technology
Department of Marine Technology

ISBN ISBN 82-471-7813-3 (printed ver.)
ISBN ISBN 82-471-7812-5 (electronic ver.)
ISSN 1503-8181

Doctoral Theses at NTNU, 2006:35

Printed by Tapir Uttrykk

Abstract

Water entry and exit, green water on deck, sloshing in tanks and capsizing in intact and damaged conditions are examples on violent fluid motion. The combination of model tests, theoretical analysis and Computational Fluid Dynamics (CFD) methods is emphasized in treating these problems. Because mixing of air and liquid may occur, the interaction between the flow in the air and in the liquid ought to be considered in numerical simulations. Further, the mixing of air and liquid represents a scaling problem of model tests.

In order to make a rational step in improving the analysis of nonlinear wave-induced ship motions and loads, it is necessary to base a solution on the Navier-Stokes equations, i.e. a CFD method has to be used. The Constrained Interpolation Profile (CIP) method described in this thesis is used as a CFD method for exterior water-body interaction studies. Because it is a rather new method, careful validation and verification are needed. This includes linear flow cases and sub-problems associated with large amplitude water entry and exit.

In this method, the solid body and free surface interaction is treated as a multiphase problem, which includes liquid (water), gas (air) and solid (rectangular cylinder, circular cylinder, bow flare section, V-shaped section, etc.) phases. The flow is represented by one set of governing equations, which are solved numerically on a non-uniform, staggered Cartesian grid by a finite difference method. The free surface as well as the body boundary is immersed in the computational domain.

First of all, linear and weakly nonlinear wave-body interaction problems are investigated by using a CIP-based finite difference method. The numerical wave tank (NWT) encounters difficulties in handling the long time simulation of large amplitude motions. Therefore, the wave-body interaction problem is isolated into water entry and water exit sub-problems.

This thesis describes the fully nonlinear free-surface deformations of initially calm water caused by water-entry and water-exit of a horizontal circular cylinder with both forced and free vertical motions. This has relevance for marine operations as well as for the ability to

predict large amplitude motions of floating sea structures. The numerical results of the water entry and exit force, the free surface deformation and the vertical motion of the cylinder are compared with experimental results, and favorable agreement is obtained.

The CIP method is also applied to 2D water entry of vertical and heeled bow flare and V-shaped sections. The results for the bow flare section have relevance for slamming loads on a ship in bow sea with large roll oscillations and relative vertical motions. The results for the heeled V-shaped section can be combined with a 2D+t numerical method to study how the steady heel moment on a prismatic planing hull on a straight course in calm water depends on the Froude number (Faltinsen, 2005). A generally satisfactory agreement with experimental drop test results of vertical water entry velocity, vertical and horizontal hydrodynamic forces as a function of time is demonstrated. This includes the effect of flow separation from the knuckles. The experimental results have bias errors due to eigenfrequency oscillations of the test rig and the use of elastic ropes to stop the models. The occurrence of ventilation of the leeward hull side is examined.

An example on 3D calculations by means of the CIP method is presented. Green water on the deck of a Wigley hull at Froude number 0.25 in head sea is studied.

Our studies are a step towards developing rational CFD methods for predicting strongly nonlinear wave-induced motions and loads on a ship.

Acknowledgements

This work is carried out under the patient guidance of my supervisor Prof. Odd M. Faltinsen at the Department of Marine Technology, Norwegian University of Science and Technology. I must thank him for his great contributions to this thesis. His guidance covers not only controlling the main direction of the thesis but also a lot of useful suggestions and discussions. I cannot imagine how to finish this thesis without his supervision.

I must thank Prof. Changhong Hu at RIAM, Kyushu University who was a visiting professor at CeSOS, NTNU for one year. He helps me a lot during his stay in Trondheim in developing the 2D code by using the CIP method. Helpful discussions with him are very much appreciated.

My friends and colleagues at the Department of Marine Technology give me a lot of help during my life and study in NTNU. Special thanks give to those Chinese friends. They make me feel at home.

I am indebted to my parents and my brother for their selfless support of my study in Norway.

This work was supported by Research Council of Norway through the Project - *BeMatA* at MARINTEK.

Nomenclature

General Rules

- Only the most used symbols are listed in the following sections
- Meaning of symbols is given at least when introduced in the thesis
- Sometimes the same symbol is used to indicate different things

Subscripts

max	Maximum
min	Minimum

Roman Letters

A	Submerged cross-sectional area
A_{33}	Heave added mass
B_{33}	Heave damping coefficient
B	Breadth
C_A	Added mass coefficient
C_D	Drag coefficient
Ce	Exit coefficient
C_g	Group velocity
C_M	Inertia coefficient
Cs	Slamming coefficient

Cs_b	Slamming coefficient due to buoyancy
C_w	Phase velocity = $\lambda/T = \omega/k$
D	Draft/Diameter
Eu	Euler number
F_i	Hydrodynamic force component
F_x	Horizontal force
F_z	Vertical force
Fn	Froude number
g	Gravitational acceleration
h	Water depth
I	inertial moment per unit length
H	Incoming wave height; Drop height
k	wave number $=2\pi/\lambda$
L	Ship length
m	Mass per unit length
M	Roll moment
$\vec{n}$	Normal unit vector
p	Pressure
p_a	Atmospheric pressure
R	radius of circular cylinder
Re	Reynolds number
t	Time
T	Period
T_w	Wave period
u	Horizontal velocity component
v	Vertical velocity component
U	Horizontal impact velocity component
V, W	Vertical impact velocity component
x	Horizontal axis
y, z	Vertical axis
(x_c, z_c)	Mass centre of the floating body
Z_a	Amplitude of heave motion

Greek Letters

α	Sharpness enhancement parameter; Roll angle
β	Heel angle; CFL number
Δx	Horizontal spatial grid size in x-direction
Δy	Vertical spatial grid size in y-direction
Δt	Time step
ε	Small positive constant
η_3	Heave motion
η_{3a}	Amplitude of heave motion
λ	Wave length
μ	Dynamic viscosity coefficient

ν	Kinematic viscosity coefficient
ρ	Density of water, air, solid body, etc.
φ	Velocity potential
φ_m	Color function
Φ	Transformation function
ω	Frequency (rad/s); Acceleration coefficient in SOR method
Ω	Computational domain

Abbreviations

1D	One dimensional
2D	Two dimensional
3D	Three dimensional

Content

CHAPTER 1

Introduction

1.1 Background and motivation

Green water on deck, water impact, sloshing in tanks and capsizing in intact and damaged conditions are examples on violent fluid motions in marine hydrodynamics, see Figure 1.1.

(a) Green water and water impact on floating structures.

(b) Sloshing in tanks.

(c) Platform P-36: capsizing in damaged conditions.

Figure 1.1 Examples on violent fluid motions in marine hydrodynamics.

The green water problem arises when a ship, usually in harsh weather conditions, encounters waves that exceed the freeboard and wet the deck (Nielsen, 2003). Many researchers have investigated the green water problem both experimentally and by the use of various numerical models. With the introduction of floating production storage and offloading units (FPSOs) and floating storage units (FSUs) in the offshore industry, the problem of green water loads has been given increasing attention, and the effort to install FPSOs in yet harsher environments has increased the problems related to green water incidents (Ersdal & Kvitrud, 2000).

For the analysis of sloshing in ship tanks, one of the major concerns in the marine hydrodynamic field is the accurate prediction of impulsive load on internal structures (Kim, 2000). During violent sloshing, the sloshing-induced impact load can cause a critical damage on the tank structure. Such damage cases have been reported for oil tankers, LNG carriers and bulk carriers. Since 1970's, the sloshing problem has been an important issue in the design of the liquefied natural gas (LNG) carriers. Recently, this problem also became an important issue in FPSO design.

Capsizing of ships leads to a primary group of casualties, including loss of life and money. Despite today's advanced technology, it is difficult to build non-capsizing ships because of the fact that it is impossible to model and simulate the environment mathematically with all its aspects (Taylan, 2003). The random, unpredictable and sometimes chaotic character of the ocean environment is responsible for capsizes and loss of life. Many legal and scientific investigations have been carried out to find the causes of the disaster. Unfortunately, the exact causes of the incident still remain a mystery.

Therefore, it is necessary to estimate quantitatively and precisely the wave loads during the fully nonlinear wave-body interactions. Experiments are the most practical but expensive way. A major difficulty of the numerical simulations arises from the extremely complicated hydrodynamic phenomena, for instance, the highly distorted or broken free surface, the effect of the compressibility of water/air or the elasticity of the body in the case of water impact. A combination of model tests, theoretical analysis and Computational Fluid Dynamics (CFD) is needed to describe the phenomena mentioned above. Because mixing of air and liquid may occur, the interaction between the flow in the air and in the liquid ought to be considered in numerical simulations. Further, the mixing of air and liquid represents a scaling problem for model tests.

In order to make a rational step in improving the analysis of nonlinear wave-induced ship motions and loads, it seems necessary to base a solution on the Navier-Stokes equations, i.e. a CFD method has to be used. Even though there may be a long wait for the computational power needed to simulate the stochastic effect of a sea state, this should not prevent research groups from starting the process. Careful validation and verification are needed. This should include linear flow cases and sub-problems associated with large amplitude water entry and exit.

1.2 CFD methods

There are different types of CFD methods, which have been used to solve the above problems. Before breaking and fragmentation phenomena occur, and in the regions where the flow can be studied through a potential theory, the most efficient and accurate instrument is given by the use of the Boundary Element Method (BEM). After that more general field methods able to capture the post-breaking phase have to be considered.

CFD methods based on solving the Navier-Stokes equations such as the Smoothed Particle Hydrodynamics (SPH) method, the Constrained Interpolation Profile (CIP) method, and the finite difference methods in which the free surface is captured by the Volume of Fluid (VOF) method or the Level Set (LS) method are generally more robust than the BEM to solve violent fluid motion. Further, mixture between air and fluid may occur and viscous effects can be accounted for. However, the accuracy of a CFD method for different applications such as sloshing in tanks, green water on deck, slamming and large amplitude ship motion has to be documented. Important verification and validation tests of a CFD method include also how well it can predict linear fluid problems. CFD methods are still too time-consuming for practical strongly nonlinear 3D wave-ship interaction problems, requiring long time simulations to obtain probability density functions of response variables in a stochastic sea.

Both grid methods and gridless methods are used to solve the Navier-Stokes equations. The SPH method is an example on a gridless method where individual fluid particles are followed in time. The grid method can be classified into two categories:

- Lagrangian method (moving grid method)

  The boundary is treated explicitly without smearing information at the interface. The boundaries are fitted by the computational grid. The governing equations are solved on the boundary fitted grid. Boundary conditions are applied at the exact location of the free surface or rigid boundary. This method is quite efficient when the geometric variation is modest. However, it is very difficult and time consuming to generate the boundary grid of a strongly deforming free surface and arbitrarily moving bodies (Fekken, 2004). The Boundary Element Method applied to a strongly nonlinear problem is a special case of the Lagrangian method.

- Eulerian method (fixed grid method)

  Eulerian methods are suitable for surfaces with large deformations. The interface is not explicitly tracked but is reconstructed from the field variables of the fixed grid. The location of the interface is determined based on volume fraction information, resulting in uncertainty of about one grid cell. It is difficult to apply the boundary conditions at the exact location of the boundary, but the discretization is easy because no remeshing is needed (Fekken, 2004). Topological changes are easy to handle but some accuracy may be lost when details of the interface can not be covered by the grid. The interface is of a finite thickness but can be sharpened by various strategies. The VOF, LS and CIP methods use an Eulerian grid.

In the following, all the CFD methods mentioned above will be described briefly.

1.2.1 Boundary Element Method (BEM)

The Boundary Element Method has been successful in solving linear and second-order wave-body interaction problems dominated by potential flow. Good results have also been demonstrated in cases of strongly nonlinear and violent fluid motion. An example is the water entry studies by Zhao & Faltinsen (1993). Flow separation from chines can be accounted for, but it is more difficult to use a BEM to simulate non-viscous flow separation from curved surfaces happening during water entry. A BEM fails, for instance, when a plunging wave impacts on the underlying water. One reason is that vorticity is generated, i.e. there does not exist a velocity potential describing the fluid flow. However, there is the possibility to cut away the plunging wave part and continue the numerical solution with minor influence on the pressure distribution on the body. Moyo & Greenhow (2000) used BEM to study the fully non-linear inviscid-flow calculations of the deformations of an initially calm free surface caused by the free motion of a horizontal cylinder starting from rest from a prescribed depth. The calculations break down due to ventilation at the final stage. The cylinder is then above the initially calm water free surface with a thin layer of fluid on the upper cylinder surface and two (symmetric) regions with pressures lower than the atmospheric pressure on the lower cylinder surface. The resulting pressure inversion across the free surface immediately below the cylinder causes Rayleigh-Taylor instability and spontaneous free surface breaking of the type photographed by Greenhow & Lin (1983). This stops the numerical calculations.

1.2.2 Smoothed Particle Hydrodynamics (SPH) method

SPH is a particle method for the numerical simulation of Lagrangian hydroynamics. It is originally invented by Lucy (1977) and Gingold & Monaghan (1977) to simulate the fission of a rapidly rotating star and is extended to complicated free surface flows including solitary wave propagation over a planar beach (Monaghan & Kos, 1999), plunging breakers (Tulin & Landrini, 2000), solid bodies impacting on the water (Monaghan et al., 2003) and dam break simulations (Monaghan, 1994). In particle methods, the computational elements are not grid-cells as in finite difference methods, but moving points in space where computational data in the fluid is sampled. The motion of the particles is typically governed by the equations of the fluid. SPH is a Lagrangian method, which means that the particles follow the fluid flow. The particles carry all the computational information, so there is no computational grid. The particles themselves are the computational framework on which the fluid equations are solved. This makes the method easy to implement.

The main strength of SPH comes directly from its Lagrangian properties. It is easy to handle multi-dimensional problems and problems without any particular symmetry with SPH. SPH only performs calculations in the relevant regions, i.e. where the mass is located. No computational time will be spent in empty regions. It is relatively easy to include different physical processes in SPH. The equations retain their original mathematical form to a high degree. SPH is known to be a robust method and gives reasonable accuracy for a wide range of conditions. Even when a simulation evolves outside the domain where SPH is known to give valid solution, the method will not break down completely. Landrini et al. (2003) simulated the problem of sloshing in a tank by SPH and showed a favorable agreement with experiments as shown in Figure 1.2.

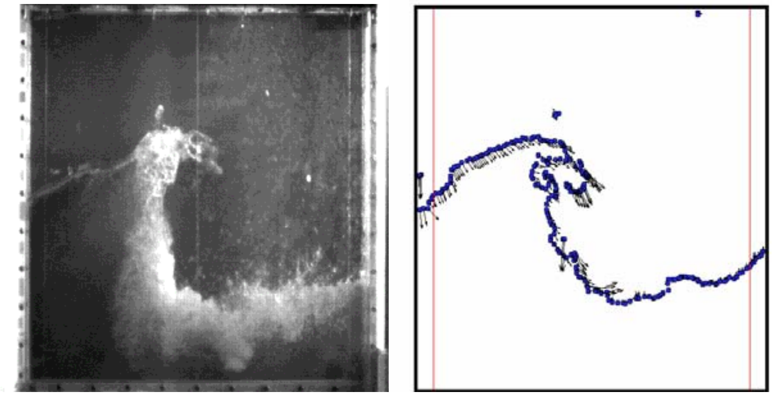

Figure 1.2 Experiment (left) and SPH simulations (right) of sloshing in a tank (Landrini et al., 2003).

However, boundary conditions are usually difficult to implement in SPH. Handling of boundaries does not come very naturally. Typically, it is difficult to prevent particles from penetrating boundaries. For complicated boundary conditions, SPH is not the method of choice; see Rogers et al. (2003). The easiest types of boundaries that can be handled by SPH are the natural boundaries far from the regions of interest where the density falls to zero and the periodic type conditions. SPH gives reasonable results for the first order gradient, but becomes worse for higher order derivatives. Special techniques need to be employed when the second and/or higher order derivatives are present in the physics. Another drawback is that the predicted pressure may contain unphysical oscillations due to the use of an artificial pressure-density relationship.

Monaghan (1988) described the application of SPH to a wide variety of problems in compressible gas flow. It is suggested that SPH is most effective in 3D calculations and least efficient in 1D, but the full effectiveness of SPH is yet to be determined. There is still a wide range of problems suitable for SPH treatment, although most of these problems are generally in the astrophysics field.

1.2.3 Volume of Fluid (VOF) method

Volume of Fluid (VOF) is a powerful numerical method developed by Nichols et al. (1980) and Hirt & Nichols (1981) to simulate the free surface flows. The VOF method uses an Eulerian approach and relies on the calculation of a scalar parameter (color function ϕ) representing the fractional volume of fluid in a numerical cell in order to track interface distortions. The color function is semi-discontinuous with values between one and zero and is advected according to the local flow velocity **u**

$$\frac{\partial \phi}{\partial t} + \mathbf{u} \cdot \nabla \phi = 0 \tag{1.1}$$

A filling process is used to determine which cell in the meshing volume is filled and which is emptied. The popularity of the scheme is based on its easy implementation, its accuracy and its computational efficiency.

Xing-Kaeding et al. (2004) studied the strongly nonlinear free-surface deformation during the water entry and exit of a horizontal circular cylinder by a viscous flow solver with the volume of fluid (VOF) method and got favorable agreement with the photographs of experiments. Kleefsman et al. (2004) solved wave impact problems by a numerical method based on the Navier-Stokes equations and by using an improved volume-of-fluid (VOF) method for the displacement of the free surface. Dam break problem and water entry and exit of 2D objects were compared with the experimental results to validate this method.

However, Eulerian VOF schemes have accuracy problems in the attempt to maintain local mass conservation, see Lafaurie et al. (1994). The reconstructed interface is not smooth or even continuous, lowering the accuracy of the geometrical information (normals and curvature) at the interface compromising the entire solution. Several researchers have worked to improve the accuracy of the VOF geometrical information using convolution of the color function with a kernel function, see e.g. Williams et al. (1999a, 1999b). James & Lowengrub (2004) used a surfactant-conserving volume-of-fluid method for interfacial flows with insoluble surfactant. The main advantages of this method are that the interface shape is not constrained, changes in topology are handled automatically, and mass of each flow component is conserved exactly. The interface location is captured by tracking the local volume fraction. The volume fraction is constant in each fluid and discontinuous at the interface. The volume fraction convection equation is solved in every cell, but is nontrivial only near an interface. To maintain the discontinuous nature of the volume fraction, care is taken not to introduce numerical diffusion when solving the equations. Numerical diffusion would cause smoothing of the discontinuity and the interface would become smeared normal to itself. The approach used to avoid this is to calculate the flux of one of the fluids across each cell face using a reconstruction of the interface position. The fluxes are then used to update the volume fraction to the next time step.

A number of techniques based on VOF have been developed for a number of applications, for instance, tracking water droplets caught in an air stream and polymer mould filling, see Rudman (1997). However, all these techniques have been developed for structured meshes and follow the finite-difference (FD) discretisation of the original scheme. Recently, attempts have been made to construct VOF schemes in Finite Element (FE) frameworks, which, however, employ secondary structured grids for the solution of the scalar advection equation for the tracking of the material interface, see Maronnier et al. (1999). Chirstakis et al. (2002) developed a new unstructured algorithm based on the VOF method for tracking material interfaces in a finite-volume framework.

1.2.4 Level Set (LS) method

The Level Set (LS) method, invented in 1987 by S. Osher and J.A. Sethian (see Osher & Sethian, 1988) has proved remarkably successful as a numerical (and theoretical) device in a host of applications including fluid mechanics, combustion, computer vision, and materials science, see Osher & Fedkiw (2001, 2002) and Sethian (1999, 2000). In the level-set method, a smooth function $\phi(x,t)$ called distance function or color function is introduced to denote the distance from x to the initial interface location at any instance. A particle on the level set evolves in time by the following transport equation

$$\frac{\partial \phi}{\partial t} + u_n \left|\nabla \phi\right| = 0 \tag{1.2}$$

where u_n is the normal velocity of the interface. Level Set methods have been widely used for capturing interface evolution especially when the interface undergoes extreme topological changes, e.g. merging or pinching off. Sussman (1994) used Level set methods to model multiphase immiscible incompressible flows. These methods are attractive because they admit a convenient description of topologically complex interfaces and are quite simple to implement. However, the numerical presentation of the transport equation to determine the values of the color function is prone to numerical error which leads to a loss or gain of mass. As documented in Gerrits (2001), the LS method has serious problems with mass conservation.

Enright et al. (2002) proposed a new method which combines the best properties of an Eulerian Level Set method and a marker particle Lagrangian scheme. This method randomly places a set of marker particles near the interface (defined by the zero level set) and allows them to passively advect with the flow. In fluid flows, particles do not cross the interface except when the interface capturing scheme fails to accurately identify the interface location. This method in Enright et al. (2002) was designed to track material interfaces for both incompressible and compressible flows where characteristics are not created or destroyed. In these instances, marker particles can be used to accurately track characteristic information without considering shocks and rarefactions where particles need to be created and destroyed in a consistent fashion. The particle level set method has not yet been extended to treat more complex flows such as those involving geometry, e.g. motion normal to the interface or motion by mean curvature. However, extending the particle level set method to treat the reinitialization equation is straightforward since the exact solution dictates that both the interface (zero level set) and the marker particles should sit still.

Landrini (2003) compared three CFD methods (BEM, SPH, LS) with experiments for 2D dam-breaking and water-wall impact problems to identify the disagreements among different tools; see Figure 1.3 which presents the time evolution of the water front toe after the dam break. The BEM simulation has to be stopped at the impact of the plunging wave with the underlying water, while the CFD methods are able to continue further on and predict rather similar shapes of the entrapped cavity and of the jet splash up caused by the water-water impact as in Figure 1.4 .

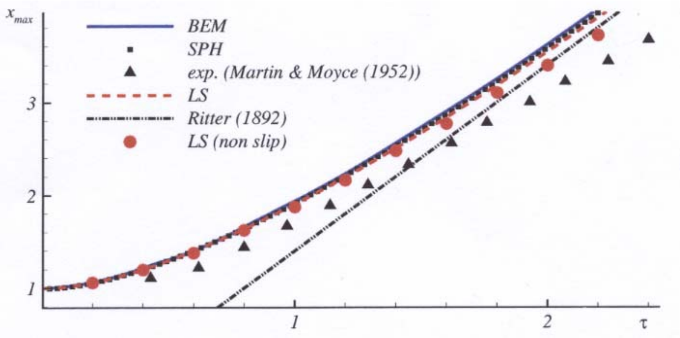

Figure 1.3 Verification and validation for the dam-breaking problem: time evolution of the water front toe. x and τ are the non-dimensional variables defined as x=X/H and $\tau = t\sqrt{g/H}$ *where X and t are respectively the physical spatial and temporal variables and H=5.7cm is the original dam height equal to the original length, L, of the reservoir behind the dam. τ=0 is the time instant for dam break and* x_{max} *is the instantaneous position of the water front. The analytical solution in Ritter (1892) gives the asymptotic velocity of the water front by a shallow-water theory. (Landrini, 2003).*

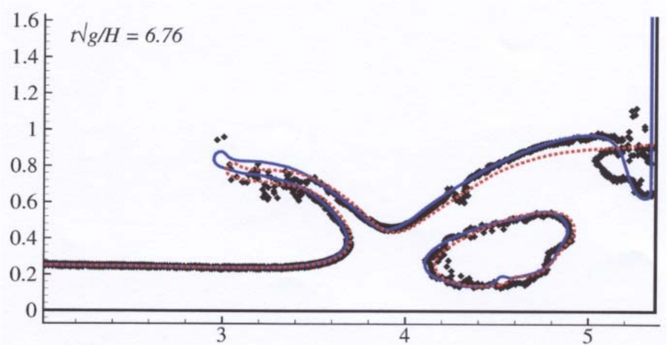

Figure 1.4 Air-water interface during the impact of a backwards plunging wave with the underlying water after the dam breaking flow has impacted against a vertical wall. Solid line: Level-Set solution. Double dots: SPH solution. Dashed line: Level-Set with reinitialization by Russo & Smereka (2000). The horizontal and vertical scales x and y are non-dimensional variables x=X/H and y=Y/H, respectively. $\tau = t\sqrt{g/H}$ *is the non-dimensional time. X and Y are the physical spatial variable. t is the physical temporal variable. The dam with the height H=60cm and the length L=2H is placed at a distance Lc=3.366H from the vertical wall. (Landrini, 2003).*

1.2.5 Constrained Interpolation Profile (CIP) method

The problem of structure-fluid interaction is not an easy task even without phase change. In most cases, the grid cannot always be adapted to the solid surface. Therefore, the description of moving solid surface of complicated shapes in the Cartesian grid system is a challenging subject. In order to attack the problem mentioned above, a method able to treat a sharp interface and to solve the interaction of compressible gas with incompressible liquid or solid is needed. Constrained Interpolation Profile method based on Cubic Interpolated Propagation (CIP) method in Takewaki et al. (1985), Takewaki & Yabe (1987), Yabe & Takei (1988), Yabe & Aoki 1991) and Yabe et al. (1991) was developed to treat both compressible and incompressible fluids with large density ratios simultaneously in one program to simulate the interaction of gas with a liquid and/or solid. The CIP method is associated with solving advection equations in the advection phase, which is the first of the three stages in the time stepping procedure. The details about this method will be described in Chapter 2.

The CIP-based finite difference method is a relatively new CFD method used in marine hydrodynamics. The structure-fluid interaction problem is treated as a multiphase problem including liquid (water), gas (air) and solid (rectangular cylinder, circular cylinder, bow flare section, V-shaped section, etc.) phases. The flow is represented by one set of governing equations including the continuity of fluid mass and the Navier-Stokes equations, which are solved numerically on a non-uniform, staggered Cartesian grid by a finite difference method. The free surface as well as the body boundary is immersed in the computational domain. An Earth-fixed rectangular grid is used to cover the air, water and solid body. An artificial mathematical problem is solved inside the body. This facilitates the numerical procedure.

In order to identify which part is the air, the water or the solid body, density functions φ_{m} (m=1, 2, 3) are introduced and satisfy the same transport equation as Eq. (1.1). The numerical method causes no sharp interface between air and water, i.e., the values of φ_1 and φ_2 change continuously between the values for air and water at the free surface. The same happens with the density functions between the body and the air and the water. However, some strategies can be applied to sharpen the interfaces.

Hu & Kashiwagi (2004) applied the CIP-based method for numerical simulation of violent free surface flows. Hu et al. (2005), Zhu et al. (2005) and Faltinsen et al. (2005) also used this method both for 2D and 3D flow and with a numerical wave tank. Hu et al. (2004) applied a conservative form of the CIP scheme, i.e. the CIP-CSL3 (Constrained Interpolation Profile-Conservative Semi-Lagrangian scheme with third-order polynomial function) scheme, which provides a way to reduce the numerical diffusion at the phase interface, to investigate violent sloshing phenomena within a horizontally oscillating rectangular tank, see Figure 1.5.

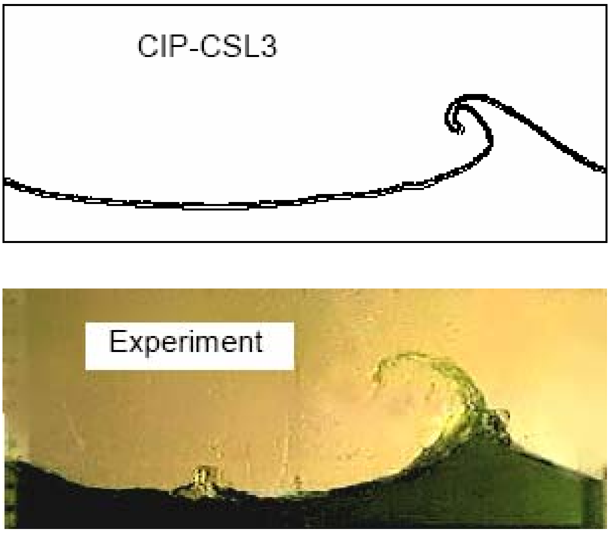

Figure 1.5 Comparison of computed free surface profiles of violent sloshing within a horizontally oscillating rectangular tank at t/T=5.8 using the CIP-CSL3 scheme. T=0.8s. The three lines denote φ_1 = 0.01, 0.50 and 0.99, respectively (Hu et al., 2004). φ_1 is explained in Eq.(2.16) in Section 2.3.1.

1.2.6 Domain Decomposition (DD)

When the BEM does not break down as illustrated above, it is generally more accurate and less time consuming than other CFD methods. A Domain Decomposition (DD) method where, for instance, the LS method is used to describe the violent fluid motion near the ship and the BEM is applied in the rest of the fluid domain is therefore an attractive approach (Colicchio et al., 2005). This assumes implicitly zero vorticity in the BEM-domain and is a reasonable assumption for most practical problems. However, it is not straightforward to combine the BEM with another CFD solver. The reason is that the BEM defines a sharp interface between the air and the water while there is implicitly assumed a continuous change of the mass density from air to water in the LS and CIP methods. A combination of the BEM and SPH methods is challenging due to the fact that particles either leave or enter the SPH fluid domain.

1.3 Present work

In this thesis, a new numerical code applying the CIP-based method is developed to solve the nonlinear wave-body interaction problems. Because this is a rather new method in the field of marine hydrodynamics, we point out the need for verification and validation by experiments.

Because we are limited from a practical CPU and storage point of view to improve the accuracy in 3D simulations by decreasing the grid size and increasing the computational domain, we present verified and validated 2D simulations of linear, weakly nonlinear and strongly nonlinear wave-body interaction problems.

1.4 Outline of the thesis

Chapter 1 is the introduction of this thesis which gives the background and motivation, possible CFD methods, present work and the content of the thesis.

Chapter 2 describes in detail the numerical method (CIP) applied in this thesis, including the numerical algorithm, the determination of the boundaries and the absorbing boundary condition, and the calculation of the hydrodynamic forces acting on the body.

In Chapter 3, 2D linear and weakly nonlinear wave-body interaction problems have been studied by using CIP-based method. For the linear problem, the hydrodynamic coefficients in harmonic heave motion for a rectangular cross-section, including the added mass and damping coefficient are calculated. The convergence of the method is studied by varying the amplitude of the forced harmonic motion, the grid size, the timestep size, the computational domain and the wave beach condition. The numerical results by CIP-based method are compared with the numerical results by BEM, the experimental results and the numerical linear results by Vugts 1968) based on an irrotational flow of incompressible water. Error sources have been discussed. The wave forces on 2D sections in the free surface zone are calculated in the numerical wave tank (NWT) which consists of a fixed body, a double-flap wavemaker to generate waves and an artificial damping zone at the downstream boundary to damp out the waves. The numerical results of 2D flow are compared with experiments by Aarsnes (1997). Experimental error sources are analyzed. The use of numerical wave tank leads to difficulties in handling the large amplitude motions. Therefore we will isolate the wave-body interaction problem to water entry and exit sub-problems.

Chapter 4 presents the numerical results of water entry and exit of a horizontal circular cylinder with constant velocity. The slamming coefficient and exit coefficient are calculated for different test conditions and are compared with the experimental results by Miao (1989). The parameters which may influence the slamming coefficient are investigated. Possible experimental error sources are analyzed. A simplified model is introduced to explain and compare with the numerical results of water exit. Two cases with higher Froude number for both water entry and water exit are simulated to further investigate the Froude number dependence of slamming coefficient and exit coefficient, however no experimental results are available for comparison.

Chapter 5 shows the numerical results of water entry and exit of a horizontal circular cylinder with free motion. A half-buoyant cylinder and a neutrally buoyant cylinder are used in the simulations of water entry and a neutrally buoyant cylinder is used in the simulations of water exit. Fully nonlinear free surface deformations of initially calm water caused by the motion of the circular cylinder are compared with the photographs taken in the experiments by Greenhow & Lin (1983). The numerically predicted motion of the circular cylinder is compared with the experimental data as well.

Chapter 6 gives the water entry forces on both vertical and heeled ship sections, including a V-shaped section and a bow flare section. All the numerical results including vertical acceleration, vertical velocity and hydrodynamic force are compared with the experiments by Aarsnes (1996). The critical angles at which ventilation occurs off the vertex of a wedge were presented as a function of deadrise angle, heel angle and the ratio U/W between the horizontal and vertical water entry velocity components by Judge et al. (2004). We tested one of the cases with deadrise angle 37°, heel angle 30° and U/W=0.75 and found the consistency of the critical angle with the results in Judge et al. (2004).

We will also present an example on 3D wave-ship interaction with severe water on the deck of a Wigley model in Chapter 7. Many interesting phenomena have been found. However, the results need to be experimentally validated.

Finally, summary and future perspectives are given in Chapter 8.

Part of the work in this thesis has been published in Zhu et al. (2005a), Zhu et al. (2005b) and Faltinsen, Zhu & Hu (2005).

CHAPTER 2

Constrained Interpolation Profile (CIP) Method

2.1 Introduction

Conventional numerical analysis methods, such as BEM for potential flow and computational fluid dynamics (CFD) methods using curvilinear grids to fit both a free surface and a body surface are not applicable to extremely nonlinear problems. Recently, several new CFD methods based on solving the Navier-Stokes equations are developed in which the free surface is captured as a part of the solution. They are therefore capable of computing more complicated free surfaces than the conventional surface-fitted methods. However, it is still a challenge for CFD to treat the complex free surface phenomena.

Using an upwind difference technique for the advection term of Navier-Stokes equations is necessary for a stable numerical calculation in computational fluid dynamics (CFD). However, the use of upwind schemes will introduce excessive numerical diffusion and associated inaccuracies. Efforts to reduce such numerical diffusion have resulted in many high-order upwind schemes.

For compressible fluid, either TVD (total variation diminishing) or ENO (essentially non-oscillating) methods proved to be effective in capturing shock waves. However, divergence of velocity which becomes zero in the incompressible fluid limit cannot be treated independently of the advection part, since these schemes employ a conservation form of the fluid equations.

Furthermore, the conservation algorithm sometimes gives fictitious pressure undulations at the boundary of multiphase materials as pointed out by Karni (1994).

Incompressible schemes like the QUICK algorithm of Leonard (1979), SIMPLE algorithm of Patankar & Spalding (1972) or higher-order upwind schemes can treat divergence-free fluid vorticity and turbulence. However, these schemes cannot always treat a shock wave as a sharp discontinuity.

We need a scheme to treat both compressible and incompressible fluids with large density ratios simultaneously in one program to simulate the interaction between gas, liquid and solid. Fully implicit solvers can handle this procedure, but the convergence of the iterations in a highly distorted state is still a problem. In an effort to move towards this goal, an Eulerian approach based on the CIP (cubic-interpolated propagation) method was developed.

The CIP method was for the first time presented as a high-order upwind scheme about 20 years ago. It does not need an adaptive grid system and therefore eliminates the grid distortion problems caused by structural breakup and topology change. The material interface can be captured by one grid throughout the computations. Further, this method can treat all the phases without restriction on the time step for high sound speed. The CIP method, which is a pressure-based algorithm coupled with a semi-Lagrangian approach, was demonstrated by Yabe et al. (2001) to be stable and robust in analyzing these subjects, but lacks conservative properties.

2.2 CIP method

2.2.1 One-dimensional CIP formulation

In order to explain the CIP method, we start from the 1D advection equation as follow

$$\frac{\partial f}{\partial t}+u\frac{\partial f}{\partial x}=0 \tag{2.1}$$

This equation presents a translational motion of a wave with velocity u. Different finite difference schemes can be used to get the numerical solution of this equation, see Yabe et al. (2001) and Figure 2.1.

The first-order upwind scheme constructed by two adjacent grid points results in numerical diffusion, because the linear interpolation will lose the information of the profile inside the grid cell. A high-order upwind scheme by more than two grid points can be used to reconstruct the profile inside the grid cell, but has an overshooting problem. Figure 2.1(d) presents a scheme different from the conventional high-order scheme called the CIP scheme, which uses the grid point value and its spatial derivative (gradient) in two grid points to form a cubic polynomial to approximate the profile.

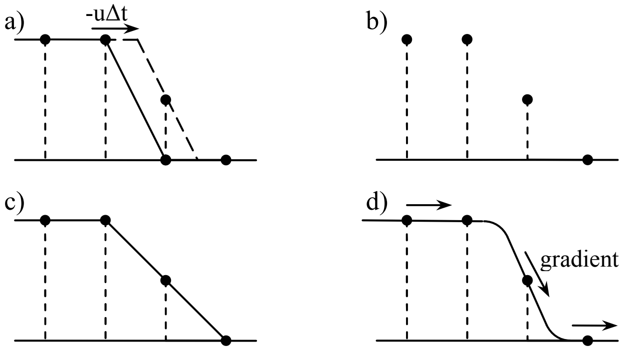

Figure 2.1 The principal of the CIP method. (a) The solid line is the initial profile and the dashed line is an exact solution after advection shown in (b) at discretized points. (c) When (b) is linearly interpolated, numerical diffusion appears. (d) In the CIP method, the spatial derivative also propagates and the profile inside a grid cell is retrieved (Yabe et al., 2001).

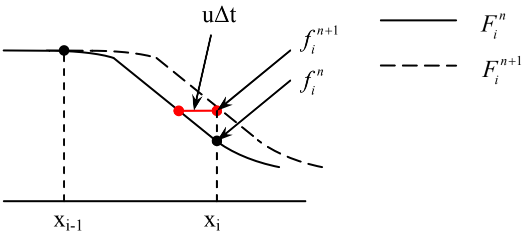

Figure 2.2 CIP scheme as a semi-Lagrangian method (Yabe et al., 2001).

By differentiating Eq. (2.1) with respect to x, we have the equation of the spatial derivative

$$\frac{\partial g}{\partial t}+u\frac{\partial g}{\partial x}=-g\frac{\partial u}{\partial x} \tag{2.2}$$

where $g=\partial f/\partial x$. For simplicity, we assume a constant advection velocity u. Then, Eq. (2.2) has the same form as Eq. (2.1). For u>0, the profile for f^n inside the upwind cell $[x_{i-1}, x_i]$ can be approximated by

$$F_i^n(x)=a_i(x-x_i)^3+b_i(x-x_i)^2+c_i(x-x_i)+d_i \tag{2.3}$$

Then the profile at timestep n+1 in Figure 2.2 is obtained by shifting the profile at timestep n by –uΔt, i.e. the time evolution of the function f and g can be obtained by using the following Lagrangian invariants:

$$f_i^{n+1} = F_i^n(x_i - u\Delta t) \qquad g_i^{n+1} = dF_i^n(x_i - u\Delta t)\big/dx \tag{2.4}$$

Therefore the CIP advection scheme is called a semi-Lagrangian method in the sense that the CIP advection scheme employs a Lagrangian invariant solution. The four known coefficients in Eq. (2.3) can be determined by known quantities f_i^n, f_{i-1}^n, g_i^n and g_{i-1}^n. We obtain the following relations

$$\begin{aligned}
a_i &= \frac{g_i^n - g_{i-1}^n}{\Delta x^2} - \frac{2\left(f_i^n - f_{i-1}^n\right)}{\Delta x^3} \\
b_i &= \frac{2g_i^n + g_{i-1}^n}{\Delta x} - \frac{3\left(f_i^n - f_{i-1}^n\right)}{\Delta x^2} \\
c_i &= g_i^n \\
d_i &= f_i^n
\end{aligned} \tag{2.5}$$

CIP was originally interpreted as ‘Cubic Interpolation Propagation’ but is recently known as ‘Constrained Interpolation Profile’, since the development of CIP has resulted in many schemes for other order polynomials than cubic, i.e. linear, quadratic Lagrange, cubic Lagrange, cubic spline and quintic Lagrange. All these schemes, except those using a linear interpolation function, need at least three points to construct an interpolation approximation in one dimension.

Compared with the conventional upwind schemes, CIP has the following features:

- Compact high-order scheme. A function and its spatial derivatives are taken as dependent variables to construct a profile. Therefore a cubic polynomial can be determined by using the information at grid points of a grid cell.

- Sub-cell resolution. The use of spatial derivatives makes the profile inside a grid cell well-reconstructed. This means that in order to achieve a certain computational accuracy, a smaller number of grid points may be used by CIP than by conventional high-order upwind schemes.

- The calculation cost does not increase even though additional variables (spatial derivatives) are introduced according to Eq. (2.4).

2.2.2 Two-dimensional CIP formulation

The general form of two-dimensional advection equations for a function χ can be written as follows:

$$\frac{\partial\chi}{\partial t}+u\frac{\partial\chi}{\partial x}+v\frac{\partial\chi}{\partial y}=0 \tag{2.6}$$

$$\frac{\partial\chi_x}{\partial t}+u\frac{\partial\chi_x}{\partial x}+v\frac{\partial\chi_x}{\partial y}=0 \tag{2.7}$$

$$\frac{\partial\chi_y}{\partial t}+u\frac{\partial\chi_y}{\partial x}+v\frac{\partial\chi_y}{\partial y}=0 \tag{2.8}$$

The subscripts x and y indicate partial derivatives with respect to x and y. The terms on the right-hand-sides (RHS) of Eqs. (2.7) and (2.8) are included in the non-advection phase calculation of a fractional step approach as shown in the next section.

Consider a grid point (i,j), then we can find a upwind cell with four grid points (i,j), (iw,j), (i,jw) and (iw,jw). Here iw=i-sign(u), jw=j-sign(v). Each grid has three continuity conditions, i.e. the values of χ^n , χ_x^n and χ_y^n , so there are 12 continuity conditions. Then a multi-dimensional polynomial up to third-order of ξ and η can be constructed to approximate the spatial distribution of the value of χ in the upwind cell as follows:

$$\begin{aligned}X(\xi,\eta)=&C_{31}\xi^3\eta+C_{13}\xi\eta^3+C_{30}\xi^3+C_{21}\xi^2\eta+C_{12}\xi\eta^2+C_{03}\eta^3+C_{20}\xi^2\\&+C_{11}\xi\eta+C_{02}\eta^2+C_{10}\xi+C_{01}\eta+C_{00}\end{aligned} \tag{2.9}$$

There are 12 unknown coefficients which can be determined by 12 continuity conditions at the four points of the upwind cell.

Another polynomial is introduced in a simpler way as

$$\begin{aligned}X(\xi,\eta)=&C_{30}\xi^3+C_{21}\xi^2\eta+C_{12}\xi\eta^2+C_{03}\eta^3+C_{20}\xi^2\\&+C_{11}\xi\eta+C_{02}\eta^2+C_{10}\xi+C_{01}\eta+C_{00}\end{aligned} \tag{2.10}$$

There are 10 unknown coefficients in Eq. (2.10) which can be determined by 10 out of 12 continuity conditions on the four grid points of the upwind cell. The values of χ^n, χ_x^n and χ_y^n at grid points (i,j), (iw,j), (i,jw) and the value of χ^n at the grid point (iw,jw) are one of the choices to determine the unknowns, but not the only one. One should note that since the continuity conditions of χ_x^n and χ_y^n at the grid point (iw,jw), i.e. the farthest grid point from the concerning point (i,j) are not used, the profile near (iw,jw) may not be correct when calculated from Eq. (2.10). However, numerical tests studied by Hu (2005) showed that the differences between the results by Eqs.(2.9) and (2.10) are negligible. For the sake of simplicity, we choose Eq. (2.10) in our calculations with the following coefficients

$$C_{30}=\left\{\xi_1\left[\chi_x^n(iw,j)+\chi_x^n(i,j)\right]-2\left[\chi^n(iw,j)-\chi^n(i,j)\right]\right\}/\xi_1^3$$

$$C_{03}=\left\{\eta_1\left[\chi_y^n(i,jw)+\chi_y^n(i,j)\right]-2\left[\chi^n(i,jw)-\chi^n(i,j)\right]\right\}/\eta_1^3$$

$$C_{20}=\left\{-\xi_1\left[\chi_x^n(iw,j)+2\chi_x^n(i,j)\right]+3\left[\chi^n(iw,j)-\chi^n(i,j)\right]\right\}/\xi_1^2$$

$$C_{02}=\left\{-\eta_1\left[\chi_y^n(i,jw)+2\chi_y^n(i,j)\right]+3\left[\chi^n(i,jw)-\chi^n(i,j)\right]\right\}/\eta_1^2$$

$$C_{21}=\left\{\left[\chi^n(iw,jw)-\chi^n(iw,j)-\chi^n(i,jw)+\chi^n(i,j)\right]-\xi_1\left[\chi_x^n(i,jw)-\chi_x^n(i,j)\right]\right\}/(\xi_1^2\eta_1)$$

$$C_{12}=\left\{\left[\chi^n(iw,jw)-\chi^n(iw,j)-\chi^n(i,jw)+\chi^n(i,j)\right]-\eta_1\left[\chi_y^n(i,jw)-\chi_y^n(i,j)\right]\right\}/(\xi_1\eta_1^2)$$

$$C_{11}=-\left[\chi^n(iw,jw)-\chi^n(iw,j)-\chi^n(i,jw)+\chi^n(i,j)\right]\Big/(\xi_1\eta_1)$$

$$+\left\{\xi_1\left[\chi_x^n(i,jw)-\chi_x^n(i,j)\right]+\eta_1\left[\chi_y^n(iw,j)-\chi_y^n(i,j)\right]\right\}\Big/(\xi_1\eta_1)$$

$$=\left[\chi^n(iw,jw)-\chi^n(iw,j)-\chi^n(i,jw)+\chi^n(i,j)\right]\Big/(\xi_1\eta_1)-C_{21}\xi_1-C_{12}\eta_1$$

$$C_{10}=\chi_x^n(i,j)$$

$$C_{01}=\chi_y^n(i,j)$$

$$C_{00}=\chi^n(i,j)$$

where $\xi_1=-\text{sign}(u)\Delta x$ and $\eta_1=-\text{sign}(v)\Delta y$. Once the interpolation function has been determined, the values after the advection calculation, χ^*, χ_x^* and χ_y^*, can be directly obtained as follows:

$$\chi^*(i,j)=X(\xi',\eta')$$

$$\chi_x^*(i,j)=\left.\frac{\partial X(\xi,\eta)}{\partial\xi}\right|_{\substack{\xi=\xi'\\ \eta=\eta'}}$$

$$\chi_y^*(i,j)=\left.\frac{\partial X(\xi,\eta)}{\partial\eta}\right|_{\substack{\xi=\xi'\\ \eta=\eta'}}$$

where $\xi' = -u\Delta t$ and $\eta' = -v\Delta t$. This is called A-type CIP scheme where the advection part can be calculated by a semi-Lagrangian procedure after the interpolation function of Eq. (2.10) is determined.

A-type CIP

$$\chi^{n+1}(\mathbf{x}) = \mathrm{X}^n\left(\mathbf{x} - \mathbf{u}^n \Delta t\right)$$

$$\left(\partial_\xi \chi\right)^{n+1}(\mathbf{x}) = \frac{\partial \mathrm{X}^n}{\partial \xi}\left(\mathbf{x} - \mathbf{u}^n \Delta t\right)$$

For multi-dimensional advection calculations, there are several other CIP schemes called C-type and M-type schemes which make use of a dimensional splitting method and do multi-dimensional CIP calculation by repeating one-dimensional CIP calculation. The concept of these schemes is shown in Figure 2.3 for two-dimensional cases.

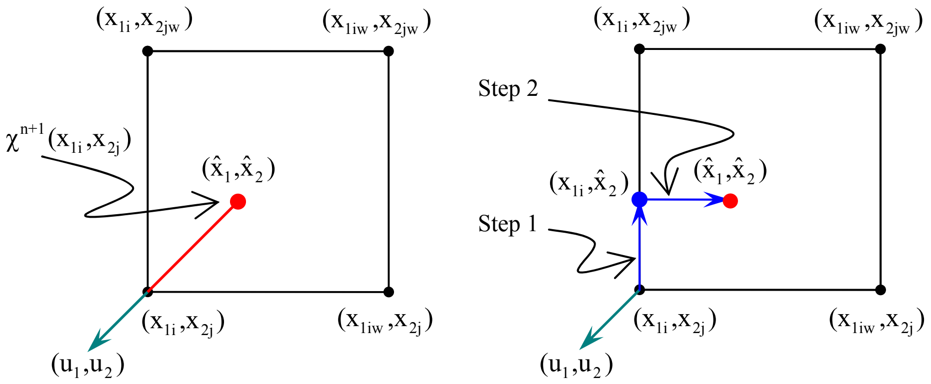

(a) A-type CIP (b) C-type or M-type CIP

Figure 2.3 Concept for A-type, C-type and M-type schemes in two dimensions.

C-type CIP

Step 1

$$A_i = \chi^n(x_{1i},\hat{x}_2) = \mathrm{CIP\_1D}(\chi^n_{i,j},(\partial_{x_2}\chi)^n_{i,j},\chi^n_{i,jw},(\partial_{x_2}\chi)^n_{i,jw},x_2=\hat{x}_2)$$

$$\partial_{x_2} A_i = \frac{\partial}{\partial x_2}\chi^n(x_{1i},\hat{x}_2) = \frac{\partial}{\partial x_2}\mathrm{CIP\_1D}(\chi^n_{i,j},(\partial_{x_2}\chi)^n_{i,j},\chi^n_{i,jw},(\partial_{x_2}\chi)^n_{i,jw},x_2=\hat{x}_2)$$

$$\partial_{x_1} A_i = \partial_{x_1} \chi^n (x_{1i}, \hat{x}_2) = \mathrm{CIP\_1D}\Big((\partial_{x_1}\chi)^n_{i,j}, (\partial_{x_1x_2}\chi)^n_{i,j}, (\partial_{x_1}\chi)^n_{i,jw}, (\partial_{x_1x_2}\chi)^n_{i,jw}, x_2 = \hat{x}_2) \Big)$$

$$\partial_{x_1x_2} A_i = \frac{\partial}{\partial x_2} \partial_{x_1} \chi^n (x_{1i}, \hat{x}_2) = \frac{\partial}{\partial x_2} \mathrm{CIP\_1D}\Big((\partial_{x_1}\chi)^n_{i,j}, (\partial_{x_1x_2}\chi)^n_{i,j}, (\partial_{x_1}\chi)^n_{i,jw}, (\partial_{x_1x_2}\chi)^n_{i,jw}, x_2 = \hat{x}_2) \Big)$$

Step 2

$$\chi^{n+1}_{i,j} = \mathrm{CIP\_1D}(A_i, \partial_{x_1} A_i, A_{iw}, \partial_{x_1} A_{iw}, x_1 = \hat{x}_1)$$

$$\partial_{x_1} \chi^{n+1}_{i,j} = \frac{\partial}{\partial x_1} \mathrm{CIP\_1D}(A_i, \partial_{x_1} A_i, A_{iw}, \partial_{x_1} A_{iw}, x_1 = \hat{x}_1)$$

$$\partial_{x_2} \chi^{n+1}_{i,j} = \mathrm{CIP\_1D}(\partial_{x_2} A_i, \partial_{x_1x_2} A_i, \partial_{x_2} A_{iw}, \partial_{x_1x_2} A_{iw}, x_1 = \hat{x}_1)$$

$$\partial_{x_1x_2} \chi^{n+1}_{i,j} = \frac{\partial}{\partial x_1} \mathrm{CIP\_1D}(\partial_{x_2} A_i, \partial_{x_1x_2} A_i, \partial_{x_2} A_{iw}, \partial_{x_1x_2} A_{iw}, x_1 = \hat{x}_1)$$

where CIP_1D denotes one-dimensional CIP calculation. The C-type CIP has the same accuracy as the A-type CIP. The merit of C-type CIP is easy extension to multi-dimensions. The disadvantage is that extra dependent variables should be introduced, such as $\partial_{x_1x_2}\chi$ for 2D case. To avoid using higher-order spatial derivatives, an M-type CIP scheme was developed.

M-type CIP

Step 1

$$A_i = \chi^n (x_{1i}, \hat{x}_2) = \mathrm{CIP\_1D}(\chi^n_{i,j}, (\partial_{x_2}\chi)^n_{i,j}, \chi^n_{i,jw}, (\partial_{x_2}\chi)^n_{i,jw}, x_2 = \hat{x}_2)$$

$$\partial_{x_2} A_i = \frac{\partial}{\partial x_2} \chi^n (x_{1i}, \hat{x}_2) = \frac{\partial}{\partial x_2} \mathrm{CIP\_1D}(\chi^n_{i,j}, (\partial_{x_2}\chi)^n_{i,j}, \chi^n_{i,jw}, (\partial_{x_2}\chi)^n_{i,jw}, x_2 = \hat{x}_2)$$

$$\partial_{x_1} A_i = \mathrm{FDM\_1D}\Big((\partial_{x_1}\chi)^n_{i,j}, (\partial_{x_1}\chi)^n_{i,jw}, x_2 = \hat{x}_2 \Big)$$

Step 2

$$\chi^{n+1}_{i,j} = \mathrm{CIP\_1D}(A_i, \partial_{x_1} A_i, A_{iw}, \partial_{x_1} A_{iw}, x_1 = \hat{x}_1)$$

$$\partial_{x_1} \chi^{n+1}_{i,j} = \frac{\partial}{\partial x_1} \mathrm{CIP\_1D}(A_i, \partial_{x_1} A_i, A_{iw}, \partial_{x_1} A_{iw}, x_1 = \hat{x}_1)$$

$$\partial_{x_2} \chi^{n+1}_{i,j} = \mathrm{FDM\_1D}(\partial_{x_2} A_i, \partial_{x_2} A_{iw}, x_1 = \hat{x}_1)$$

Here a linear interpolation denoted as FDM_1D is used. The precision of M-type CIP scheme may be less than A-type and C-type schemes. However, numerical experiments by Hu (2005) have shown that the difference in the computational results by the three schemes is not significant. For the sake of simplicity, M-type scheme is often used in multi-dimensional computations.

2.3 Numerical algorithm

2.3.1 Governing equations

Two-dimensional water and air flow in interaction with a solid body is considered in this thesis. The fluid is assumed compressible and viscous. Temperature variations are neglected. The governing equations for the fluid are

$$\frac{\partial \rho}{\partial t} + u_i \frac{\partial \rho}{\partial x_i} = -\rho \frac{\partial u_i}{\partial x_i} \tag{2.11}$$

$$\frac{\partial u_i}{\partial t} + u_j \frac{\partial u_i}{\partial x_j} = -\frac{1}{\rho} \frac{\partial \sigma_{ij}}{\partial x_j} + f_i \tag{2.12}$$

$$p = f(\rho) \tag{2.13}$$

where

t is the time variable;
x_i ($i = 1,2$) are the coordinates of a Cartesian coordinate system;
ρ is the mass density;
u_i ($i=1,2$) are the velocity components;
f_i ($i=1,2$) are due to the gravity force.

Further, σ_{ij} is the total stress and is expressed as

$$\sigma_{ij} = -p\delta_{ij} + 2\mu(1-\delta_{ij}/3)S_{ij}$$

where:

p is the pressure;
μ is the dynamic viscosity coefficient;
δ_{ij} is the Kronecker delta function;

$$S_{ij} = \frac{1}{2}\left(\frac{\partial u_i}{\partial x_j} + \frac{\partial u_j}{\partial x_i}\right)$$

The expression for σ_{ij} implies a modeling of the bulk viscosity for compressible fluid that can be questioned; see White (1974). If turbulent flow is considered, the equations have to be averaged over the time scale of turbulence and additional equations describing the Reynolds stresses must be introduced. We assume laminar flow in the following studies. This is appropriate for the boundary layer flow in the considered Reynolds number range. Even though the boundary layer flow is laminar and flow separation occurs, the separated flow will be turbulent for the considered Reynolds numbers. However, it is more important to correctly predict the boundary layer flow and where flow separation occurs than the fact that the separated flow is turbulent.

The sound speed C defined as $C=\sqrt{dp/d\rho}$ gives

$$\frac{dp}{dt}=C^2\frac{d\rho}{dt}$$

or

$$\frac{\partial p}{\partial t}+u_i\frac{\partial p}{\partial x_i}=C^2\left(\frac{\partial \rho}{\partial t}+u_i\frac{\partial \rho}{\partial x_i}\right) \tag{2.14}$$

Making use of Eq. (2.11), the equation of state (EOS) given by Eq. (2.13) can be expressed by Eq. (2.14) as follow

$$\frac{\partial p}{\partial t}+u_i\frac{\partial p}{\partial x_i}=-\rho C^2\frac{\partial u_i}{\partial x_i} \tag{2.15}$$

In order to identify which part is the air, the water or the solid body, density functions φ_m (m=1, 2, 3) are introduced. These functions satisfy

$$\frac{\partial \varphi_m}{\partial t}+u_i\frac{\partial \varphi_m}{\partial x_i}=0 \tag{2.16}$$

with

$$\varphi_m(x,y,t)=\begin{cases}1, & (x,y)\in\Omega_m\\ 0, & \text{otherwise}\end{cases}$$

where Ω_m denotes the domain occupied by the liquid, gas and solid phase, respectively. The left-hand-side (LHS) of Eq. (2.16) is the material derivative of $\frac{D\varphi}{Dt}$. Eq. (2.16) indicates that if we follow a fluid particle, the property φ_m of the fluid particle does not change with time. The numerical method causes no sharp interface between air and water, i.e., the values of φ_1 and φ_2 change continuously between the values for air and water at the free surface. The same happens with the density functions between the body , the air and the water.

Because a one-fluid formulation is used, that is the air and the water phases are modeled as a single fluid with varying properties (i.e. density, viscosity, etc.), there is no need to specify dynamic conditions in terms of stresses at the interface between the air and the water. The dynamic conditions are automatically satisfied.

The time integration of the governing equations of the fluid, i.e. Eqs. (2.11), (2.12) and (2.15), together with the density function Eq. (2.16), is based on an Euler method and a fractional step approach consisting of three steps.

2.3.2 The fractional step approach

The governing equations of the fluid and the density function are written as follows

$$\frac{\partial}{\partial t}\begin{pmatrix}\rho\\ u_j\\ p\\ \varphi_m\end{pmatrix}+u_i\frac{\partial}{\partial x_i}\begin{pmatrix}\rho\\ u_j\\ p\\ \varphi_m\end{pmatrix}=\begin{pmatrix}0\\ 0\\ 0\\ 0\end{pmatrix}+\begin{pmatrix}0\\ \frac{2\mu}{\rho}\frac{\partial}{\partial x_j}\left(S_{ij}-\frac{1}{3}\delta_{ij}S_{kk}\right)+f_j\\ 0\\ 0\end{pmatrix}+\begin{pmatrix}-\rho\frac{\partial u_i}{\partial x_i}\\ -\frac{1}{\rho}\frac{\partial p}{\partial x_i}\\ -\rho C^2\frac{\partial u_i}{\partial x_i}\\ 0\end{pmatrix}\quad(2.17)$$

By applying a fractional step approach, the numerical solution of the governing equations can be divided into two phases: advection phase and non-advection phase. The non-advection phase is divided into a state-related part to reflect the fluid compressibility denoted by non-advection phase (ii) and a remaining part denoted by non-advection phase (i). Therefore, there are totally three fractional steps, and the three fractional steps are arranged in an order of the advection phase, the non-advection phase (i) and the non-advection phase (ii).

The time integration of the equations is based on an Euler method. The variables with superscript ‘n’ denote the values at the present time level. The following procedure shows how to get the values at the new timestep ‘n+1’ by calculation of the three intermediate steps.

1. **Advection phase**

$$\left(\frac{\partial}{\partial t}+u_i\frac{\partial}{\partial x_i}\right)\begin{pmatrix}\rho\\ u_j\\ p\\ \varphi_m\end{pmatrix}=\begin{pmatrix}0 & 0 & 0 & 0\end{pmatrix}^T$$

The first fractional step is called the advection phase. It means that the right-hand side (RHS) of Eq. (2.17) is set equal to zero. The equations of the first-order spatial derivatives $\partial/\partial x_i$ of ρ, u_i, p and φ_m denoted as $\partial_{x_i}\rho$, $\partial_{x_i}u_j$, $\partial_{x_i}p$ and $\partial_{x_i}\varphi_m$ are obtained by differentiating Eq. (2.17) with respect to x_i.

$$\left(\frac{\partial}{\partial t}+u_i\frac{\partial}{\partial x_i}\right)\begin{pmatrix}\partial_{x_i}\rho\\ \partial_{x_i}u_j\\ \partial_{x_i}p\\ \partial_{x_i}\varphi_m\end{pmatrix}=\begin{pmatrix}0 & 0 & 0 & 0\end{pmatrix}^T-\begin{pmatrix}\frac{\partial\rho}{\partial x_i} & \frac{\partial u_j}{\partial x_i} & \frac{\partial p}{\partial x_i} & \frac{\partial\varphi_m}{\partial x_i}\end{pmatrix}^T\frac{\partial u_i}{\partial x_i} \quad (2.18)$$

The RHS of Eq. (2.18) is also set equal to zero in the advection phase computation. Because all the equations in the advection phase have the same mathematical form $\frac{\partial\chi}{\partial t}+u_i\frac{\partial\chi}{\partial x_i}=0$, the advection phase computation can be done by the CIP method.

$$\frac{\rho^*-\rho^n}{\Delta t}+u_i^n\frac{\partial\rho^n}{\partial x_i}=0$$

$$\frac{u_i^*-u_i^n}{\Delta t}+u_j^n\frac{\partial u_i^n}{\partial x_j}=0$$

$$\frac{p^*-p^n}{\Delta t}+u_i^n\frac{\partial p^n}{\partial x_i}=0$$

$$\frac{{\varphi_m}^*-{\varphi_m}^n}{\Delta t}+u_i^n\frac{\partial{\varphi_m}^n}{\partial x_i}=0$$

$$\frac{(\partial_{x_i}\rho)^*-(\partial_{x_i}\rho)^n}{\Delta t}+u_i^n\frac{\partial(\partial_{x_i}\rho)^n}{\partial x_i}=0$$

$$\frac{(\partial_{x_i}u_j)^*-(\partial_{x_i}u_j)^n}{\Delta t}+u_i^n\frac{\partial(\partial_{x_i}u_j)^n}{\partial x_i}=0$$

$$\frac{(\partial_{x_i}p)^*-(\partial_{x_i}p)^n}{\Delta t}+u_i^n\frac{\partial(\partial_{x_i}p)^n}{\partial x_i}=0$$

$$\frac{(\partial_{x_i}\varphi_m)^*-(\partial_{x_i}\varphi_m)^n}{\Delta t}+u_i^n\frac{(\partial_{x_i}\varphi_m)^n}{\partial x_i}=0$$

The superscript * indicates the intermediate values after the CIP computations.

The source terms at the RHS of the equations of the spatial derivatives, i.e. Eq. (2.18) are computed by a central-difference scheme, and the values of the spatial derivatives are updated by an Euler explicit scheme as follows

$$\frac{\overline{(\partial_{x_i}\rho)}-(\partial_{x_i}\rho)^*}{\Delta t}=-\frac{\partial\rho^*}{\partial x_i}\frac{\partial u_i^*}{\partial x_i}$$

$$\frac{\overline{(\partial_{x_i}u_j)}-(\partial_{x_i}u_j)^*}{\Delta t}=-\frac{\partial u_j^*}{\partial x_i}\frac{\partial u_i^*}{\partial x_i}$$

$$\frac{\overline{(\partial_{x_i} p)} - (\partial_{x_i} p)^*}{\Delta t} = -\frac{\partial p^*}{\partial x_i}\frac{\partial u_i^*}{\partial x_i}$$

$$\frac{\overline{(\partial_{x_i} \varphi_m)} - (\partial_{x_i} \varphi_m)^*}{\Delta t} = -\frac{\partial \varphi_m^*}{\partial x_i}\frac{\partial u_i^*}{\partial x_i}$$

The spatial derivatives with an overbar indicate the intermediate values after the computations of the first fractional step.

2. Non-advection phase (i)

$$\frac{\partial}{\partial t}\begin{pmatrix}\rho\\ u_j\\ p\\ \varphi_m\end{pmatrix} = \begin{pmatrix}0 & \frac{2\mu}{\rho}\frac{\partial}{\partial x_j}\left(S_{ij}-\frac{1}{3}\delta_{ij}S_{kk}\right)+f_j & 0 & 0\end{pmatrix}^T$$

For the non-advection phase (i), a central difference scheme is used for the RHS terms and an Euler explicit scheme is used for the time integration. The spatial derivatives of the velocity components are also updated simultaneously

$$\frac{u_j^{**}-u_j^*}{\Delta t} = \frac{2\mu}{\rho^*}\frac{\partial}{\partial x_j}\left(S_{ij}^*-\frac{1}{3}\delta_{ij}S_{kk}^*\right)+f_j$$

$$\frac{(\partial_{x_i} u_j)^{**}-\overline{(\partial_{x_i} u_j)}}{\Delta t} = \frac{\partial}{\partial x_i}\left(\frac{2\mu}{\rho^*}\frac{\partial}{\partial x_j}\left(S_{ij}^*-\frac{1}{3}\delta_{ij}S_{kk}^*\right)+f_j\right)$$

Here the value with the superscript ** denotes the intermediate value after the computations of the second fractional step and also the derivative at the new timestep ‘n+1’.

3. Non-advection phase (ii)

$$\frac{\partial}{\partial t}\begin{pmatrix}\rho\\ u_i\\ p\\ \varphi_m\end{pmatrix} = \begin{pmatrix}-\rho\frac{\partial u_i}{\partial x_i} & -\frac{1}{\rho}\frac{\partial p}{\partial x_i} & -\rho C^2\frac{\partial u_i}{\partial x_i} & 0\end{pmatrix}^T$$

For the non-advection phase (ii), an implicit scheme is used for the time integration.

$$\frac{\rho^{n+1}-\rho^*}{\Delta t} = -\rho^*\frac{\partial u_i^{n+1}}{\partial x_i} \tag{2.19}$$

$$\frac{u_i^{n+1}-u_i^{**}}{\Delta t}=-\frac{1}{\rho^*}\frac{\partial p^{n+1}}{\partial x_i} \tag{2.20}$$

$$\frac{p^{n+1}-p^*}{\Delta t}=-\rho^* C^2\frac{\partial u_i^{n+1}}{\partial x_i} \tag{2.21}$$

$$\frac{\varphi_m{}^{n+1}-\varphi_m{}^*}{\Delta t}=0$$

Taking divergence of Eq. (2.20) and substituting $\partial u_i^{n+1}/\partial x_i$ by using Eq. (2.21), we obtain the following pressure equation

$$\frac{\partial}{\partial x_i}\left(\frac{1}{\rho}\frac{\partial p^{n+1}}{\partial x_i}\right)=\frac{p^{n+1}-p^*}{\rho^* C^2\Delta t^2}+\frac{1}{\Delta t}\frac{\partial u_i^{**}}{\partial x_i} \tag{2.22}$$

This is a Poisson type equation for the pressure calculation. This equation is valid for liquid, gas and solid phases, and we can obtain the pressure field in the whole computation domain by solving this equation. This is the most time-consuming part.

For the solid phase (the body), this Poisson equation reduces to a Laplace equation for the pressure of an artificial problem inside the body. We implicitly solve the artificial problem inside the body. We enforce the velocity inside the body equal to the rigid body velocity. The interior pressure satisfies the Laplace equation and is consistent with the pressure on the body surface. The interior pressure and velocity is not consistent with Eqs. (2.11), (2.12), (2.15) and (2.16), i.e. it is not a true flow problem. The reason for doing this is from a practical computational point of view. The procedure ensures that the body boundary conditions are satisfied. This is obviously needed as a part of solving the exterior flow. We do not need to explicitly specify the free surface conditions. This is implicitly taken care of by the method.

The computation of advection phase has no restriction on the size or the sign of the Courant-Friedrich-Lewy (CFL) number $\beta = u\Delta t/\Delta x$. However, using the explicit time integration, i.e. Euler scheme, results in a CFL restriction for the time step size as documented in Kawasaki (2005), i.e. β is less than 1.0.

2.3.3 Cartesian grid method

In this thesis, we apply the CIP method together with a Cartesian grid method to solve the wave-body interaction problem. As a matter of fact, there are many numerical methods that can be applied for the wave-body interaction, including grid method and gridless method. If we consider the grid methods, they can be roughly divided into two categories: domain dividing method and domain embedding method as shown in Figure 2.4.

For the domain dividing method, the free surface and the body surface are taken as the moving domain boundaries to be determined. A curvilinear grid or an unstructured grid that adapted to the boundary is required. Although this method gives high resolution for boundary layer computation, the grid generation with complicated boundaries is troublesome and the regridding process for unsteady problem is computationally costly. Therefore this method is generally not applicable for strongly nonlinear marine hydrodynamic problems such as slamming, water on deck, wave impact by green water, and capsizing due to large-amplitude waves.

However, the domain embedding method can in general be applied to those complicated problems. We can foresee problems if a thin plate is studied. A practical example that is challenging to handle is a ship equipped with bilge keels. As a Cartesian grid is often used, this domain embedding method is also called Cartesian grid method. The use of a Cartesian grid method can greatly simplify the structure of the code and increase the computation efficiency for problems with complicated free surface and moving bodies.

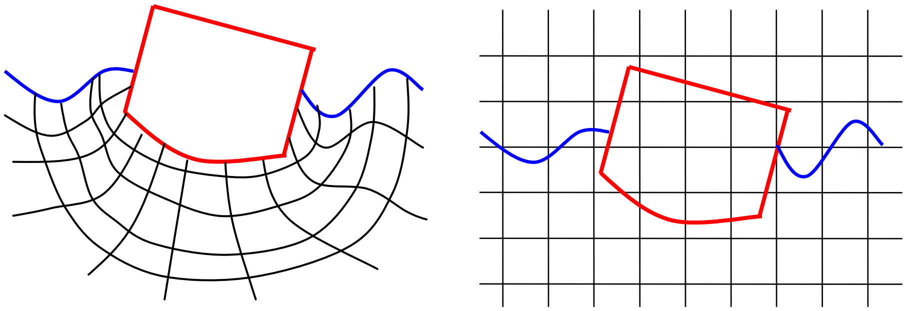

(a) Domain dividing (b) Domain embedding (Cartesian grid)

Figure 2.4 Examples of two grid systems used in the Finite Difference Method (FDM) to model wave-body interaction problems. (a) Domain dividing method uses a grid system adapted to the instantaneous body boundary and free surface. (b) Domain embedding method uses an Earth-fixed Cartesian grid system.

Figure 2.5 shows the grid system used in the calculations where we have the following relations: dx(i)=x(i)-x(i-1), dy(j)=y(j)-y(j-1), xc(i)=[x(i)+x(i-1)]/2, yc(i)=[y(j)+y(j-1)]/2, dxc(i)=xc(i)-xc(i-1) and dyc(j)=yc(j)-yc(j-1). The computational domain is divided into rectangular cells. An exterior fictitious one-cell layer adjacent to each side of the physical domain is added to allow imposition of discrete boundary conditions.

A staggered grid configuration shown in Figure 2.6 is used to discretize the dependent variables. On each cell, the pressure p is computed at the cell center, the velocity component u is computed at the middle of the vertical edge, and the velocity component v is computed at the middle of the horizontal edge. The first-order spatial derivatives are computed at the same position as the variables. In the associated formulation, the u-momentum equation is discretized at the middle of the right vertical edge, the *v*-momentum equation is discretized at the middle of the top horizontal edge, and the continuity equation is discretized at the cell center.

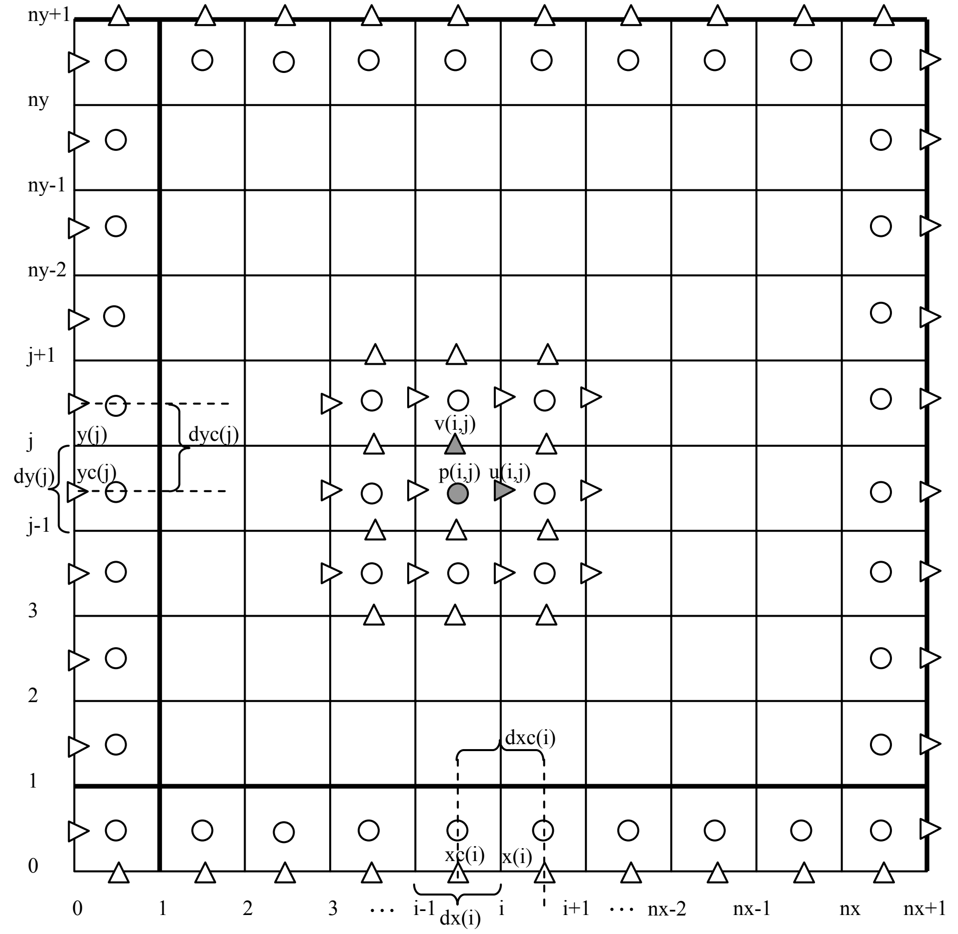

Figure 2.5 Grid system used in the 2D CIP calculations. p is the pressure. u and v are horizontal and vertical velocity components, respectively.

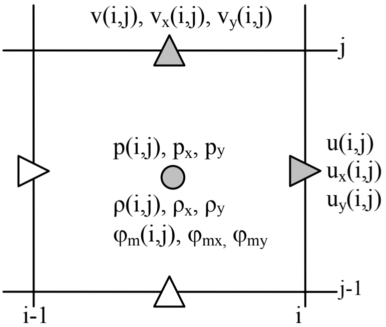

Figure 2.6 The staggered grid used in combination with the 2D CIP method. p is the pressure. u and v are horizontal and vertical velocity components, respectively. ρ is the density of air, water or solid body. φ_m (m=1,2,3) is the density function. The subscripts x and y denotes the spatial derivatives with respect to x and y.

2.3.4 Iterative methods for Poisson equation

As the fluid is assumed to be incompressible, i.e. the pressure wave propagates at infinite speed, the Poisson equation for pressure can be rewritten as

$$\frac{\partial}{\partial x_i}\left(\frac{1}{\rho}\frac{\partial p^{n+1}}{\partial x_i}\right)=\frac{1}{\Delta t}\frac{\partial u_i^{**}}{\partial x_i} \tag{2.23}$$

Since most of the CPU time will be spent solving the Poisson equation, the use of a fast solution method is important for increasing the total computation efficiency. For a 2D problem, the Poisson equation can be written in a finite difference form for a cell (i,j) as

$$\begin{aligned}&\frac{1}{\Delta x_i}\left(\frac{1}{\rho_{Ei,j}}\frac{p_{i+1,j}^{n+1}-p_{i,j}^{n+1}}{\Delta xc_i}-\frac{1}{\rho_{Wi,j}}\frac{p_{i,j}^{n+1}-p_{i-1,j}^{n+1}}{\Delta xc_{i-1}}\right)\\&+\frac{1}{\Delta y_i}\left(\frac{1}{\rho_{Ni,j}}\frac{p_{i,j+1}^{n+1}-p_{i,j}^{n+1}}{\Delta yc_j}-\frac{1}{\rho_{Si,j}}\frac{p_{i,j}^{n+1}-p_{i,j-1}^{n+1}}{\Delta yc_{j-1}}\right)\\&=\frac{1}{\Delta t}\left(\frac{u_{i,j}^{**}-u_{i-1,j}^{**}}{\Delta x_i}-\frac{v_{i,j}^{**}-v_{i,j-1}^{**}}{\Delta y_j}\right)\end{aligned} \tag{2.24}$$

where $\Delta x_i = dx(i)$, $\Delta y_i = dy(i)$, $\Delta xc_i = dxc(i)$ and $\Delta yc_i = dyc(i)$ as defined in Figure 2.5, respectively.

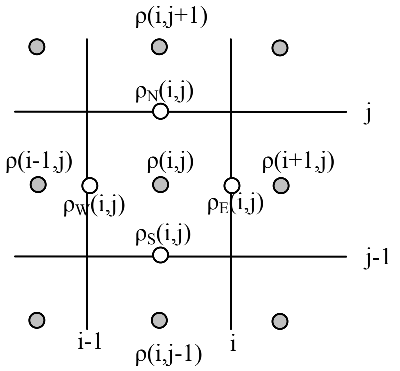

Figure 2.7 Definition of density ρ on the grid lines.

The density $\rho_N(i,j)$, $\rho_S(i,j)$, $\rho_W(i,j)$ and $\rho_E(i,j)$ are computed at the positions presented in Figure 2.7. $\rho_N(i,j)$ is linearly interpolated by the nearest two values of $\rho(i,j)$ and $\rho(i,j+1)$, $\rho_S(i,j)$ by $\rho(i,j)$ and $\rho(i,j-1)$, $\rho_W(i,j)$ by $\rho(i,j)$ and $\rho(i-1,j)$, and $\rho_E(i,j)$ by $\rho(i,j)$ and $\rho(i+1,j)$, respectively.

$$\rho_N(i,j) = \frac{\rho(i,j)\Delta y(j+1) + \rho(i,j+1)\Delta y(j)}{\Delta y(j) + \Delta y(j+1)}$$

$$\rho_N(i,j) = \frac{\rho(i,j)\Delta y(j-1) + \rho(i,j-1)\Delta y(j)}{\Delta y(j) + \Delta y(j-1)}$$

$$\rho_S(i,j) = \frac{\rho(i,j)\Delta x(i-1) + \rho(i-1,j)\Delta x(i)}{\Delta x(i) + \Delta x(i-1)}$$

$$\rho_E(i,j) = \frac{\rho(i,j)\Delta x(i+1) + \rho(i+1,j)\Delta x(i)}{\Delta x(i) + \Delta x(i+1)}$$

Equation (2.24) represents a sparse linear system for the pressure p which can be rewritten as

$$\mathbf{A}\mathbf{x} = \mathbf{b} \qquad (2.25)$$

where **A** is an M×M matrix, and **b** are vectors with M elements. Here M=NX×NY. NX and NY are grid number in x-, y-direction, respectively. For a sparse linear system, we need an iterative method for numerical solution. There are two types of iterative methods: the stationary method and the non-stationary method.

The stationary method, e.g. the successive over-relaxation (SOR) method is an old method, but easy to understand and implement. The algorithm of SOR is as follows:

$$\hat{x}_i^{(k)} = \frac{1}{a_{ii}}\left(b_i - \sum_{j<i} a_{ij} x_j^{(k)} - \sum_{j>i}^{M} a_{ij} x_j^{(k-1)} \right) \tag{2.26}$$

$$x_i^{(k)} = \omega \hat{x}_i^{(k)} + (1-\omega) x_i^{(k-1)} \tag{2.27}$$

where ω is an acceleration coefficient with $0<\omega<2$. $x_i^{(k-1)}$ denotes the value at previous iteration k-1, $\hat{x}_i^{(k)}$ is the intermediate value and $x_i^{(k)}$ is the value at present iteration k. SOR may be the most efficient stationary method. We use this method to solve the Poisson equation. However, the rate of convergence is too slow to use for the large-scale linear system in a 3D computation.

The non-stationary method is usually hard to understand but highly effective. The efficiency of the method largely depends on the so-called pre-conditioner. The Bi-Conjugate Gradient Stabilized method (Bi-CGSTAB) of Vorst (1992) is found to work well for the CIP method. The Bi-CGSTAB method with preconditioning matrix **K** is given in Xiao (2001) as:

```
Set :
        the initial residual $\mathbf{r}_0 = \mathbf{b} - \mathbf{A}\mathbf{x}_0$;  $\mathbf{x}_0$ is the initial guess;
        $\hat{\mathbf{r}}_0 = \mathbf{r}_0$;
        $\rho_0 = \omega_0 = \alpha_0 = 1$;
        $\mathbf{v}_0 = \mathbf{p}_0 = 0$;
for i=1, 2, 3, …
        $\rho_i = (\mathbf{r}_i, \bar{\mathbf{r}}_i)$;
        $\beta_{i-1} = (\rho_i / \rho_{i-1}) / (\alpha_{i-1} / \omega_{i-1})$;
        $\mathbf{p}_i = \mathbf{r}_i + \beta_{i-1}(\mathbf{p}_{i-1} - \omega_{i-1}\mathbf{v}_{i-1})$ ;
        solve $\hat{\mathbf{p}}$ from $\mathbf{K}\hat{\mathbf{p}} = \mathbf{p}_i$;
        $\mathbf{v}_i = \mathbf{A}\hat{\mathbf{p}}$;
        $\alpha_i = \rho_i / (\mathbf{v}_i, \bar{\mathbf{r}}_0)$;
        $\mathbf{s} = \mathbf{r}_i - \alpha_i \mathbf{v}_i$;
        solve q from Kq=s;
        u=Aq;
        $\omega_i = (\mathbf{u}, \mathbf{s}) / (\mathbf{u}, \mathbf{u})$;
        $\mathbf{x}_{i+1} = \mathbf{x}_i + \alpha_i \hat{\mathbf{p}} + \omega_i \mathbf{q}$;
        $\mathbf{r}_{i+1} = \mathbf{s} - \omega_i \mathbf{u}$;
        if $\|\mathbf{r}_{i+1}\| / \|\mathbf{b}\| \le \varepsilon_T$ then quit
end
```

However, numerical implementation of the Bi-CGSTAB method with a good pre-conditioning is not easy. On the other hand, it is hard to treat an irregular body boundary. The CIP code in this thesis uses a Cartesian grid method which has no difficulty with it because a rectangular computation domain is always used.

2.4 Determination of boundaries

Density functions φ_m (m=1, 2, 3) with $0 \le \varphi_m \le 1$ are introduced to identify which part is the air, the water or the solid body. There are two types of interfaces that need to be captured in the numerical simulations, i.e., the interface between air and water (the free surface) and the interface between solid body and water, such as the floating body boundary, see Figure 2.8. The behaviors of these two types of interface are quite different, and so different capturing methods are used for each of them. Since a constraint within a computational cell is $\sum_{m=1}^{3} \varphi_m = 1$, after φ_1 and φ_3 are known, we have $\varphi_2 = 1 - \varphi_1 - \varphi_3$.

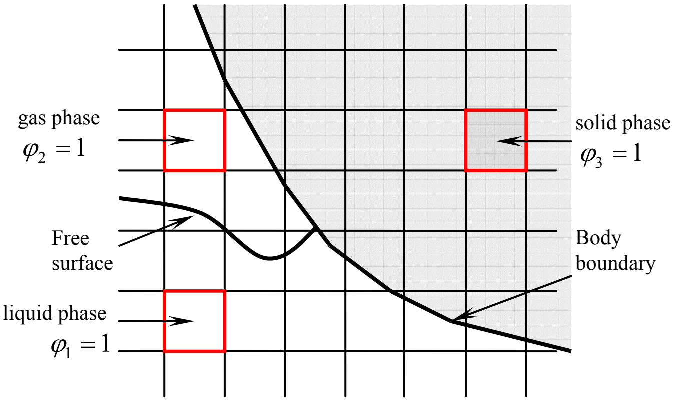

Figure 2.8 Density function φ_m *(m=1,2,3) for multiphase problems with* $0 \le \varphi_m \le 1$ *and* $\varphi_1 + \varphi_2 + \varphi_3 = 1$ *in the computational cells.*

2.4.1 Calculation of the density function for the free surface

The free surface is determined by solving this density function with the CIP method. During the computations, the original sharp interface may become poorly defined with finite thickness due to the numerical diffusivity. However, owing to the sub-cell resolution feature of the CIP scheme, the thickness grows very slowly as the computation proceeds. Therefore, for many cases, it is considered that this degree of interface diffusion is acceptable for computations with the time corresponding to the actual hydrodynamic problems.

However, attempts to overcome this diffusion also result in a number of interface capturing methods, such as VOF (volume of fluid, Hirt and Nichols, 1981), LS (level set method, Sussman et al., 1994) and the CIP method. It has been shown that the CIP coupled with a function transformation method can calculate the free surface without diffusion. Therefore, we can solve the following equation for transformation function Φ instead of Eq. (2.16)

$$\frac{\partial \Phi}{\partial t} + u_i \frac{\partial \Phi}{\partial x_i} = 0 \tag{2.28}$$

Yabe et al. (2001) introduced a tangential function

$$\Phi(\varphi_1) = \tan\left[(1-\varepsilon)\pi(\varphi_1 - 0.5)\right]$$

$$\varphi_1 = \frac{\tan^{-1}\Phi}{(1-\varepsilon)\pi} + 0.5$$

where ε is a small positive constant. A very sharp interface, which means that the thickness of the interface ($\varphi_1 = 0.05 \to 0.95$) is within one or two grid widths, can be obtained by using ε=0.02. The disadvantage of this transformation method is that the originally smooth free surface may become a stepwise function. Further, the numerical calculation of tangential function is time consuming.

Hu (2005) recommended the simpler function transformation as

$$\Phi(\varphi_1) = 0.5 + \alpha(\varphi_1 - 0.5)$$

$$\varphi_1 = 0.5 + (\Phi - 0.5)/\alpha$$

where $\alpha > 1$ is the sharpness enhancement parameter. It was demonstrated that $\alpha = 1.2$ is sufficient to make the thickness of the free surface ($\varphi_1 = 0.05 \to 0.95$) less than 5 grid widths.

As pointed out by Hu (2005), these two transformations described above only work well with the 3rd-order scheme.

Another CIP-based interface capturing method, i.e. CIP-CSL3 (CIP-Conservative Semi-Lagrangian scheme with a 3rd-order polynomial function) scheme is developed. Instead of the spatial derivatives in CIP method, this scheme uses cell-integrated values as the additional constraint to construct a cubic polynomial. Because this scheme introduces a slope control parameter, the sharpness of the density function variation across the interface can be retained in the calculations. Detailed description of the scheme can be found in Xiao & Yabe (2001) and Xiao & Ikebata (2003). The biggest merit of this scheme is the good mass conservation, which is beneficial to long-term computation. Hu et al. (2004) applied this scheme for violent sloshing computation.

2.4.2 Calculation of the density function for rigid body

For the floating body boundary, we consider only the rigid-body case. Instead of the computation using Eq. (2.16), a direct computation method is developed to determine the density function for the solid phase φ_3. The basic idea of this method is to map the geometry information of a moving body to an Earth-fixed Cartesian grid system.

For a rigid body, since the geometry does not change with time, a Lagrangian method is developed to calculate φ_3 to obtain accurate body boundary position without any numerical diffusion. If the solid body can be expressed by an explicit mathematical formula, the treatment is simple. Otherwise, two Lagrangian methods as shown in Figure 2.9 can be used to calculate φ_3. The first method is to use a series of straight line segments to approximate the body surface. The second method is to present the solid body by distributing particles on the surface and it can be extended from 2D to 3D straightforwardly. Furthermore, both non-slip and slip conditions for velocity and the boundary condition for pressure can be obtained by this method.

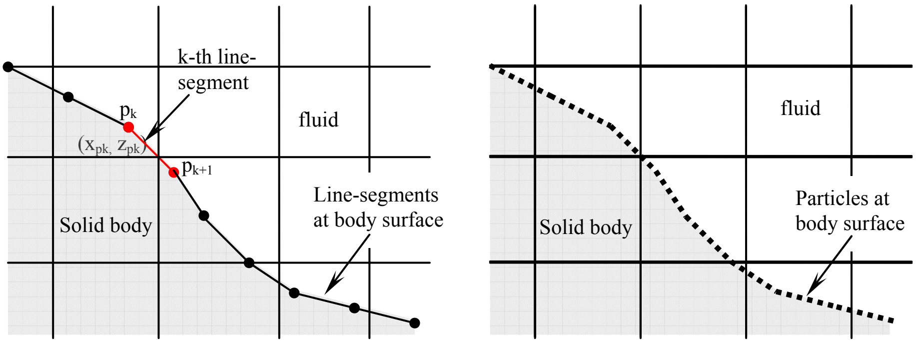

(a) Body surface presented by line segments (b) Body surface presented by particles

Figure 2.9 Lagrangian methods to define a rigid body.

For the two-dimensional case, the main procedure of the first method can be expressed as follows:

- The two-dimensional body boundary is approximated by a series of straight line-segments (p_k, p_{k+1}), k=1,N.

- The coordinates for the end points (x_{pk}, z_{pk}) of the line segments in Figure 2.9(a) are calculated by the following equations:

$$x_{pk} = x_c + (x_{pk}^0 - x_c)\cos\alpha - (z_{pk}^0 - z_c)\sin\alpha \tag{2.29}$$

$$z_{pk} = z_c + (x_{pk}^0 - x_c)\sin\alpha + (z_{pk}^0 - z_c)\cos\alpha \tag{2.30}$$

  where (x_c, z_c) is the mass center of the floating body, α is the roll angle, the superscript 0 denoted the initial value. (x_c, z_c) and α are calculated in a Lagrangian way because the hydrodynamic forces acting on the body can be obtained by the method described in section 2.5.

- All the intersection points (nodes) of line segments and grid lines are then calculated. For each computational cell, if there are more than two nodes, the cell is considered as a boundary cell between the solid body and the air or the water, and the area of the solid body (area of the shadow) in this cell is computed to determine φ_3. Let us see the computational cell in Figure 2.10 where points A and B are the intersection points (nodes) between the line segments and grid lines, then the density function φ_3 for this computational cell can be calculates as

$$\varphi_3(i,j) = \frac{\text{Area of the shadow}}{\text{Area of the cell}}$$

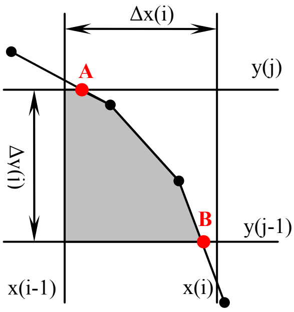

Figure 2.10 Definitions used in the calculation of the density function φ_3 at the interface between the body and the fluid. The shaded area means the area occupied by the solid body in the computational cell.

After density functions for all phases are determined, the physical properties for each computation cell can be determined by the following equation

$$\lambda = \sum_{m=1}^{3} \varphi_m \lambda_m \tag{2.31}$$

where λ denotes the viscosity, sound speed and something else. Under the incompressible fluid assumption, the density can also be determined by Eq. (2.31).

2.4.3 Non-slip condition on the body boundary

For the floating rigid body, a non-slip condition should be satisfied on the body boundary. However, the location of the interface is determined based on the volume fraction information, i.e. density function, unavoidably resulting in an uncertainty in one grid cell. So, it is difficult to apply the non-slip boundary condition at the exact location of the boundary. Hu et al. (2004) introduced two methods to calculate the velocity in the boundary cells.

The first method, which is applied to the calculations in the thesis, determines the velocity in a cell containing the solid phase as

$$\mathbf{U} = \mathbf{U_b}\varphi_3 + \mathbf{u}(1 - \varphi_3)$$

Where $\mathbf{U_b}$ is the local velocity of the body and $\mathbf{u}$ is the velocity obtained by Eq. (2.12). This is a volume fraction weighting treatment for velocity interpolation in the boundary cells. In the numerical procedure, imposing the velocity distribution inside and on the body boundary is equivalent to applying a forcing term $\overline{f_i}$ to the momentum equation Eq. (2.12) as follows:

$$\frac{u_i^{n+1} - u_i^n}{\Delta t} = RHS_i + \overline{f_i}$$

Where RHS_i contains the remaining terms of Eq. (2.12). The forcing term $\overline{f_i}$ is zero in the fluid cells and has the following expression in the solid and boundary cells to satisfy $u_i^{n+1} = U_i^{n+1}$ (non-slip condition) on the body boundary.

$$\overline{f_i} = -RHS_i + \frac{U_i^{n+1} - u_i^n}{\Delta t}$$

The second method is an interpolation method which determines the velocity $\mathbf{U}$ as shown in Figure 2.11 by applying a linear approximation as used by Faldun et al. (2000). The force is given by an imposed velocity $\mathbf{U_0}$ which is obtained by interpolating the local velocity of the body $\mathbf{U_b}$ and the velocity of the neighboring fluid cell $\mathbf{U_1}$.

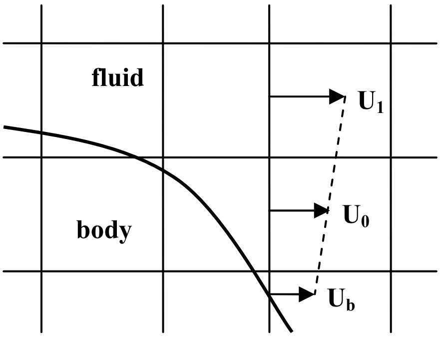

Figure 2.11 Sketch of the velocity interpolation.

Because the outer flow field is essentially independent of the velocity distribution inside the body, the difference between these two methods lies in the way that the imposed velocity at the body boundary is determined.

2.4.4 Absorbing boundary conditions

The numerical wave tank must have a finite size in the simulations. Therefore, the disturbances radiated by the body, as well as the transmitted and reflected waves, may reach the edge of the computational domain within the necessary simulation time. This will cause unphysical reflections and affects the results. In order to prevent the problem and to perform simulations in a finite computational domain over a long time, a non-reflecting boundary condition is required at the downstream boundary of the computational domain to damp out progressively the outgoing wave motions.

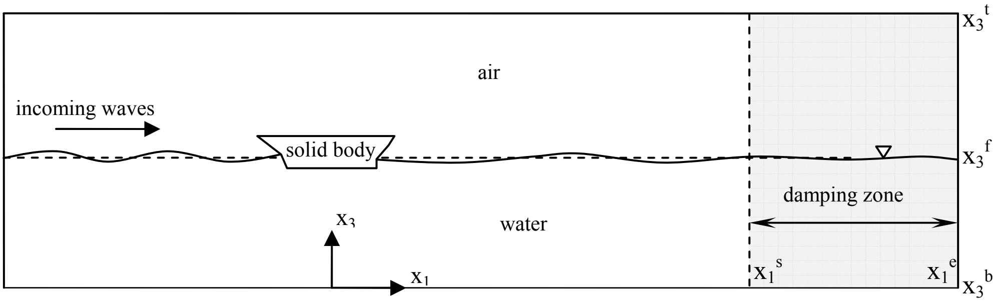

Figure 2.12 Sketch of the damping zone in a numerical wave tank

An artificial damping zone shown in Figure 2.12 is placed at the downstream boundary ($x_1^s < x_1 < x_1^e$, $x_3^b < x_3 < x_3^t$), and an artificial damping force is added to the body force term of Eq. (2.12), which is expressed as follows:

$$f_{di} = \alpha \left(\frac{x_1 - x_1^s}{x_1^s - x_1^e} \right)^m \left(1 - \left| \frac{x_3 - x_3^f}{x_3^t - x_3^b} \right| \right)^n u_i \delta_{i3} \tag{2.32}$$

where:

x_1^s, x_1^e and x_3^b, x_3^t denote the positions of the damping zone boundaries;

x_3^f is the average free surface position;

$$\delta_{i3} = \begin{cases} 1 & i = 3 \\ 0 & else \end{cases}$$

The constants in Eq. (2.32) are determined in Hu & Kashiwagi (2004) with $\alpha = 0.5/\Delta t$, m=4 and n=1 and are used in all the calculations in this thesis.

2.5 Hydrodynamic forces on the floating body

The hydrodynamic force acting on a floating rigid body, i.e. F_i, can be calculated by integrating the pressure and skin friction along the body surface.

$$F_i = F_i^{(p)} + F_i^{(v)} = \iint_A (-p\delta_{ik}) n_k dA + \iint_A 2\mu S_{ik} n_k dA \tag{2.33}$$

where A denotes the surface of the floating body and n_k is the k-th component of outward unit normal vector. By applying Gauss theorem, Eq. (2.33) can be rewritten as

$$F_i = -\iiint_\Omega \frac{\partial p}{\partial x_i} \varphi_3 d\Omega + \iiint_\Omega \frac{\partial}{\partial x_k} \left(2\mu S_{ik} \right) \varphi_3 d\Omega \tag{2.34}$$

If only the pressure needs to be considered, i.e. the skin friction is relatively small and can be neglected, we have

$$F_i = F_i^{(p)} = \iint_A (-p\delta_{ik}) n_k dA = -\iiint_V \frac{\partial p}{\partial x_i} dV = -\iiint_\Omega \frac{\partial p}{\partial x_i} \varphi_3 d\Omega \tag{2.35}$$

where V and Ω denote the space occupied by the body and the whole computational domain, respectively. The advantage of using Eq. (2.35) is that we do not need to know the exact position and orientation of the boundary surface for calculation of the unit normal vector. As the pressure in the whole computation domain can be calculated by Eq. (2.22). Equation (2.35) provides a very simple and robust way to compute the hydrodynamic forces acting on the moving body in the fixed Cartesian grid system. For instance, for a two-dimensional problem, the force and the moment acting on the floating body can be written as follows

$$\begin{aligned} F_x &= -\iiint_{\Omega} \frac{\partial p}{\partial x} \varphi_3 d\Omega \\ F_z &= -\iiint_{\Omega} \frac{\partial p}{\partial z} \varphi_3 d\Omega \\ M_y &= -\iiint_{\Omega} \left[(x - x_c)\frac{\partial p}{\partial z} - (z - z_c)\frac{\partial p}{\partial x} \right] \varphi_3 d\Omega \end{aligned} \tag{2.36}$$

2.6 Equations of motions

After the hydrodynamic forces are obtained, it is not difficult to calculate the translational and the rotational velocity of the rigid body. The position (x_c, z_c) of the mass center in the Earth-fixed coordinate system and the roll angle α can be obtained by the following equations of motion

$$\frac{d^2 x_c}{dt^2} = \frac{F_x}{m} \qquad \frac{d^2 z_c}{dt^2} = \frac{F_z}{m} \qquad \frac{d^2 \alpha}{dt^2} = \frac{M_y}{I} \tag{2.37}$$

Where *m* is the mass per unit length of the body and *I* is the inertia moment per unit length about the mass center.

These equations of motion above can be solved by a fourth-order Runge-Kutta scheme shown in Eqs. (2.38) and (2.39) where y is the variable of interest, i.e. x_c, z_c and α in Eq. (2.37). If we have

$$\frac{d^2 y}{dt^2} = \ddot{y} = b\left[y, \dot{y}\right]$$

By using

$$b_1 = b\left[y_n, \dot{y}_n\right]$$

$$b_2 = b\left[y_n + \dot{y}_n \tfrac{\Delta t}{2} + b_1 \tfrac{(\Delta t)^2}{8}, \dot{y}_n + b_1 \tfrac{\Delta t}{2} \right]$$

$$b_3 = b\left[y_n + \dot{y}_n \tfrac{\Delta t}{2} + b_1 \tfrac{(\Delta t)^2}{8}, \dot{y}_n + b_2 \tfrac{\Delta t}{2} \right]$$

$$b_4 = b\left[y_n + \dot{y}_n \Delta t + b_3 \tfrac{(\Delta t)^2}{2}, \dot{y}_n + b_3 \Delta t \right]$$

we can obtain the following

$$\dot{y}_{n+1} = \dot{y}_n + \tfrac{\Delta t}{6}\left[b_1 + 2b_2 + 2b_3 + b_4 \right] + O\left[(\Delta t)^5 \right] \tag{2.38}$$

$$y_{n+1} = y_n + \dot{y}_n \Delta t + \tfrac{(\Delta t)^2}{6}\left[b_1 + b_2 + b_3 \right] + O\left[(\Delta t)^5 \right] \tag{2.39}$$

2.7 Summary

The method described in this chapter is applied to solve the fully nonlinear wave-body interaction problem.

- The method is a CIP-based finite difference method. The acronym CIP is related to the solution of the advection phase in the numerical time-stepping procedure.

- The wave-body interaction problem is treated as a multiphase problem which has a liquid phase (water), a gas phase (air) and a solid phase (solid body). Density functions φ_m (m=1, 2, 3) with $0 \le \varphi_m \le 1$ and $\varphi_1 + \varphi_2 + \varphi_3 = 1$ are introduced to identify which part is the air, the water or the solid body.

- The problem is numerically solved in an Earth-fixed Cartesian grid system. An artificial problem is solved inside the solid body.

- The free surface and the body boundary are immersed in the computational domain.

- The pressure for the whole computational domain including the interior field of the solid body is calculated by one set of equations.

CHAPTER 3

2D linear and weakly nonlinear wave-body interaction problems

---

3.1 Introduction

Practical state-of-the-art computational tools for nonlinear wave-induced motions and loads on a ship handle the nonlinear effects in a simplistic way. The numerical codes typically assume irrotational flow of incompressible water. The Froude-number-dependent trim angle and proper handling of the interaction between the steady and unsteady flows have increased importance with increasing Froude number. Lugni et al. (2004) demonstrated both experimentally and numerically the importance of nonlinear effects in the steady flow around monohulls and catamarans at Froude numbers higher than 0.5. Further, the predicted linear wave-induced heave and pitch motions were sensitive to how the interaction between the unsteady and steady flows was handled. Their studies included Froude numbers down to 0.3.

Viscous flow separation effects are important for accurate resonant roll predictions of monohulls at low and moderate Froude number. This represents a nonlinear effect and has to be handled by an empirical viscous roll damping model in a potential flow code. Nonlinear vertical potential flow forces and pitch moments are typically handled by considering nonlinear Froude-Kriloff and hydrostatic restoring terms and including terms involving the time rate of change of heave added mass. This nonlinear method is combined with a linear time domain strip theory. It is common to use convolution integrals to express the linear hydrodynamic loads due to the ship motions. Even though it appears simplistic, the method may be able to predict correctly the nonlinear trends in, for instance, the midships vertical bending moment. This was documented in a comparative study organized by ISSC for the S-175 container ship in regular head sea conditions at Froude numbers 0.2 and 0.275 (Jensen et al., 2000). An advantage of a simplistic nonlinear method based on strip theory is the practical ability to perform simulations in a stochastic sea to obtain probability density functions of response variables. A nonlinear system requires typically more realizations of a sea state than a linear system in order to obtain reliable predictions of extreme value response.

A simplistic approach as described above is combined with separate calculations for slamming loads on, for instance, a bow flare section. The state of the art in prediction of slamming loads on a ship cross-section with given inflow conditions and body motions and based on 2D flow is generally satisfactory. However, a challenge is to incorporate the slamming predictions in the global ship motion calculations. Because the slamming loads can be sensitive to the inflow conditions, an integrated approach is needed. This requires special considerations when the slamming duration is so short that local hydroelastic effects matter. If bow flare slamming is considered, an intermediate step towards a fully 3D solution could be a nonlinear 2D+t approach. The ship passes through a set of transverse Earth-fixed cross-planes and a time-dependent 2D problem is solved in each cross-plane. The procedure requires a slender ship and that $U/\sqrt{gx}$ is higher than ≈0.4. Here U is the forward speed of the ship and x is the longitudinal distance along the ship with x=0 corresponding to the bow. It implies that the procedure can only be applied for the whole ship in the case of Froude number larger than ≈0.4.

Another challenge associated with the above-mentioned simplistic approach is to evaluate green water loads. This may, for instance, be attempted by calculating the relative vertical motions along the deck and then using a dam-breaking model to predict the behavior of the water on the deck. The resulting loads on equipment and deck house have to be done by separate calculations. There are several shortcomings with a model such as this. One is the accuracy of the predictions of the relative vertical motions and proper accounting of the steady-flow effect. Another factor is that a dam-breaking model is not always adequate to describe the behavior of the green water. We will discuss this later in Chapter 7.

Careful validation and verification of the CIP-based finite difference method are needed in order to make a rational step in improving calculations of nonlinear wave-induced ship motions and loads. Therefore, in this chapter we will deal with linear and weakly nonlinear cases. Our studies in this chapter are limited to 2D flow and we do not consider the effect of forward speed.

3.2 Convergence study

In order to investigate the convergence of our CIP-based finite difference method, the small-amplitude heave motion of a nearly rectangular cross-section shown in Figure 3.1 and Table 3.1 is studied by varying the following parameters:

- Grid size
- Timestep size
- Computational domain
- Damping zone

Table 3.1 Principal data for the rectangle used in Vugts (1968)

Length (L)	4.19m
Breadth (B)	0.40m
Draft (D)	0.20m
Area coefficient	0.9992
Displacement	335.2kgf
Water depth	1.8m

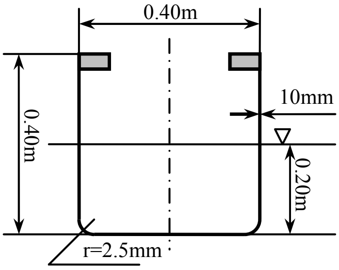

Figure 3.1 The cross-section of the nearly rectangular cylinder used in Vugts (1968).

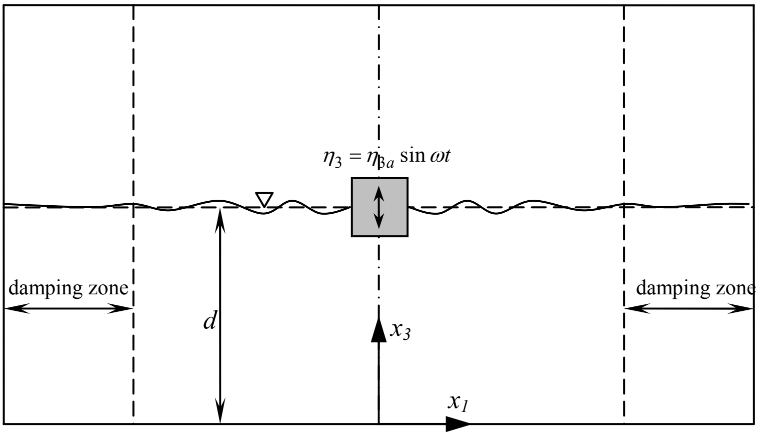

Figure 3.2 The whole computational domain used in the CIP calculations. Two artificial damping zones are placed on both ends of the numerical wave tank to damp outgoing waves.

If long time simulations are performed, and the amplitude and frequency of the oscillations are constant, the hydrodynamic force acting on the body will eventually reach steady state. Our focus is first on the linear steady-state hydrodynamic force. The part of the force in opposite phase with the acceleration of the body is defined as the added mass force, while the part in opposite phase with the velocity of the body is the hydrodynamic damping force. Further, there are dynamic restoring forces caused by changes in the hydrostatic pressure distribution. If the harmonic oscillation of the body in the i-direction is given as η_i, the hydrodynamic steady state force in the j-direction in the linear problem can be written as

$$F_j = -A_{ji}\ddot{\eta}_i - B_{ji}\dot{\eta}_i - C_{ji}\eta_i \tag{3.1}$$

where A_{ji}, B_{ji} and C_{ji} are defined as the added mass, damping and restoring coefficients, respectively. For instance, for our considered heave problem, $C_{33} = \rho g B$ where B is the breadth of the cross-section. Added mass and damping coefficients are easily evaluated from the force history.

Vugts (1968) presented linear numerical results for added mass and damping coefficient for cylinders with different cross-sections oscillating on the free surface. The closefit technique by De Jong (1967, 1973) and the Lewis form technique were used. Both methods are based on conformal transformation of the cross-section to a semi-submerged circular cylinder. The circular cylinder problem in the auxiliary plane is solved by Ursell's (1949) method. The closefit technique gives a better geometrical description of the cross-section shape than the Lewis form technique. By Lewis form is implied that only the beam, draft and the cross-sectional area are needed as input. The comparisons between these two theoretical calculations demonstrated that the differences are generally not of much importance for the tested sections.

Vugts (1968) reported the results of the cylinder with rectangular cross-section for different B/D-ratios, i.e. 2, 4 and 8. Here B is the breadth of the cross-section and D is the draft. In this thesis, we consider the harmonic heave motion $\eta_3 = \eta_{3a} \sin \omega t$ of the rectangle with B/D=2. The numerical wave tank with artificial damping zones used in the CIP calculations is shown in Figure 3.2. A wide range of frequencies as shown in Table 3.2 is tested.

For 'deep water', i.e. h/λ > 0.5 where h is the water depth, we have the following relations:

$$\omega^2 = gk = 2\pi g / \lambda$$

$$C_w = \lambda / T = \omega / k = \sqrt{g\lambda/2\pi}$$

$$C_g = 0.5 C_w$$

The finite water depth relationships are

$$\omega^2 = gk \tanh kh\ , \ k = 2\pi / \lambda$$

$$C_w = \lambda / T = \omega / k$$

$$C_g = \frac{d\omega}{dk} = \frac{C_w}{2}\left(1 + \frac{2kh}{\sinh 2kh}\right)$$

Here C_w is the phase velocity and C_g is the group velocity. Table 3.2 presents the numerical values. Because we choose h = 1.8m corresponding to the experimental tank used by Vugts (1968) in all the calculations, this means that the cases with $\lambda < 3.6$m or $\omega\sqrt{B/2g} > 0.5$ can be considered as deep water problems.

Table 3.2 Detailed parameters of the test cases for heave added mass and damping of the nearly rectangular section shown in Figure 3.1.

Non-dimensional wave frequency	Wave frequency	Wave period	Wave length	Phase velocity	Group velocity
$\omega\sqrt{B/2g}$	ω (rad/s)	T(s)	λ (m)	C_w (m/s)	C_g (m/s)
0.25	1.75	3.590	13.668	3.807	3.153
0.50	3.50	1.795	4.930	2.746	1.501
0.75	5.25	1.197	2.236	1.868	0.934
1.0	7.0	0.898	1.258	1.401	0.700
1.25	8.75	0.718	0.805	1.121	0.560
1.50	10.5	0.598	0.559	0.935	0.468

Table 3.3 Reference parameters used in the CIP calculations of heave added mass and damping of a nearly rectangular cross-section.

Computational domain with damping zones	length × height	76m×3m
Minimum non-dimensional horizontal grid size	min(Δx/B)	1/200
Minimum non-dimensional vertical grid size	min(Δy/B)	1/200
Total number of computational cells	NX × NY	500×200
Non-dimensional timestep size	Δt/T	1/2000
Amplitude of heave motion	η_{3a}	0.03m

The numerical grid used in the CIP calculations is rectangular with horizontal and vertical lengths Δx and Δy (see Figure 2.5 and Figure 2.10). The smallest values are used near the body surface and the free surface. The minimum non-dimensional lengths in the calculations are min(Δx/B)=1/200, min(Δy/B)=1/200. The computational domain has a length and height of 76m and 3m, respectively. The total number of the computational cells is 500×200. The timestep size is $\Delta t/T=1/2000$ where $T=2\pi/\omega$ is the period of the heave motion. The damping zones longer than 10m are placed at both sides of the numerical wave domain. The amplitude of the harmonic heave motion η_{3a} is 0.03m. All the parameters mentioned above are shown in Table 3.3 and taken as the reference parameters in the following convergence study.

3.2.1 *Influence of grid size*

In order to check the influence of the grid size on the numerical results, three kinds of grid sizes shown in Table 3.4 are used in the calculations. Figure 3.3 (a) shows that the results of the heave added mass are close for the small and reference grid sizes, and have small differences for the large grid size. However, the results of the heave damping coefficient in Figure 3.3(b) do not have the same trend, i.e. for $\omega\sqrt{B/2g}\geq 1$, the small grid size and the large grid size give similar results which are larger than the results of the reference grid size, and for $\omega\sqrt{B/2g}<1$, the small and reference grid sizes give similar results which are smaller than the results of the large grid size. The possible reasons are the sensitivity in estimating the damping part and the precision in the numerical calculations, which are discussed later on in Section 3.3.3.

Table 3.4 Different grid sizes used in the CIP calculations of the heave added mass and damping coefficients of a nearly rectangular cross-section.

	min(Δx/B)	min(Δy/B)
Small grid size	1/400	1/400
Reference grid size	1/200	1/200
Large grid size	1/100	1/100

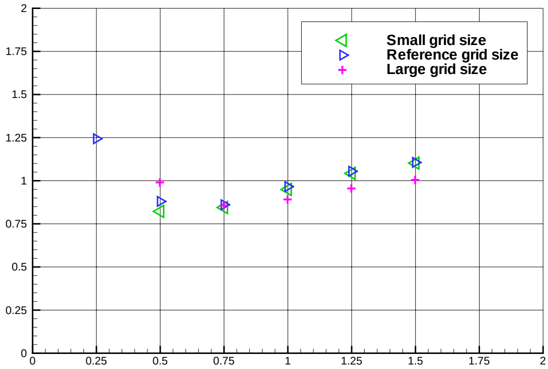

(a) Added mass coefficient

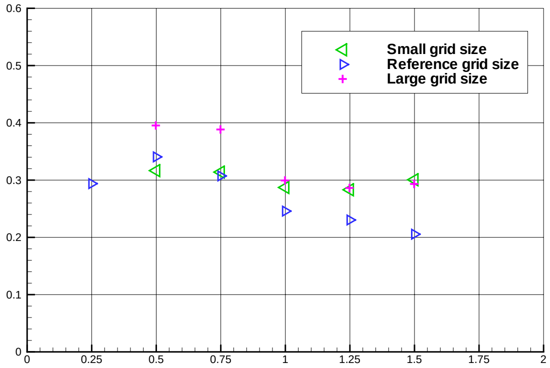

(b) Damping coefficient

Figure 3.3 Non-dimensional heave added mass $A_{33}/\rho A$ *and damping* $(B_{33}/\rho A)\sqrt{B/2g}$ *as a function of* $\omega\sqrt{B/2g}$ *for different grid sizes.* $\eta_{3a} = 0.03m$.

3.2.2 *Influence of timestep size*

Similarly, in order to investigate the influence of timestep size on the numerical results, two kinds of timestep sizes are used in the calculations. For small (reference) timestep size, Δt/T=1/2000. For large timestep size, Δt/T=1/1000. T=2π/ω is the period of the heave motion. From Figure 3.4(a), we can see that the timestep size has negligible influence on the numerical results of the heave added mass. However, the influences on the damping coefficient are not negligible, which can be seen in Figure 3.4(b). The possible reasons are similar as previously stated.

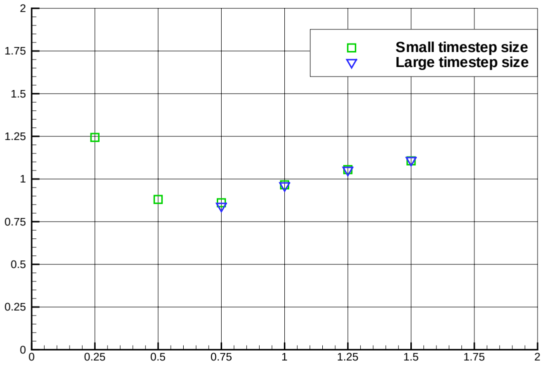

(a) Added mass coefficient

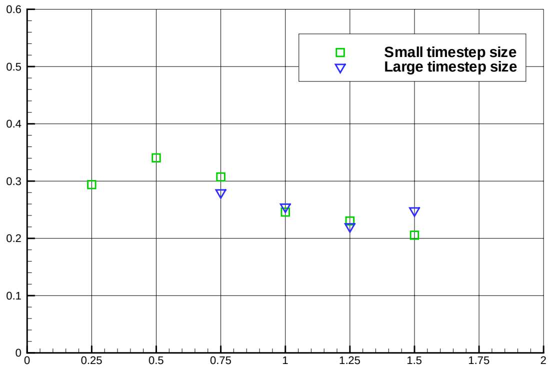

(b) Damping coefficient

Figure 3.4 Non-dimensional heave added mass $A_{33}/\rho A$ *and damping* $(B_{33}/\rho A)\sqrt{B/2g}$ *as a function of* $\omega\sqrt{B/2g}$ *for different timestep size.* $\eta_{3a} = 0.03m$.

3.2.3 *Influence of computational domain*

The influence of computational domain is investigated by varying the total length of the numerical wave tank. The length of the numerical wave tank including the damping zone is 28m for the small computational domain, 76m for the reference computational domain, and 124m for the large computational domain. Figure 3.5(a) shows that the different computational domains give negligible differences on the numerical results of the heave added mass. From Figure 3.5(b), we can see that the small and large domains give similar results of the heave damping, which are larger than the results calculated in the reference domain. This is believed to be due to the sensitivity in estimating the damping part and the precision in the numerical calculations as previously stated.

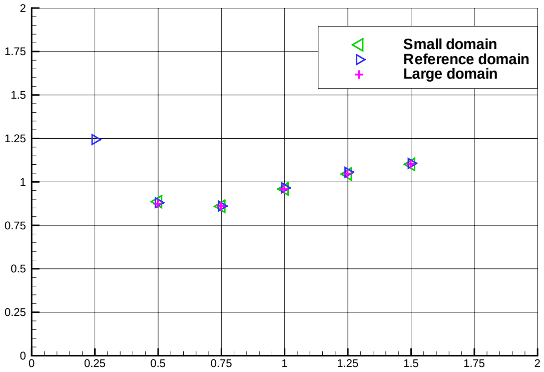

(a) Added mass coefficient

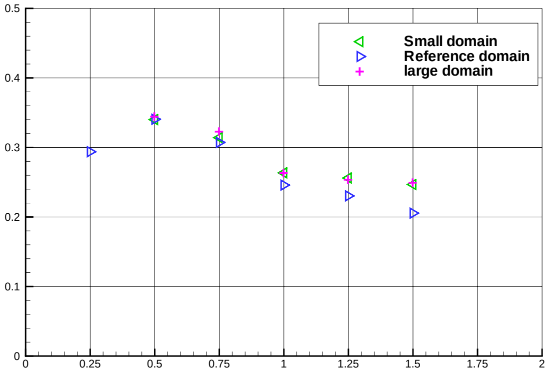

(b) Damping coefficient

Figure 3.5 Non-dimensional heave added mass $A_{33}/\rho A$ *and damping* $(B_{33}/\rho A)\sqrt{B/2g}$ *as a function of* $\omega\sqrt{B/2g}$ *for different computational domain.* $\eta_{3a} = 0.03m$.

3.2.4 Influence of damping zone

In order to perform the long-time simulations in the numerical wave tank, we can either use a large computational domain or use a finite computational domain with an artificial damping zone to damp the outgoing waves. We simulate these two conditions to see how the damping zone influences the numerical results. Figure 3.6 shows the comparison of the results with and without the damping zone for the reference computational domain. The results of the heave added mass have negligible differences. This may be due to the fact that the computational domain without damping zone is also large enough to avoid the effects from both sides of the numerical wave tank. The computational domain without damping zone gives larger heave damping coefficients than the computational domain with damping zone. The possible reasons are stated in Section 3.2.1.

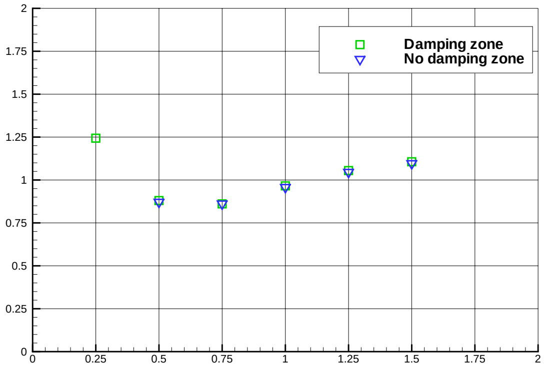

(a) Added mass coefficient

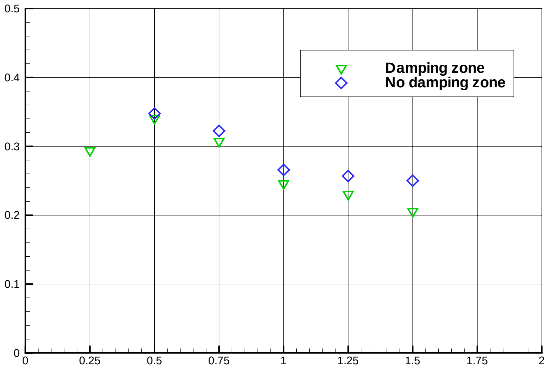

(b) Damping coefficient

Figure 3.6 Non-dimensional heave added mass $A_{33}/\rho A$ *and damping* $(B_{33}/\rho A)\sqrt{B/2g}$ *as a function of* $\omega\sqrt{B/2g}$ *for different damping condition in the reference computational domain.* $\eta_{3a} = 0.03m$*. The length of the computational domain is 76m.*

Therefore, we will compare the results with and without the damping zone for a very small computational domain of length 4.4m. From Figure 3.7, we can observe negligible differences for $\omega\sqrt{B/2g} \geq 1$ and non-negligible differences for $\omega\sqrt{B/2g} <1$. This is because the reflected wave front does not reach the cylinder within the computational duration for $\omega\sqrt{B/2g} \geq 1$, i.e. the ratio between the length of the numerical wave tank and the wavelength is large enough to avoid the reflected wave effects from both ends of the tank. However, for $\omega\sqrt{B/2g} <1$, the wave reflected from the side of the tank will influence the hydrodynamic force acting on the cylinder, and consequently influence the hydrodynamic coefficient.

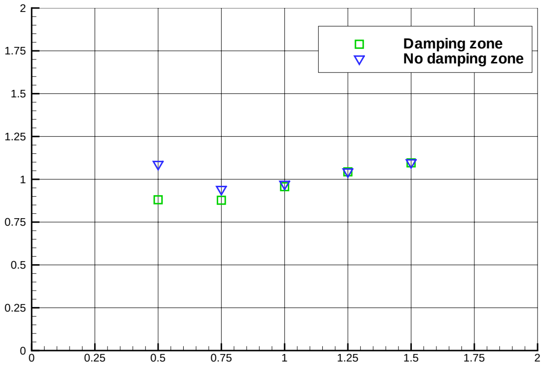

(a) Added mass coefficient

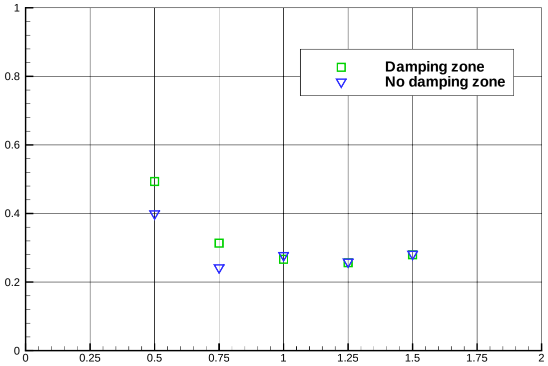

(b) Damping coefficient

Figure 3.7 Non-dimensional heave added mass $A_{33}/\rho A$ *and damping* $(B_{33}/\rho A)\sqrt{B/2g}$ *as a function of* $\omega\sqrt{B/2g}$ *for different damping condition.* $\eta_{3a}=0.03m$. *The length of the computational domain is 4.4m.*

3.3 Verification and validation

3.3.1 Linear numerical results by Vugts and BEM

Figure 3.8 shows the comparisons of the heave added mass and damping coefficients between the results by the boundary element method (BEM) and the deep-water numerical results by Vugts (1968). Both methods assume linear potential flow. The BEM results are calculated by using a code modified by the author from Greco's (2001) code. The parameters used in the calculations are as follows: the water depth of the tank was 1.8m, the cylinder was placed 10m away from the wavemaker which was located on the left side of the tank, a 10m damping zone was placed 5m away from the cylinder at the downstream boundary. The whole computational domain was discretized into 40 elements on the body surface, 320 elements on the free surface including the damping zone and 190 elements on the outer control boundary. This high number of elements is expected to give accurate numerical results.

From Figure 3.8 we can see that the results of added mass and damping coefficients by the BEM agree well with the linear numerical results by Vugts (1968) except in the vicinity of $\omega\sqrt{B/2g}=0.25$. The reason is the effect of finite water depth. However, the finite water depth effect is not very important for the considered frequencies. This gives some confidence in the linear numerical results by Vugts according to potential flow. We use later on these linear potential flow results by Vugts as a reference for our CIP calculations.

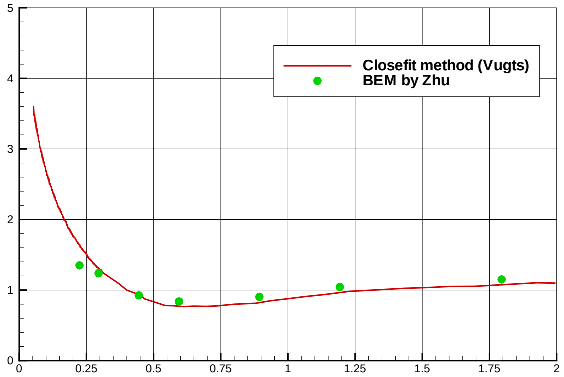

(a) Added mass coefficient

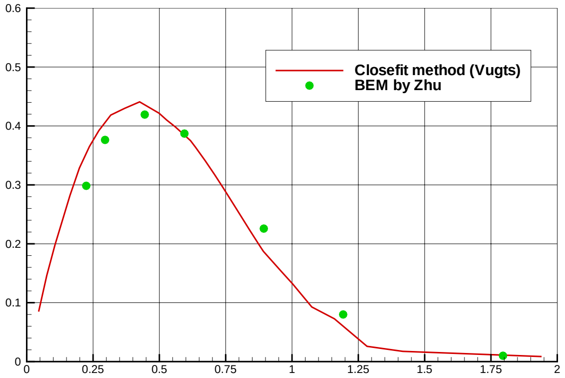

(b) Damping coefficient

Figure 3.8 Non-dimensional heave added mass $A_{33}/\rho A$ *and damping* $(B_{33}/\rho A)\sqrt{B/2g}$ *as a function of* $\omega\sqrt{B/2g}$ *by BEM and closefit method by Vugts. A denotes the submerged cross-sectional area.*

3.3.2 Verification and validation

In this section, we will compare our numerical results of the heave added mass and damping coefficients with the experimental and linear numerical results by Vugts. Non-dimensional heave amplitudes $\eta_{3a}/D=1/20$, 2/20 and 3/20 are used. Here D is the draft which is 0.20m, i.e. the amplitude of the heave motion will be 0.01m, 0.02m and 0.03m, respectively.

Figure 3.9 shows the comparisons of the heave added mass and damping coefficients between the experimental results and the linear numerical results by the closefit method in Vugts (1968) and the numerical results by the CIP method.

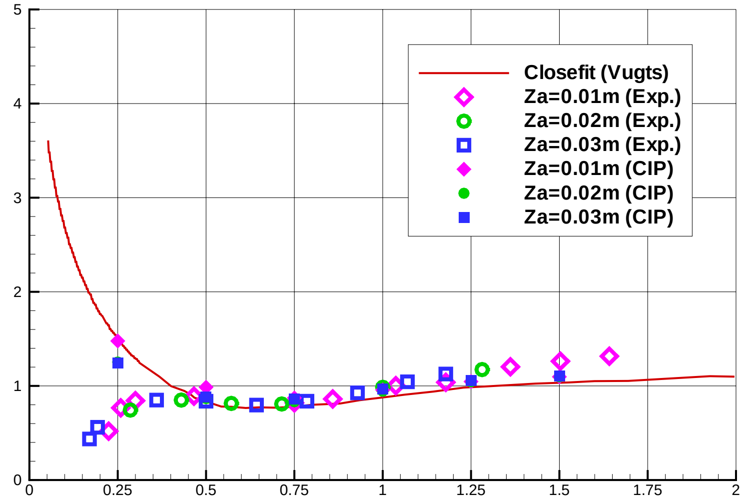

(a) Added mass coefficient

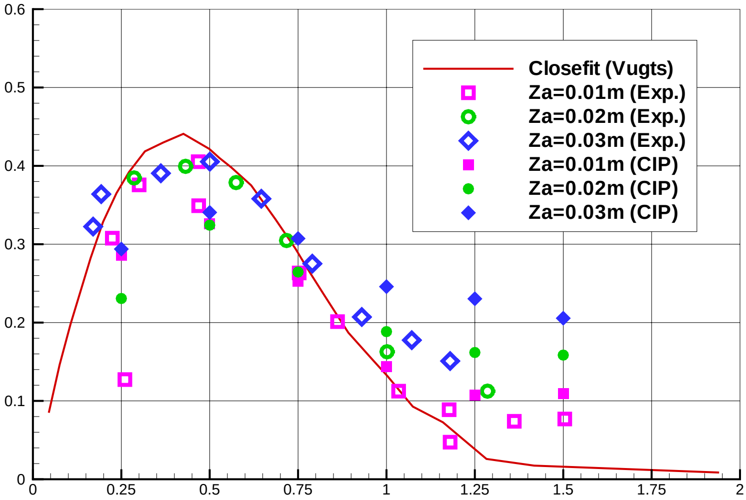

(b) Damping coefficient

Figure 3.9 Comparisons of the experimental, numerical and linear numerical results of the non-dimensional heave added mass $A_{33}/\rho A$ *and damping* $(B_{33}/\rho A)\sqrt{B/2g}$ *for different amplitudes of heave motion as a function of* $\omega\sqrt{B/2g}$. $Z_a = \eta_{3a}$ *= the heave amplitude. A = the submerged cross-sectional area.*

Vugts (1968) stated that in the low frequency range, i.e. $\omega\sqrt{B/2g}<0.5$, the experimental results deviate from the linear numerical results by the closefit method due to the experimental inaccuracies especially in the added mass. A reason is believed to be the decreasing magnitude of the added mass force with decreasing frequency. Further, the experimental results are slightly higher than the linear numerical results at the higher frequency side. The overall agreement between the experiments and the linear numerical results is satisfactory. Further, the CIP results are in general satisfactory agreement with the linear potential flow results. The differences will be discussed below.

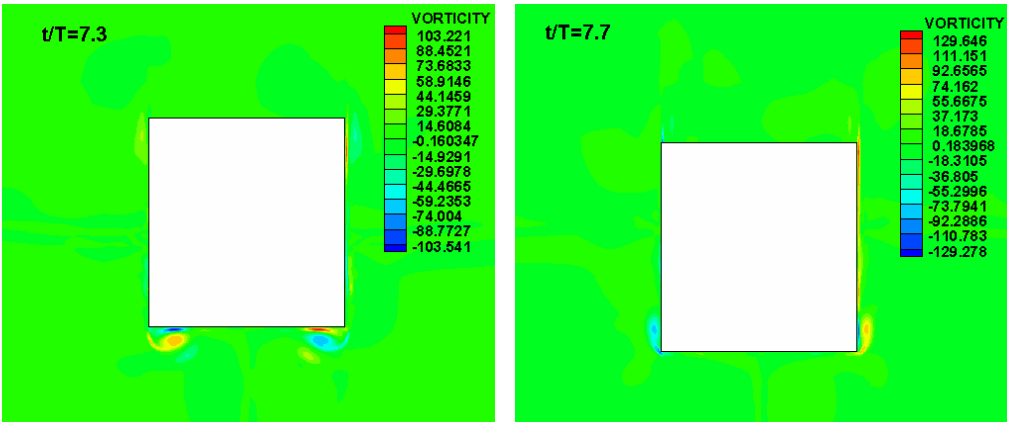

Figure 3.10 Numerically predicted vorticity field at t/T=7.3 and t/T=7.7 for a square section oscillating in the free surface with B/D=2. $\eta_{3a} = 0.03m$. *The dimension of the vorticity is* s^{-1}.

Because the ratio between the heave amplitude and the draft, i.e. η_{3a}/D, is small, one would expect *a priori* that linear effects dominate. This means that the considered heave amplitudes show a small influence on the added mass and damping coefficients. This is true for the added mass as shown in Figure 3.9(a) except for the small frequencies $\omega\sqrt{B/2g} = 0.25$ and 0.5. The results for the smallest amplitude ought to be closest to the linear potential flow results. However, this is not true for $\omega\sqrt{B/2g} = 0.25$ and 0.5. When it comes to $\omega\sqrt{B/2g} = 0.25$, we should have in mind the finite water depth effects and rather compare with the BEM results in Figure 3.8.

The variation in the damping coefficients as a function of the considered heave amplitudes is not negligible for $\omega\sqrt{B/2g} \geq 1$. A reason for this is decreasing wave generation with increasing frequency and the presence of vortex shedding from the sharp corners which can be seen from Figure 3.10. We are here considering the double-body in infinite fluid. The associated drag force can be expressed as $-\frac{1}{2}\rho B C_D |\dot{\eta}_3| \dot{\eta}_3$. Therefore, the vertical hydrodynamic force expressed by Eq. (3.1) can be corrected by accounting for the drag force

$$F_3 = -A_{33}\ddot{\eta}_3 - B_{33}\dot{\eta}_3 - C_{33}\eta_3 - \tfrac{1}{2}\rho B C_D \left|\dot{\eta}_3\right|\dot{\eta}_3 \qquad (3.2)$$

We will here associate B_{33} with wave generation and C_D with viscous effects. Strictly speaking, viscous effects can also cause a linear hydrodynamic force component. However, Braathen (1987) showed by using a thin free-shear layer model that vortex shedding had a small effect on wave generation. On the contrary, wave generation has a clear effect on vortex shedding. The latter implies that C_D is frequency dependent.

We will now focus our attention on the high frequencies. Wave generation is then small. We start with showing the equivalence between the studied problem and the flow past a double-body in infinite fluid. This enables us to compare with other published data.

Because the heave motion is small relative to the cross-sectional draft, it is reasonable to linearize the free surface conditions. We assume the vorticity is concentrated in thin boundary layer and free shear layers close to the corners of the rectangular cross-section. The fluid flow outside the vorticity regions can be considered by a velocity potential φ. The consequence is the following linearized free surface condition for steady-state conditions

$$-\omega^2\varphi + g\frac{\partial\varphi}{\partial z} = 0 \quad \text{on } z=0 \qquad (3.3)$$

When the frequency ω is very high and fluid accelerations are much higher than the gravitational acceleration g, we can neglect the second term on the right-hand-side of Eq. (3.3). Then, the free surface condition can be simplified as $\varphi=0$ on the mean free surface. This property together with the fact that we consider the heave motion allows us to study the double body problem, i.e. we consider forced heave oscillations of the sum of the submerged body and its mirror image above the free surface.

Because the velocity potential φ is constant on z=0, the velocity cannot be horizontal along the free surface and has to be vertical, i.e. the body cannot generate any free-surface waves and no energy is carried away to infinity. Then, the damping term associated with wave generation, i.e. the second term on the right-hand-side of Eq. (3.3) can be neglected. So, we can compare our numerical results with the theoretical, numerical and experimental results for 2D flow around a rectangular section in infinite fluid.

Then, we can associate Eq. (3.2) with Morison's equation (Morison et al., 1950) which is often used to calculate wave loads on circular cylindrical structural members of fixed offshore structures when viscous forces matter, and generalize it to express the vertical hydrodynamic force acting on a horizontal rectangular cylinder with heave motion $\eta_3 = \eta_{3a}\sin\omega t$ (Faltinsen, 1990). The vertical force F_3 per unit length of the rectangular cylinder can be represented as

$$F_3 = -\rho(C_M - 1)S\ddot{\eta}_3 - \tfrac{1}{2}\rho C_D B\left|\dot{\eta}_3\right|\dot{\eta}_3 \qquad (3.4)$$

where ρ is the fluid density, S is the volume displacement per unit length, B is the width of the cylinder normal to the flow direction, and C_M and C_D are the inertia and drag coefficients, respectively. The drag coefficient C_D and added mass coefficient C_A can be obtained by the following formulas according to Keulegan-Carpenter (1958)

$$C_D = -\frac{3\omega}{4\rho BU_m^2}\int_0^T F(t)\cos(\omega t)dt = -\frac{3\pi}{4\rho BU_m^2}\left(\frac{2}{T}\int_0^T F(t)\cos(\omega t)dt\right) \quad (3.5)$$

$$C_A = C_M - 1 = \frac{1}{\pi\rho SU_m}\int_0^T F(t)\sin(\omega t)dt = \frac{1}{\omega\rho SU_m}\left(\frac{2}{T}\int_0^T F(t)\sin(\omega t)dt\right) \quad (3.6)$$

where $U_m = \omega\eta_{3a}$ is the amplitude of the oscillation velocity, $F(t)$ is the time history of the hydrodynamic force per unit length which should be two times of the hydrodynamic force calculated by the CIP method excluding the restoring force for the rectangular section in the free surface. The inertia coefficient of the cylinder can be calculated as $C_M = 1 + C_A$.

For all the considered cases with $\omega\sqrt{B/2g}=1.5$, we obtain that $C_A \approx 1.1$ which is close to the theoretical value $C_A = 4.754/4 = 1.1885$ given by Newman (1977) for a square in an infinite fluid based on potential flow.

For $\omega\sqrt{B/2g}=1.5$, we obtained the following C_D-values:

$C_D \approx 4.8$	Experimental results by Vugts (1968) for η_{3a}=0.01m
$C_D \approx 6.8$	Numerical results by the CIP method for η_{3a}=0.01m
$C_D \approx 5.0$	Numerical results by the CIP method for η_{3a}=0.02m
$C_D \approx 4.3$	Numerical results by the CIP method for η_{3a}=0.03m

There should theoretically be small influence of the heave amplitude on the C_D-value for a rectangular section in infinite fluid at small KC-numbers $\pi\eta_{3a}/D$ (Graham, 1980). This assumes negligible influence of shear stress which is true in our calculations. We note that the experimental results for η_{3a} = 0.01m, and the CIP results for η_{3a} = 0.02m and 0.03m show nearly the same results. However, the CIP results for η_{3a} = 0.01m is clearly different. Further, the experimental C_D-value of 3.0 obtained by Bearman et al. (1984) for a facing square in infinite fluid is clearly lower than our numerical and Vugts' experimental results. Possible numerical error sources are discussed below.

3.3.3 *Numerical error sources*

- The influence of the bilge radius *r*

A possible error is the influence of the bilge radius, which is neglected in our computations. Faltinsen (1989) documented that the bilge radius r has an effect on the drag coefficient and that increasing the bilge radius means decreasing the drag coefficient for 2D nearly rectangular sections in infinite fluid. However, the influence is very small when the ratio $2r/B$ is smaller than approximately 0.05. The bilge radius and the width of the rectangular cylinder used in the calculations are 0.0025m and 0.4m respectively, so we have $2r/B = 0.00625$ which is too small to influence the drag coefficient. Further, because the bilge radius of the rectangular cylinder is close to the smallest vertical grid size and even smaller than the smallest horizontal grid size in the numerical simulations, the effect of the bilge radius will not show up in the numerical results of the vertical hydrodynamic force.

- The influence of wave generation

The combined effect of wave generation and vortex shedding will influence the numerical results. How big the influence of the wave generation is at the largest examined frequency will be assessed qualitatively in the following way. By assuming no viscous effect, the damping coefficient can by energy conservation (Faltinsen, 1990) be calculated by

$$B_{33}=\rho\left(\frac{A_3}{|\eta_3|}\right)^2\frac{g^2}{\omega^3} \tag{3.7}$$

where A_3 is the far-field wave amplitude. For the examined frequency $\omega\sqrt{B/2g}=1.5$, the far-field wave amplitude A_3 is numerically predicted to be around $0.2|\eta_3|$. According to Eq. (3.7), the non-dimensional damping coefficient $(B_{33}/\rho A)\sqrt{B/2g}$ is calculated to be approximately 0.006, which means that the influence of wave generation on damping is small. It is therefore appropriate as we did earlier to compare our numerical results with Bearman et al.'s (1984) experimental results for a square section in infinite fluid.

- Possible sensitivity in estimating the drag part

The drag force is a small part of the total hydrodynamic force when η_{3a}/D is small. Let us document this by examining the double-body in infinite fluid. The ratio between the maximum drag force and the maximum added mass force is

$$R_a=0.25\left(\frac{\eta_{3a}}{D}\right)\frac{C_D}{C_A}$$

Using C_D=5.0 and C_A=1.1 gives R_a=1.136(η_{3a}/D), i.e. the ratio is only 0.17 for the largest η_{3a}/D=3/20. The drag force is 90° out of phase with the added mass force and causes a small phase shift in the total hydrodynamic force. The estimated drag force is sensitive to this phase influence.

- Precision in the numerical calculations for small heave amplitude

  The precision in the numerical calculations decreases with decreasing heave amplitude for a given grid size. For instance, for the heave motion with the amplitude of 0.01m and $\omega\sqrt{B/2g}=1.5$, the rectangular cylinder oscillates within less than 5 grid cells near the free surface, and the generated wave elevation oscillates within 2 grid cells. It is desirable to have a larger ratio between the heave amplitude and the grid dimension.

  It is not straightforward to further decrease the grid size. Decreasing the grid size will decrease the timestep size due to the CFL stability criterion. This will increase the number of computational elements and time steps, therefore greatly increase the computational time. Further, the increase of time steps will make numerical diffusivity mentioned in Section 2.4 stronger.

3.3.4 Conclusions

According to the investigations above, we can draw the following conclusions:

- The numerical results of the heave added mass and damping coefficients by the CIP method are in general agreement with both the experimental and linear numerical potential flow results by Vugts (1968).

- The numerical results of the heave damping by the CIP method at high frequencies are due to viscous damping. The results are consistent with Vugts' experimental results except for the smallest examined heave amplitude. The results are not consistent with Bearmean et al.'s experimental drag coefficient for a facing square in infinite fluid. Our numerical results for drag coefficient is not reliable for the smallest examined η_{3a}/D=1/20. This is both due to the small magnitude of the drag force and practical restrictions in reducing the grid size in the numerical computations.

3.4 2D numerical wave tank

3.4.1 Experimental setup

The 2D version of our CIP code will be compared with the experimental results by Aarsnes (1997) for wave forces and moments on a V-shaped test section that was restrained from oscillating. Incident regular waves were considered. The tests were carried out in the extension of the towing tank at the Marine Technology Center in Trondheim. The tank is 80m long and 10.5m wide. The water depth is 10m. The tank is equipped with a hydraulically operated, double-flap wave generator. The cross-section drawing of the wave generator is shown in Figure 3.11. The upper and lower flap motions are in phase with each other. The specified wave conditions and the corresponding motions of the wavemaker are listed in Table 3.6.

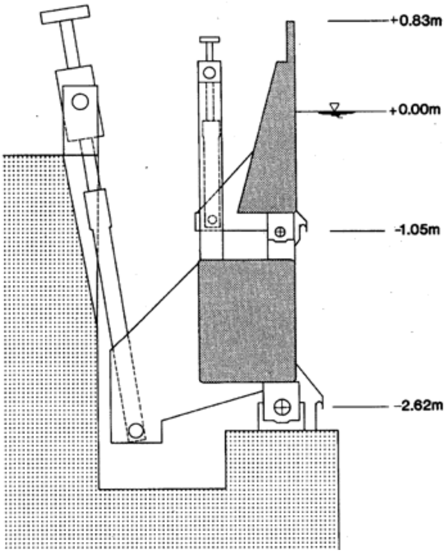

Figure 3.11 Cross-section of the main part of the hydraulic wave generator in the large towing tank at the Marine Technology Center, Trondheim.

The model was mounted underneath the stiff carriage in the extension of the towing tank as shown in Figure 3.12. The draft of the cylinder was altered by lifting the entire model. During the tests, the carriage was kept in the fixed position 30.0m from the wavemaker. The model was mounted in the center of the towing tank and wave absorbers were placed at the end of each dummy section, as shown in Figure 3.13. The intention of the wave absorbers was to reduce the 3D effects which develop at the ends of the model. Without these wave absorbers, a transverse wave system will gradually develop in the towing tank which can significantly influence the measured vertical forces and wave elevation. This effect will be dependent of the actual wave period.

The model with a V-shaped cross-section shown in Figure 3.14 was used in the tests. The total model shown in Figure 3.12 was divided into three parts, one measuring section with a dummy section on each side. The measuring section was connected to the rig using two force transducers. The main data for the model are shown in Table 3.5.

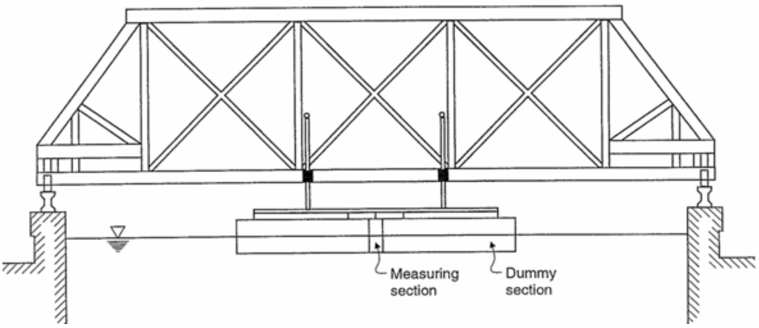

(a) Carriage in the towing tank

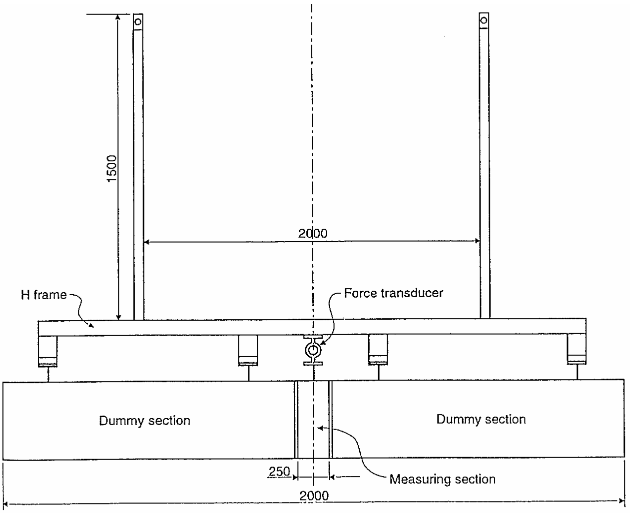

(b) The model

Figure 3.12 Sketch of the model mounted on the carriage in the towing tank.

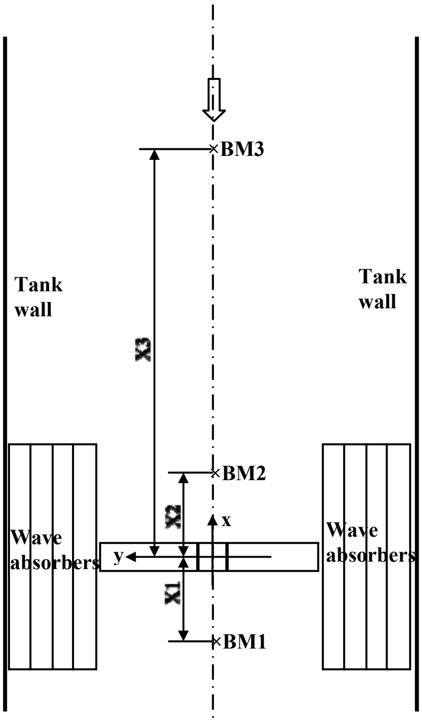

Figure 3.13 Towing tank positions of wave absorbers and wave staffs used in the experimental studies by Aarsnes (1997).

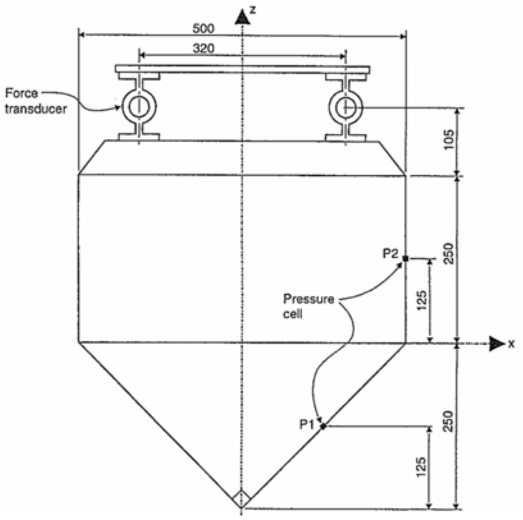

Figure 3.14 Details of the V-shaped test section. Dimensions in mm. The mean water level correspond to z=+150mm in our studies.

Table 3.5 Main dimensions of the V-shaped test section

Breadth	0.500m
Draft	0.400m
Length of measuring section	0.250m
Length of each dummy section	2.000m
Total length	4.250m

3.4.2 Wave conditions

The 2D numerical wave tank (NWT) used in the calculations is 80m long, including a damping zone on the side of the tank opposite to the wavemaker, see Figure 3.15. The experimental wavemaker was included as a part of the numerical wave tank. The control signals for the two flaps for different specified wave heights and periods of regular waves shown in Table 3.6 were estimated based on the wave data in Aarsnes (1997) combined with the wavemaker transfer function (which is stored in MARINTEK's internal computer system for wavemaker BM1 in Towing Tank 1) and a frequency-dependent weight function (which is implemented in MARINTEK’s software "WAVEN"). The water depth is 4m, which satisfies the deep water condition for all test cases. In order to perform simulations in a numerical wave tank with finite computational domain over a long time, a non-reflection boundary condition is required at the downstream boundary. An artificial damping zone is placed at the downstream boundary as shown in Figure 3.15, and an artificial damping force expressed by Eq. (2.32) is added to the body force term in Eq. (2.12).

The whole computational domain used in the numerical simulations has a horizontal length of 80m and a vertical height of 4.83m. The smallest grid length is used near the wavemaker. The minimum horizontal and vertical lengths in the calculations are min(Δx)=0.005m and min(Δy)=0.002m respectively. The total number of the computational cells is 827×253. The timestep size is $\Delta t/T=1/1000$.

Table 3.6 Specified wave conditions and the corresponding wavemaker conditions.

Wave no.	Specified waves		Analysis results from calibration tests		Amplitude of wave maker	
	Wave period T (s)	Wave height H(m)	Wave period T(s)	Wave height H(m)	Upper flap (deg)	Lower flap (deg)
1	1.1	0.03	1.09	0.032	0.663	0
2	1.3	0.03	1.3	0.031	0.588	0.061
3*	1.3	0.06	1.3	0.071	1.176	0.122

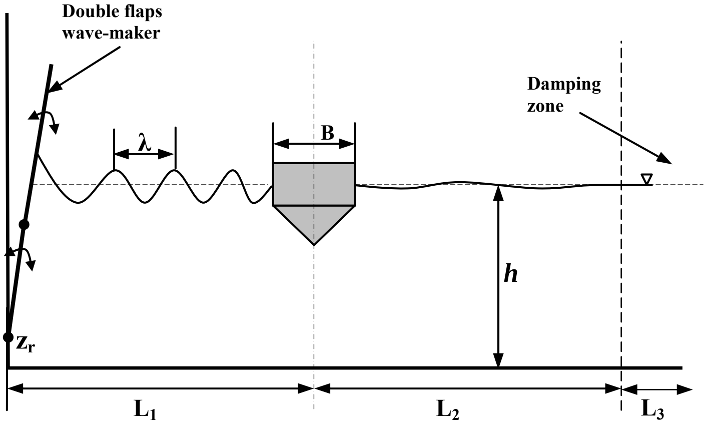

Figure 3.15 Sketch of our numerical wave tank with a double flap wavemaker, damping zone (wave beach) and a fixed body. The lower flap is hinged at a distance z_r above the bottom. The upper and lower flap motions are in phase with each other. L_1 is the distance between the wavemaker and the fixed body, which is chosen larger than 4λ to avoid the local effect at the wavemaker. L_3 is the length of damping zone which must be at least 4λ long to damp the waves.

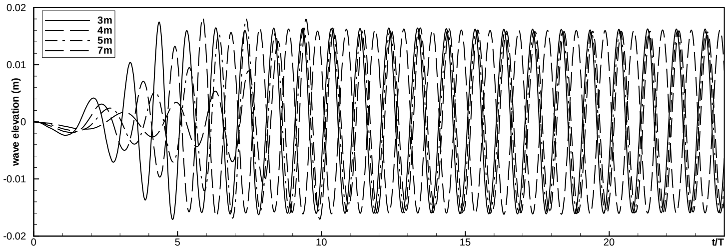

Figure 3.16 Time history of the wave elevations at 3m (solid line), 4m (dashed line), 5m (dash-dot line) and 7m (long-dashed line) from the wave maker. Specified wave: T=1.1s and H=0.03m.

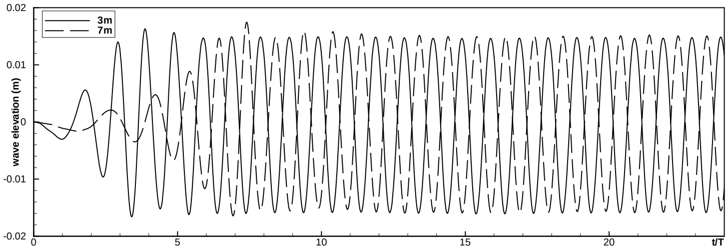

Figure 3.17 Time history of the wave elevations at 3m (solid line) and 7m (long-dashed line) from the wave maker. Specified wave: T=1.3s and H=0.03m.

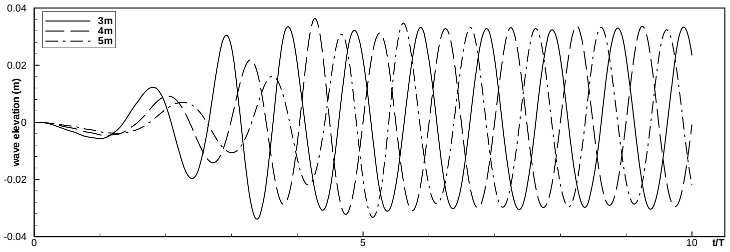

Figure 3.18 Time history of the wave elevations at 3m (solid line), 4m (dashed line) and 5m (blue dash-dot line) from the wavemaker. Specified wave: T=1.3s and H=0.06m.

Figure 3.16 - Figure 3.18 show the time history of the wave elevation at different distances from the wavemaker for different specified incoming wave conditions. We can see the wave elevation at the different distances gets a steady-state behavior after some time. The numerical incident wave height for the No. 1 wave condition in Figure 3.16 is 0.032m. The numerical incident wave height for the No. 2 wave condition in Figure 3.17 is 0.031m. The numerical results for these two wave conditions are in good agreement with the analysis results from the calibration tests. However, the numerical incident wave height for the No. 3 wave condition with superscript * in Table 3.6 is shown to be 0.065m in Figure 3.18 which has a clear difference from the value of 0.071m in the calibration tests and the specified wave height of 0.06m.

3.4.3 Wave forces on 2D section in the free surface zone

When the fixed model is introduced, wave loads acting on the model for the specified wave conditions will be considered. The same computational domain is used in the numerical simulations. The model is fixed at a position 15m from the wavemaker. The smallest grid length is used near the wavemaker and the fixed model. The minimum horizontal and vertical lengths in the calculations are min(Δx)=0.005m and min(Δy)=0.002m, respectively. The total number of the computational cells is 1050×253. The timestep size is $\Delta t/T=1/1000$.

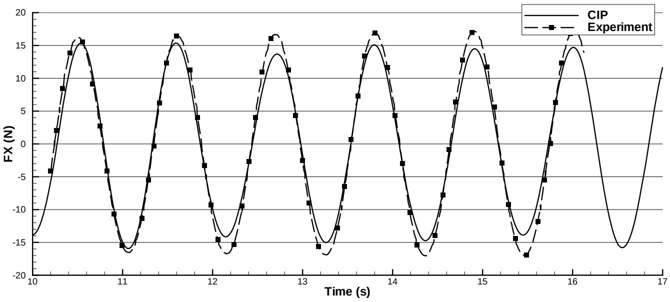

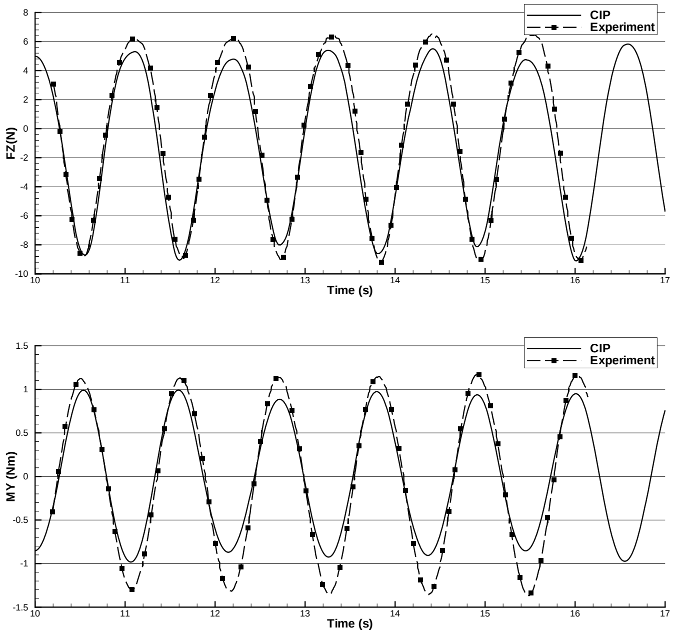

Figure 3.19 Wave forces and moment acting on the V-shaped section for the specified wave condition. T=1.1s, H=0.03m. The draftt is 0.4m. FZ=Vertical force. FX=Horizontal force. MY=Roll moment about the axis through the origin of the coordinate system defined in Figure 3.20.

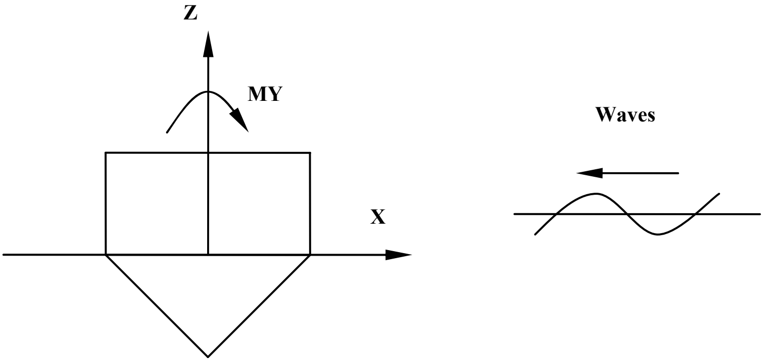

Figure 3.20 Coordinate system. The coordinate system is fixed in the model with origin located at the elevation of the knuckle. Positive z-axis is pointed upwards and the x-axis is horizontal and pointing against the wavemaker. This implies that the waves propagate along the negative x-axis.

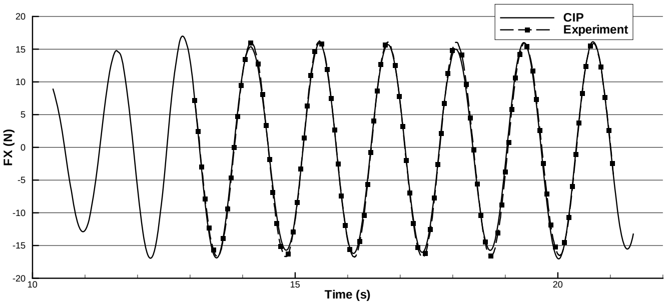

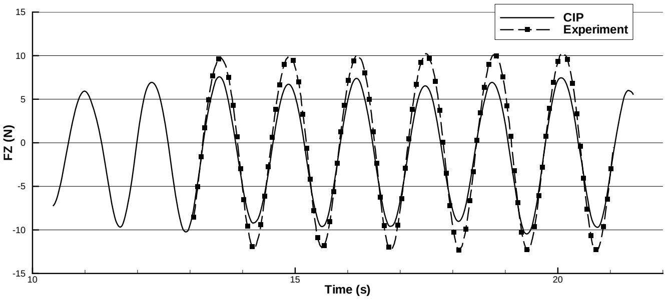

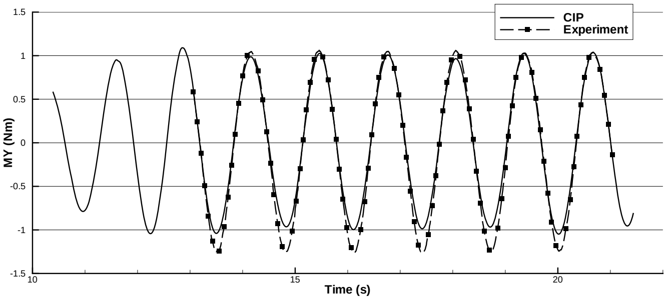

Figure 3.21 Wave forces and moment acting on the V-shaped section for the specified wave condition. T=1.3s, H=0.03m. The draft is 0.4m. FZ=Vertical force. FX=Horizontal force. MY=Roll moment about the axis through the origin of the coordinate system defined in Figure 3.20.

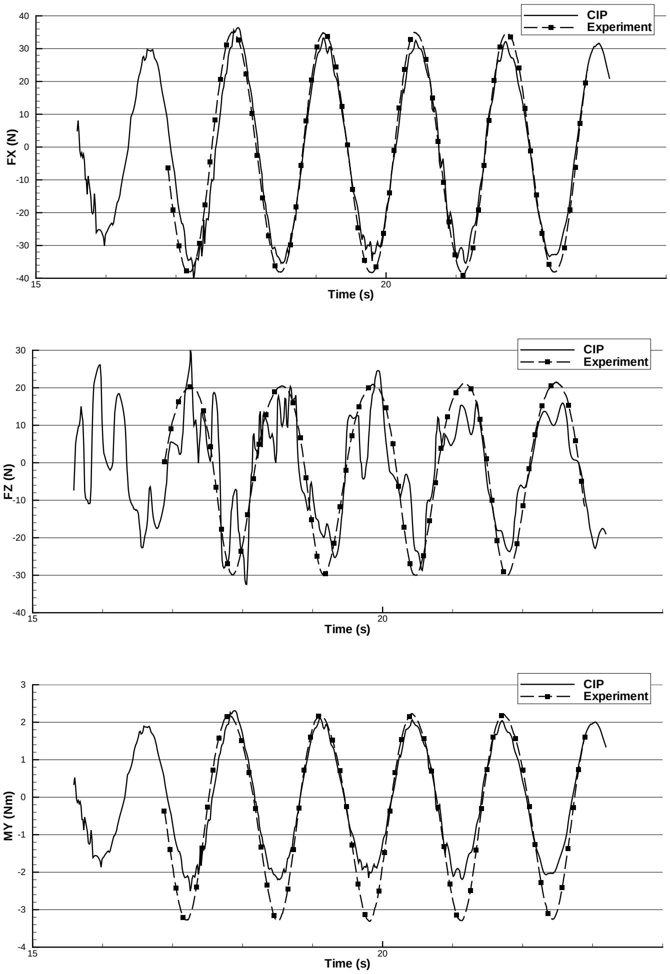

Figure 3.22 Wave forces and moment acting on the V-shaped section for the specified wave conditions. T=1.3s, H=0.06m.The draft is 0.4m. FZ=Vertical force. FX=Horizontal force. MY=Roll moment about the axis through the origin of the coordinate system defined in Figure 3.20.

Figure 3.19 presents comparisons of steady-state wave force and moment when the specified incident wave height and period are 0.03m and 1.1s, respectively. The actual incident wave height was 0.032m both in the experiments and the numerical simulations.

Figure 3.21 presents comparisons of steady-state wave forces and moment when the specified incident wave height and period are 0.03m and 1.3s, respectively. The actual incident wave height was 0.031m both in the experiments and the numerical simulations. Linear effects are dominating in this condition. There is good agreement between numerical and experimental values of the horizontal wave force *Fx*. The differences between the CIP method and the experiments are largest for the vertical force *Fz*. Since the incident wave period 1.3s corresponds to a natural period for transverse sloshing, there is the possibility of experimental errors. Zhao et al. (1988) showed the transverse sloshing resonance had more effect on the vertical than on the horizontal linear wave force. This is consistent with the fact that the horizontal wave forces agree better than the vertical wave force in Figure 3.21.

Figure 3.22 presents comparisons of wave force and moment when the specified incident wave height and period are 0.06m and 1.3s, respectively. The actual incident wave height was 0.071m in the experiments, and 0.065m in the numerical simulations as previously stated. The vertical force has some oscillations, which are related to higher-order components. The first harmonic of the force oscillates with the frequency ω =2π/T, the oscillation frequencies of the second and third harmonic are 2ω and 3 ω, respectively. A Fourier analysis of the total force history shows that the first three harmonics of the hydrodynamic force are dominant. The ratio between the third and the first harmonic force is around 0.27, which is comparable with the results shown in Baarholm (2001) who compared the first and the third harmonic part of the force for Lewis form cylinder with B/D=2 and A/(BD)=0.989 for different heave amplitudes where B is the breadth at the waterline, D is the draft of the cylinder and A is the mean submerged cross-sectional area.

However, when testing the case with the wave period T=1.3s and wave height H=0.12m, we found that the numerical wave tank encounters difficulties in handling the large amplitude motions for long time simulations.

3.4.4 Experimental error sources

Experimental error sources are related to 3D flow effects, incident wave conditions, resonant waves in the tank, and measurement accuracy. Because we did not perform the tests, we cannot quantify experimental errors. However, a qualitative discussion will be given below.

- 3D effects without tank walls

  We assume a free surface of infinite horizontal extent and use the theoretical results for infinite frequency added mass in heave of a rectangular plate by Meyerhoff (1970). If a plate of the same length-to-beam ratio as in the tests is considered and the contribution to the added mass from a section of the same length and position as the measuring section is studied, Meyerhoff's results show that the flow can be considered 2D at the measuring section. However, the frequency matters for the influence of three-dimensionality. Newman & Sclavounos (1981) studied theoretically added mass and damping of a prolate spheroid with the longitudinal axis in the mean free surface and with length-to-beam ratio L/B=8. The effect of three-dimensionality matters for frequencies ω smaller than $\omega\sqrt{L/g}=3$. Using the total length 4.25m of the model shows that three-dimensionalities must be considered when T>1.38s. However, the three-dimensional effects are largest at the ends of the model. This discussion suggests that the flow can be considered two-dimensional at the measuring section for the considered wave period as if the model were in water of infinite horizontal extent.

- Transverse sloshing

The planar fluid motion in the transverse cross-section of the tank has an infinite number of eigenfrequencies. Our concern is if any of these eigenfrequencies are in the vicinity of the frequencies generated by the wave maker and that the corresponding eigenmodes are symmetric about the longitudinal center plane of the tank. These eigenmodes can then be excited due to the three-dimensional nature of flow caused by the test section. This will be present even though we argued earlier in the text that the flow is approximately two-dimensional at the measuring section. Zhao et al. (1988) showed a dominant effect of transverse sloshing on the wave loads of a stationary hemisphere restrained from oscillating. However, no wave absorbers as in Aarsnes' (1997) experiments were used at the tank walls in Zhao et al.'s (1988) experiments. The resonant period of concern in our case is 1.30s, corresponding to four wavelengths across the tank walls. We have no information available documenting how effective the wave absorbers along the tank walls were in Aarsnes' (1997) experiments.

- Longitudinal sloshing (seiching)

It is the lowest mode that is of most concern. We approximate the mode by assuming a longitudinal rectangular tank with 2D flow. Using shallow water theory gives that the natural period of the lowest mode is $T_N = 2L/\sqrt{gh}$, where L is the tank length and h is the water depth. Setting L=80m and h=10m gives T_N=16.15s, i.e. much longer than the considered wave periods. If seiching was excited, it would appear as a beating effect. However, no such effect could be detected in the measurements.

- Incident wave conditions

Transverse instabilities dependent on the wave length and period may develop in the incident waves. Further, there is a scattering effect due to the wave absorbers. The effects of these factors are unknown.

- Measurement accuracy

The force measurements are believed accurate. The wave measurements are affected by meniscus effects due to free surface tension at the wave probe. The resulting measurement accuracy is less than ±0.001m.

3.5 Summary

The CIP-based method is used to solve the linear and weakly nonlinear wave-structure interaction problem in a 2D numerical wave tank (NWT). The wavemaker in the numerical wave tank generates regular and irregular waves.

The numerical results are first compared with the experimental added mass and damping coefficient results of a nearly rectangular section with forced small-amplitude heave motion. The convergence of the CIP-based method is investigated by varying the amplitude of the heave motion, the grid size, the timestep size and the computational domain. From all the studied cases, the added mass coefficient has good agreement with the linear numerical results based on potential flow. However, the damping coefficient has relatively better agreement with the experimental results than with the linear numerical results based on potential flow. Noticeable differences can be observed when comparing the numerical results and the theoretical results. Error sources have been discussed to explain the differences. The results of the BEM agree well with the linear numerical results by Vugts (1968) based on potential flow.

The incoming waves generated by the wavemaker in the numerical wave tank without the fixed body are in good agreement with the specified wave conditions. Wave forces including the horizontal force, vertical force and the moment acting on the 2D section in the free surface zones are compared with the experimental results by Aarsnes (1997). The numerical results of the horizontal force are in good agreement with the experimental results for all three test cases. However, there are noticeable differences between the numerical and the experimental results of the vertical force. These differences may be due to the experimental errors.

Our numerical wave tank encounters difficulties in handling the large amplitude motions for long time simulations. Therefore we will isolate the wave-body interaction problem to water entry and exit sub-problems in the following chapters.

CHAPTER 4

Water entry and exit of a circular cylinder with constant velocity

---

4.1 Introduction

This chapter presents numerical simulations of two-dimensional water-entry and water-exit of a circular cylinder with forced constant velocity by using the CIP-based finite difference method described in Chapter 2. This has relevance for wave loads on a horizontal member of a jacket structure in the splash zone, marine operations where units are lowered from a crane ship through the free surface and large amplitude wave-induced motions and loads on floating structures.

The water exit has been far less studied than the water entry. The water entry phase includes the slamming, i.e. the impact between the body and the free surface. This can be associated with the formation of air pockets and local hydroelastic effects. We include the air flow, but assume a rigid structure. The air and water are assumed incompressible. The compressibility of the air matters when air cushions are generated. The compressibility of the water matters only in a very small initial time and is not believed important for the structural response. Gravity and viscosity do not matter in the initial water entry phase. However, both these two effects must be considered at a later stage of the water entry and during the water exit phase. Viscous effects become important when viscous flow separation occurs. The latter requires the existence of points on the cylinder surface where the shear stress is zero. This takes time to develop after the start up flow around the cylinder. This has been discussed by Schlichting (1979) for the flow around a circular cylinder in an infinite fluid. There occurs Froude number dependent non-viscous flow separation from the cylinder surface during the penetration of the cylinder in our studied water entry cases. An open air cavity is then formed above the cylinder. The non-viscous flow separation is important for the hydrodynamic loads on the cylinder.

Greenhow & Moyo (1997) studied totally submerged horizontal circular cylinders moving with constant vertical motions. The results are compared with the small-time asymptotic solution derived by Tyvand & Miloh (1995a, b), whose results were taken to the third order of the small expansion variable T=Ut/d. Here U is the cylinder speed, t is the real time and d is the initial cylinder centre depth. In Tyvand & Miloh (1995a), the general hydrodynamic conditions are stated for the zeroth-, first- and second-order potentials, but the hydrodynamic condition for the third-order potential is only valid for constant acceleration from rest. The corresponding kinematic conditions are also general, except for the condition corresponding to the third-order potential, which is only valid in the case of constant acceleration from rest. The leading-order gravitational effect appears in the hydrodynamic condition for the second-order potential, and this leading-order gravity-dependent potential satisfies the condition of zero normal derivative at the cylinder contour. Excellent agreement is obtained for small times. Beyond this, only the numerical method gives accurate results until the free surface breaks or the cylinder emerges from the free surface. We compared our numerical results of the free surface deformation of a circular cylinder impulsively started with constant upwards and downwards velocities in initially calm water with the results in Greenhow & Moyo (1997) for several dimensionless times T = Ut/d as defined above. The agreement is fairly good.

It is obvious that if the cylinder submerges very slowly, the free surface will simply close over the cylinder top. However, in our studied cases in this chapter, an open air cavity is happening above the cylinder due to non-viscous flow separation from the cylinder surface during the penetration of the cylinder. Then, the open air cavity will be closed either by that a closed air cushion is formed above the cylinder with the upper cylinder surface remaining dry or that the open air cavity above the cylinder surface disappears with the upper surface becoming wetted. How this open air cavity is closed is a function of the Froude number. The calculations in this chapter indicate that there is a threshold Froude number for a closed air cavity appearing above the cylinder. Then, a relevant question is what the threshold Froude number is.

Moyo (1996) showed the case of a submerging cylinder with radius-based Froude number of 0.46 with no bubbles above the cylinder top, which indicated that the radius-based threshold Froude number should be higher than 0.46. However, he did not show what the threshold Froude number is for his studied cases, where the cylinder starts half-submerged. In this chapter, we studied several Froude numbers, i.e. 0.4627, 0.577, 0.6863, 0.791 and 0.9247 without a clear air cushion. A closed air cushion is clearly created when the Froude number equals 1.1. These imply that the threshold Froude number should be higher than 0.9247 and lower than 1.1 for our studied cases with a cylinder starting from above the free surface. Because there are no experimental results to compare with, we can not tell whether or not the air cushion is in reality created and when the air cushion starts to occur. All these questions need future studies.

In this chapter, we will compare the CIP-based method by existing experimental results for forces during the entry and exit phase. The initial impact and the non-viscous flow separation represent numerically the most difficult phases of the water entry. The final water exit phase before penetration of the cylinder is also numerically challenging.

4.2 Convergence study

A horizontal circular cylinder is forced through an initially calm water surface with a constant vertical velocity V. The submergence of the lowest point on the cylinder relative to the calm water surface is h=Vt. Here t is the time variable with t=0 corresponding to the initial time of impact. The slamming coefficient Cs is defined as

$$Cs \equiv \frac{F_3}{\frac{1}{2}\rho V^2 2R} \tag{4.1}$$

Here:
ρ is the mass density of water;
R is the radius of the circular cylinder;
F_3 is the total vertical hydrodynamic force per unit length of cylinder resulting from the water entry, including the buoyancy force. The viscosity causes a shear force and influences the pressure loads. The effect of viscosity matters for the hydrodynamic force when viscous flow separation occurs. The dominant effect is due to the influence on the pressure loads. However, we cannot separate out what is the influence of viscosity and potential flow effects.

In this section, we will investigate the convergence of the CIP-based method by varying the timestep size and grids size. The No. 2 water entry test by Miao (1989) in Table 4.2 is used as an example case.

4.2.1 Effect of timestep size

The numerical grid used in the calculations is rectangular with horizontal and vertical lengths Δx and Δy (see Figure 4.1) that vary in the computational domain. The smallest values are used at the cylinder. The minimum non-dimensional lengths in the simulations are $\Delta x/R=0.01$ and $\Delta y/R=0.01$. The computational domain has a breadth and height of 400R and 50R, respectively. The total number of cells is 620×450.

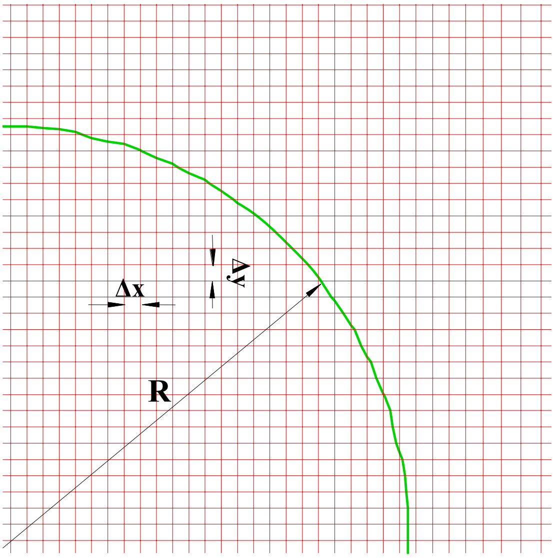

Figure 4.1 Sketch of grid distribution of part of the circular cross-section with radius R and its close vicinity.

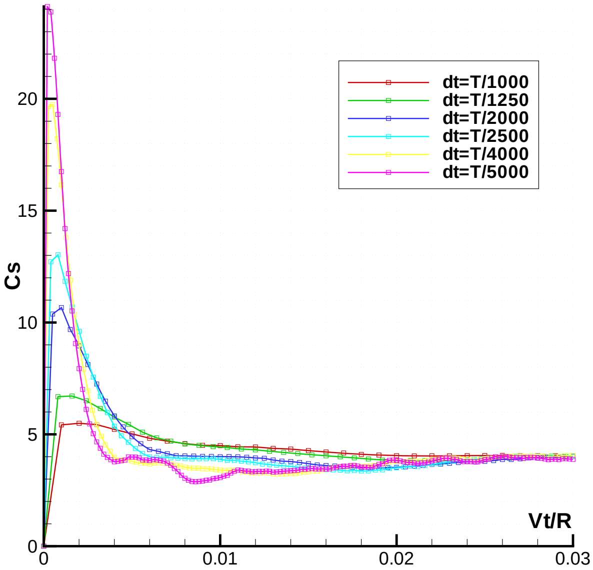

Figure 4.2 Slamming coefficient Cs as a function of non-dimensional submergence Vt/R. Here: dt is the time step size used in the numerical integration; T=R/V where R is cylinder radius and V is water entry velocity. The calculations are for the test condition No. 2 in Miao's (1989) experiments (see Table 4.2).

Figure 4.2 shows how the slamming coefficient Cs as a function of submergence depends on the time step size dt. From this figure, no convergence is apparent at the early stage of the impact. The difficulty in solving this problem can be understood from the numerical results by Zhao & Faltinsen (1993) for water entry of wedges with constant velocity. A non-viscous and incompressible fluid was assumed and a Boundary Element Method (BEM) was applied in their study. The air flow and gravity were neglected. The smaller the deadrise angle β was, the more difficult it was to obtain convergent results. The lowest examined β was 4°. The local deadrise angle is initially zero during the water entry of a circular cylinder. We are better off during the initial impact with using the analytical Wagner's (1932) solution, which shows that the time rate of change of the wetted area 2c in the outer flow domain is proportional to $1/\sqrt{t}$, i.e. the solution is singular at t=0. The outer flow domain excludes the detailed flow in the spray roots and the jets causing spray. The numerical time integration method ought to recognize this singular behavior and an Euler method is inadequate. The Wagner method gives Cs=2π at t=0.

The effect of compressibility and air flow will influence the results. However, it is believed that the origin of our numerical difficulties illustrated in Figure 4.2 is associated with the very rapid initial change of the wetted surface. Although we cannot get convergence of F_3 at the early stage of impact, we can see that all the curves in Figure 4.2 converge after a small submergence $Vt/R \approx 0.02$.

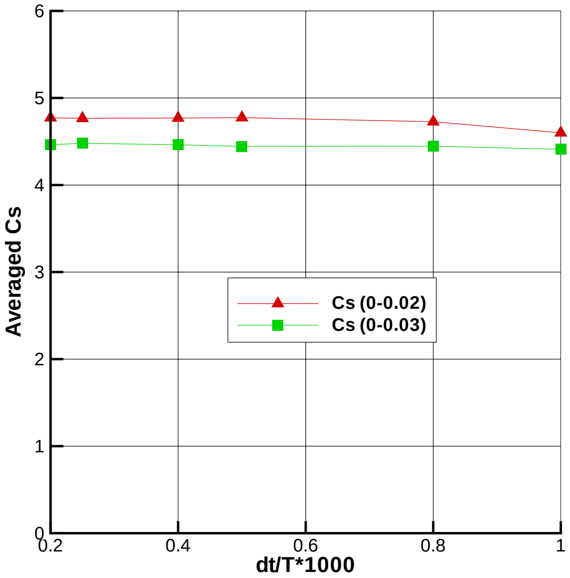

Figure 4.3 Averaged initial slamming coefficient Cs as a function of non-dimensional time stepsize dt/T. Here Cs (0-0.02) denotes the slamming coefficient averaged from Vt/R=0 to 0.02; Cs (0-0.03) is the slamming coefficient averaged from Vt/R=0 to 0.03.

However, for some problems, what is important for the global and local responses of the structure during a small time increment Δt after the impact is the force impulse rather than the instantaneous value of the force. The force impulse is defined as

$$I = \int_0^{\Delta t} F_3(t)dt \qquad (4.2)$$

We compared therefore time-averaged Cs-values (related to the force impulse I) during the small submergences (related to small time increment Δt) Vt/R=0.02 and Vt/R=0.03 as a function of the time step size. From Figure 4.3, convergence for the averaged Cs can be obtained when a small time step size is used.

The initial impact phase results by using the time-averaged Cs are in reasonable agreement with the empirical formulas by Miao (1989) and Campbell & Weynberg (1980). We will now investigate the numerical results for a broader range of Vt/R.

4.2.2 *Effect of grid size*

Figure 4.4 shows the slamming coefficient as a function of Vt/R for different grid size as shown in Table 4.1. Because all the results are in favorable agreement with the experiments, we can in different cases choose different grid size to decrease the computing time.

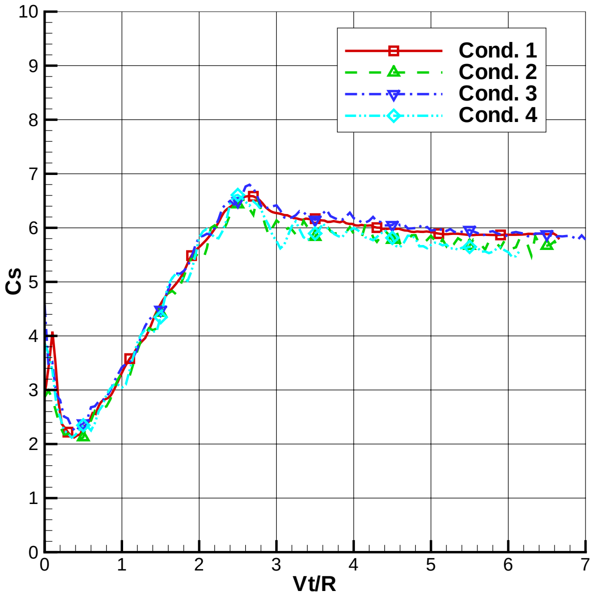

Figure 4.4 Convergence study for different grid sizes for No. 2 water entry test in Miao (1989).

Table 4.1 Computational conditions

Condition No.	Grid number (NX×NY)	Minimum grid size		Timestep size $\Delta t/T$
		min($\Delta x/R$)	min($\Delta y/R$)	
1	290×371	0.04	0.04	1/2000
2	340×371	0.02	0.04	1/2000
3	290×521	0.04	0.02	1/2000
4	340×494	0.02	0.02	1/2000

4.3 Water entry with constant velocity

4.3.1 Description of the experiment

Our CIP-based method will be compared with the water entry tests by Miao (1989) in the No. 2 tank at the Marine Technology Centre in Trondheim. The basin is 28m long, 2.5m wide and has a water depth of 1.0m.

A test cylinder with diameter D=0.125m and length L=0.25m was used in measuring the impact forces. In order to achieve a two-dimensional flow condition, the model was equipped with two rectangular stiffened end plates with height H=0.4m and width B=0.3m.The test cylinder was made from a standard PVC pipe. The pipe thickness is 3.7mm. The end plates were made of plexiglass for photographic purpose during the impact phase of the experiment.

A hydraulic system drove the model vertically downwards into water at speeds ranging from 0 to about 2.66m/s. The stroke was regulated by an electronically operated valve in combination with the measurements of the position of the test cylinder by means of a potentiometer. The water entry velocity was determined from an average slope computed from the position data. Other parameters for the water entry tests are shown in Table 4.2.

The numerical grid is rectangular with horizontal and vertical lengths Δx and Δy that vary in the computational domain. The smallest values are used at the cylinder. The minimum non-dimensional lengths in the simulations are $\Delta x/R=0.02$ and $\Delta y/R=0.02$. The computational domain has a breadth and height of 400R and 50R, respectively. The total number of cells is 500×435.

Table 4.2 Parameters for the water entry tests by Miao (1989)

Test No.	No.1	No.2	No.3	No.4	No.5
V(m/s)	0.5124	0.639	0.760	0.876	1.024
F_n	0.4627	0.577	0.6863	0.791	0.9247

4.3.2 Possible parameters influencing Cs

The non-dimensional impact force defined by Eq. (4.1) can be expressed as

$$Cs = f(\frac{Vt}{D}, F_n, Re_, ...)$$

where $F_n = V/\sqrt{gD}$ is the Froude number, Re=VD/ν is the Reynolds number and $\nu = \mu/\rho$ is the kinematic viscosity of water. Other possible parameters influencing Cs are the roughness number k/D, the Weber, Euler and Cauchy numbers. Here k is the mean height of the roughness on the cylinder surface. We assume a rigid structure so that non-dimensional parameters characterizing the elastic properties of the structure do not matter.

- **k/D and Re**

The viscous parameters k/D and Re will matter for the force magnitude after viscous flow separation has occurred. This will in practice for water entry mean that the whole cylinder surface is wetted and the cylinder has penetrated many cylinder radii.

- **Euler number Eu**

The Euler number $Eu = p_a/(0.5\rho V^2)$ where p_a is the atmospheric pressure must be considered if closed air cavities are formed.

- **Weber and Cauchy numbers**

The Weber and Cauchy numbers account for the surface tension and the compressibility of the water, respectively. The importance of surface tension requires a free surface with high curvature. It matters, for instance, in describing the details of either spray or small bubbles. However, the detailed spray behavior has negligible influence on the hydrodynamic loads on the structure. We do not consider the effect of surface tension in our calculations. The compressibility of the water matters at a very small initial time, when the speed of sound in water is smaller or the order of $\sqrt{VR/t}$. The latter is the theoretical velocity of half of the intersection point of the cylinder and undisturbed free surface position, when the effects of air cushion, air flow and free surface deformation are neglected. Let us exemplify what this time scale means by setting the speed of sound, i.e. 1400ms^{-1}, equal to $\sqrt{VR/t}$ and use $V=0.5124\ m \cdot s^{-1}$ together with R=0.0625m. This gives the time $1.634 \cdot 10^{-8}$ s or $Vt/R = 1.34 \cdot 10^{-7}$. This corresponds to a significantly smaller time than the time steps used in the calculations presented in Figure 4.2. The consequence is that we have not properly modeled the effect of the compressibility in the water. However, the compressibility of the water matters in a too small time scale to have practical importance for the global behavior of the structure and maximum structure stresses. This means that the error in adequately modelling the compressibility of water is unimportant for our application.

- **Fn and Re**

Our further discussion will focus on the influence of Fn and Re. A smooth cylinder surface is assumed. The Froude number dependence is both due to the free surface wave generation and the buoyancy force.

In order to check the influence of Reynolds number on Cs, both a low and a high Reynolds number in the subcritical flow regime are used in the calculations and the comparisons are shown in Figure 4.5, Figure 4.6 and Figure 4.9. The Reynolds number was obtained by varying fictitiously the kinematic viscosity of water. The results show a small difference between the high and low Reynolds numbers. This is an expected result for this Reynolds number variation in the subcritical flow regime. The vorticity in the fluid was calculated in order to assess the influence of the viscous forces. Because the major vorticity was concentrated in the boundary layer of the cylinder, i.e. no flow separation, there is expected a small effect of viscosity on the pressure. Further, the frictional force gave a very small contribution to the total force.

We can explain qualitatively the behavior of Cs as a function of Vt/R by expressing the total vertical force as in Faltinsen (1990)

$$F_3 = d(VA_{33}(t))/dt + \rho g A(t) = V dA_{33}(t)/dt + \rho g A(t)$$

Here A_{33} is the 2D infinite-frequency heave added mass and A(t) is the cylinder area below the mean free surface. $dA_{33}(t)/dt$ is largest at t=0 and decreases with increasing Vt/R while A(t) increases with time. The combination of $VdA_{33}(t)/dt$ and $\rho gA(t)$ causes a minimum Cs as we see occurs at about Vt/R=0.5 in the examined cases. This approach does not account for the fact that the water separates from the cylinder and causes an open air cavity above the cylinder. It follows by continuity of fluid mass that the water displaced by the cylinder and the air cavity causes an increased water elevation. This free surface wave generation affects the vertical force. A large part of the force at the final stage when the cylinder surface is totally wetted is due to the buoyancy.

If the cylinder is totally submerged, the contribution of the buoyancy to the slamming coefficient is

$$C_{Sb} = \frac{\rho g \pi D^2/4}{\frac{1}{2}\rho V^2 D} = \frac{\pi}{2}\frac{1}{F_n^2} \tag{4.3}$$

This value is presented in Figure 4.5-Figure 4.9 from the time when the cylinder is totally submerged. There is a maximum in Cs a small time before the cylinder is totally submerged.

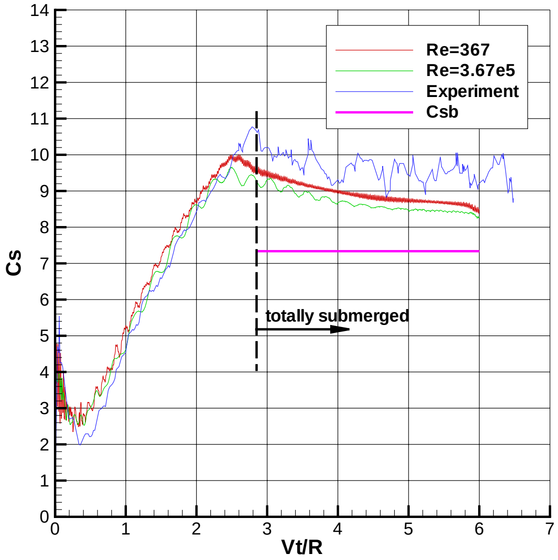

Figure 4.5 Slamming coefficient Cs as a function of Vt/R for the water entry test No.1. V=0.5124 m/s. Fn=0.4627.

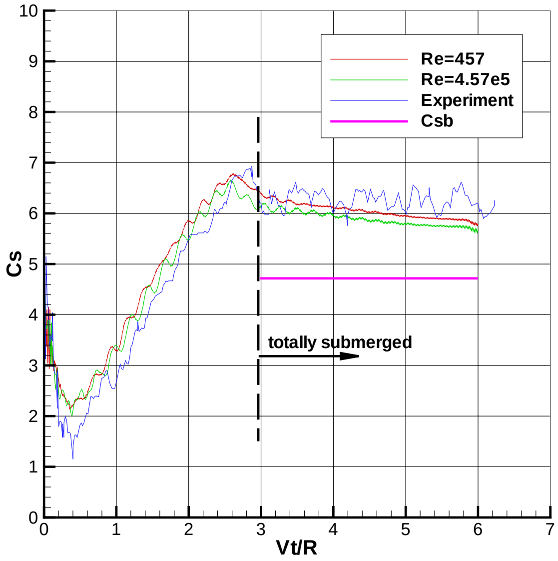

Figure 4.6 Slamming coefficient Cs as a function of Vt/R for the water entry test No. 2. V=0.639 m/s. Fn=0.577.

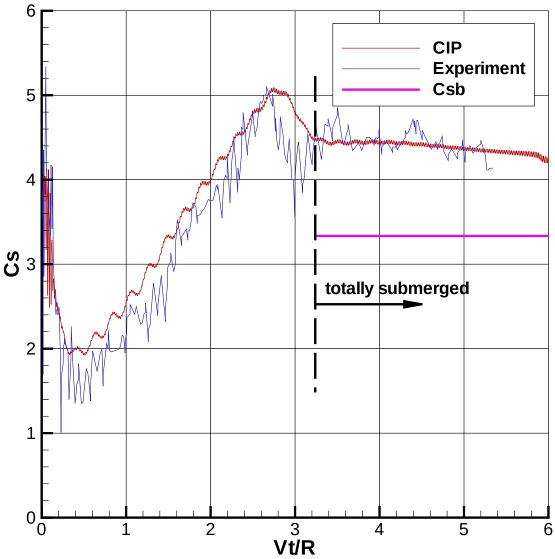

Figure 4.7 Slamming coefficient Cs as a function of Vt/R for the water entry test No. 3. V=0.760 m/s. Fn=0.6863.

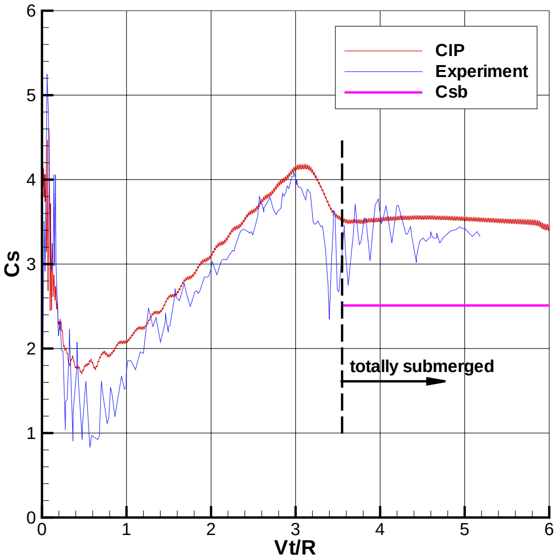

Figure 4.8 Slamming coefficient Cs as a function of Vt/R for the water entry test No. 4. V=0.876 m/s. Fn=0.791.

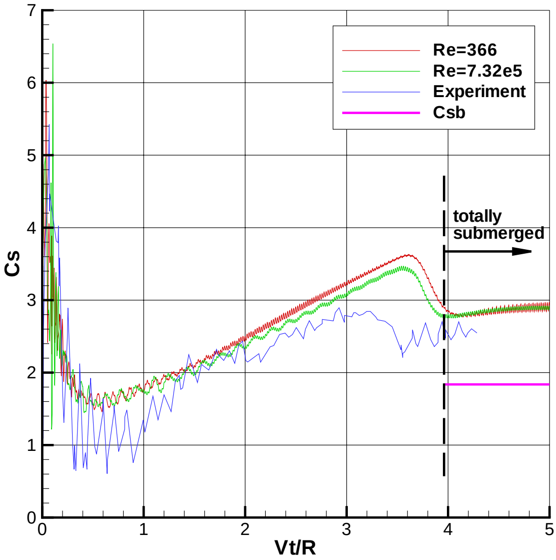

Figure 4.9 Slamming coefficient Cs as a function of Vt/R for the water entry test No. 5. V=1.024 m/s. Fn=0.9247.

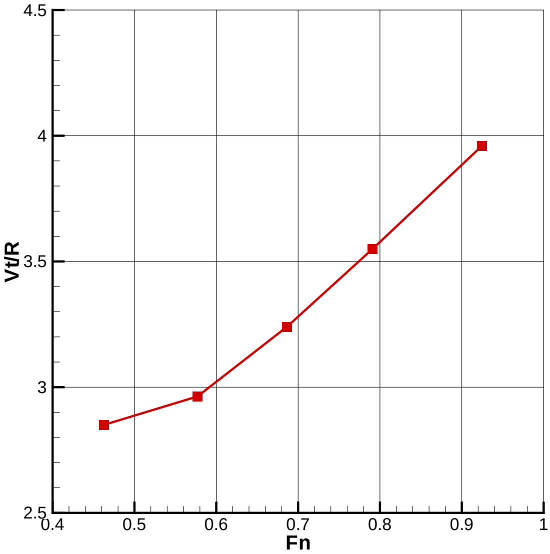

Figure 4.10 The non-dimensional time Vt/R when the circular cylinder is totally submerged as a function of Froude number Fn for water entry with constant velocity.

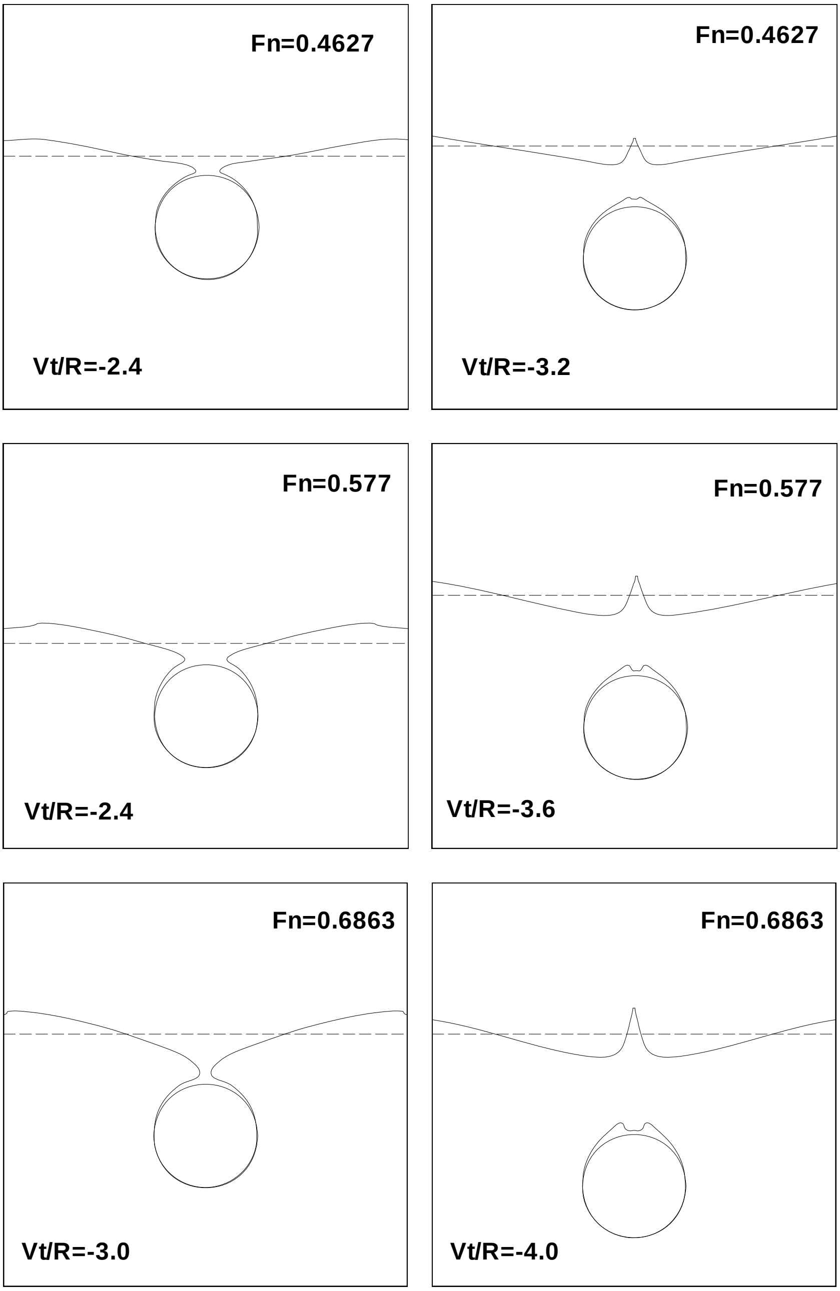
Fn=0.4627
Vt/R=-2.4
Fn=0.4627
Vt/R=-3.2
Fn=0.577
Vt/R=-2.4
Fn=0.577
Vt/R=-3.6
Fn=0.6863
Vt/R=-3.0
Fn=0.6863
Vt/R=-4.0

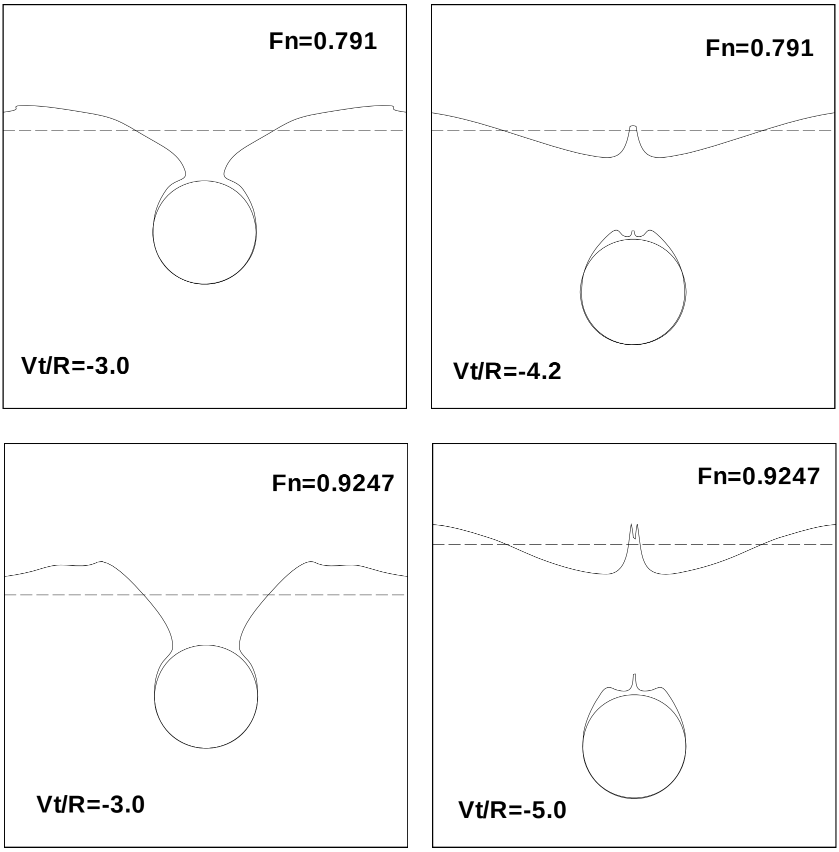

Figure 4.11Free surface deformations for different Froude numbers before and after the impact of the two free surfaces of the open air cavity.

As one can see from Figure 4.5 to Figure 4.9, the non-dimensional time Vt/R for the cylinder to be totally submerged for the five Froude numbers studied above increases with the Froude number and is illustrated in Figure 4.10. Figure 4.11 shows the free surface deformations for the five different Froude numbers before and after the impact of the two free surfaces of the open air cavity. We can see the two free surfaces on both sides of the open air cavity move almost along the cylinder surface. After the impact, a very thin layer appears above the cylinder top. This thin layer may be due to either the generation of the closed air cushion or the numerical diffusion on the free surface. Because the numerical method does not predict a sharp interface between the water and air, and because of the small thickness of the apparent air cushion above the cylinder and numerical diffusion, we cannot be sure that a closed air cushion occurs. If the thin layer is the closed air cushion, then the threshold Froude number will change to be lower than 0.4627 instead of 1.1 as stated in the introduction. When the Froude number goes to infinity, we expect an infinitely long air cavity above the cylinder.

This is similar to the water entry of a wedge at infinite Froude number studied by Zhao et al. (1996). When time goes to infinity, the problem is equivalent to steady cavity flow past a wedge at zero cavitation number.

4.3.3 Experimental error sources

From Figure 4.5 to Figure 4.9, some differences exist between the numerical results and the experimental data at the final stage of impact. The fact that we predict correctly the buoyancy force for the totally submerged phase is no surprise. So, in order to judge the accuracy of the predictions, we must deduct the buoyancy force. This increases the errors in the numerical predictions relative to the experiments. However, the experiments have errors as well.

Experimental error sources could be

- Buoyancy force due to the stiffened end plates. This contribution to the slamming coefficient is approximately 0.03 at Vt/R=0 and is about 0.1 after Vt/R=4.2.

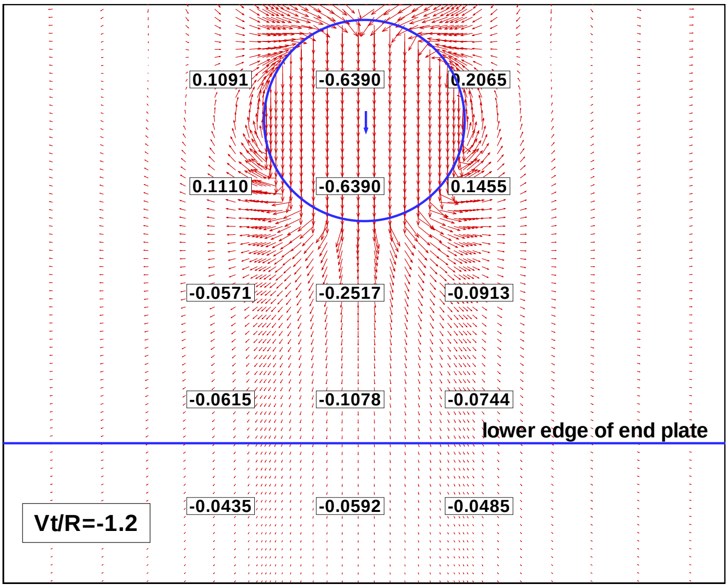

Figure 4.12 Velocity field in the vicinity of the circular cylinder and the vertical velocity around the end plate edge for the water entry test No. 2. The water entry velocity of the circular cylinder is 0.639m/s. Vt/R=-1.2 means that the distance between the lowest point of the cylinder and the mean free surface is 1.2 times the radius of the cylinder. Fn=0.577.

- 3D flow effects in the experiments. Although the two end plates were used on the model cylinder, it is impossible to completely get rid of 3D effects and to achieve 2D flow. This was numerically documented in the present case by evaluating the 2D flow velocity around the cylinder at the position of the plate edges in Figure 4.12. Since this was not negligible, we anticipate some 3D flow effects. We cannot quantify this. However, we expect that the 2D flow assumption represent a good approximation.

- Cross flow with flow separation at the edges of the end plates as a consequence of 3D flow.

- Frictional force on the end plates. The vertical frictional force on the end plates can be estimated by $F = \frac{1}{2}\rho C_F V^2 S$, where S is the area of both sides of the two end plates, i.e. S=4HB where H is the height of the end plates and B is the width of the end plates. The International Towing Tank Conference (ITTC) 1957 model-ship correction line expresses the friction coefficient C_F for a smooth hull surface as $C_F = 0.075/(\log_{10}Re-2)^2$, where $Re=VH/\nu$ is the Reynolds number. The contribution of the frictional force to the slamming coefficient is $C_{SF} = F/(\frac{1}{2}\rho V^2 DL)$, which is approximately equal to 0.01. One should note that the estimation by assuming totally wetted plate sides is an approximation. Further, the effects of stiffeners and the fact that the velocity along the inside of the plates is spatially varying due to the presence of the cylinder are ignored. However, our objective is to estimate qualitatively the contribution of frictional force to the slamming coefficient. We find that this contribution is about 0.01, i.e. it is negligible.

- Possible necklace vortices (see Lugt, 1983) at the intersection lines between the plates and the cylinder. We cannot estimate this effect.

- Natural frequencies of the test rig, including possible hydroelastic effects. Chezhian (2003) documented clear hydroelastic effects in his experimental drop tests of a horizontal 3D structure with circular cross-sections. The oscillatory nature of the experimental slamming coefficient suggests either hydroelastic effects, eigenfrequency oscillations of the test rig, or air cavity oscillations. Miao (1989) said without giving detailed explanations that the 140Hz oscillations seen in the experiments can be associated with the measuring system. However, oscillations with smaller frequencies occur also in the force measurements, in particular when the cylinder surface is totally wetted. We made a rough estimate of the possibility of oscillations of air bubbles. This was done by guessing the possible dimensions of the air bubbles and estimating the natural frequency of the air bubble oscillations (see Faltinsen, 2005). We found that this could not explain the oscillating behavior of Cs.

4.3.4 Numerical prediction for Fn=1.1

The previous results of water entry of a circular cylinder were for the five Froude numbers 0.4627, 0.577, 0.6863, 0.791 and 0.9247. Slamming coefficient Cs was examined as a function of Vt/R from 0 to 6. The most important parameters are Vt/R and Fn. There is negligible Froude number dependence at the initial stage of the water impact. However, the Froude number matters at a later stage. We will in the following study Fn=1.1 to further investigate the Froude number dependence of Cs and the flow as a function of Vt/R. There are no experimental results to compare with in this case.

Figure 4.13 presents the results of Cs as a function of Vt/R. The vorticity in the fluid was calculated in order to assess the influence of the viscous forces. Because the major vorticity was concentrated in the boundary layer of the cylinder, there is a small effect of viscosity on the vertical force.

Figure 4.14 shows the free surface deformation during the water entry of the cylinder. As one can see, after the cylinder reaches the free surface, the water rises and two jets are thrown up on both sides of the cylinder and move away from the cylinder, leaving the upper part of the cylinder dry even when h/R>2, where h (=Vt) is the submergence of the lowest point on the cylinder relative to the mean free surface. The free surfaces on the two sides of the air cavity eventually become unstable and the cavity formed behind the cylinder collapses. The free surfaces of the open air cavity above the cylinder impact first against each other above the cylinder surface. The impact throws up another jet. The closure of the air cavity for Fn=1.1 occurs when Vt/R≈5.2. The flow will be affected by the Euler number after the closure of the air cavity. Because the compressibility of the air is neglected, we cannot properly describe the behavior of the air cavity. Otherwise, one would need to account for adiabatic compression of the air bubble (see Best, 1993).

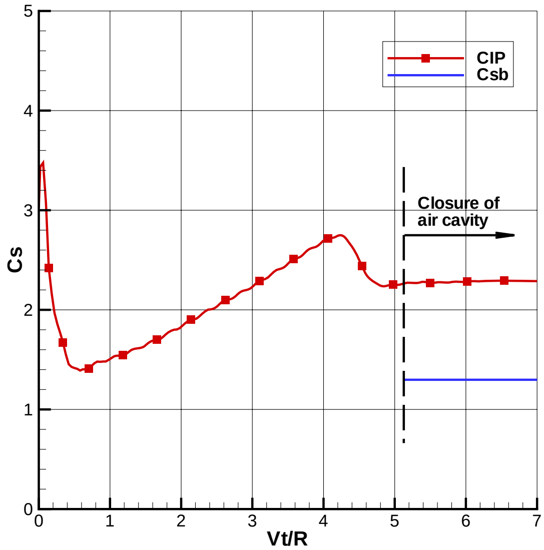

Figure 4.13 The slamming coefficient Cs as a function of non-dimensional time Vt/R. Fn=1.1. Eu=135. Re=$1.52 \cdot 10^5$.

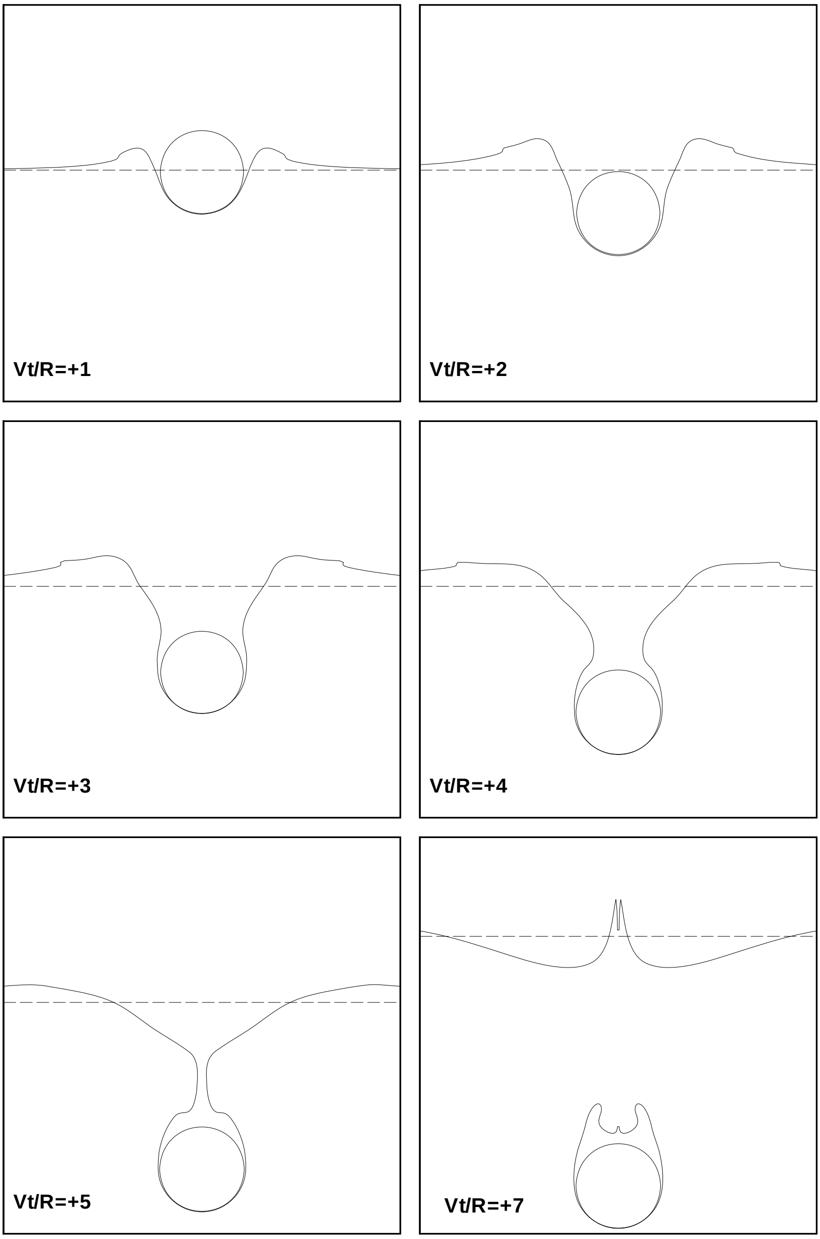

Figure 4.14 The free surface deformation during the water entry of a circular cylinder with constant velocity. A closed air cavity is formed above the cylinder at Vt/R≈5.2. The free surface denotes the density function $\varphi_1 = 0.5$. *Fn=1.1. Eu=135. Re=*$1.52 \cdot 10^5$.

4.4 Water exit with constant velocity

4.4.1 Comparisons between CIP and experiments

Similarly as for the water entry studies, the grid used in the water exit calculations is also rectangular. The smallest horizontal and vertical lengths are used at the cylinder. The minimum values are $\Delta x/R=0.04$ and $\Delta y/R=0.04$. Other parameters for the water exit tests are shown in Table 4.3.

Table 4.3 Parameters for the water exit tests by Miao (1989)

Test No.	No.1	No.2
V(m/s)	0.5124	0.7644
F_n	0.4627	0.6903

A minor correction was made to the experimental data to make it possible to compare with the numerical results. The buoyancy force due to the stiffened end plates has been subtracted from the experimental data. Its contribution to the vertical force matters until Vt/R=4.2, where t=0 corresponds to the time when the top of the cylinder reaches the mean free surface.

Figure 4.15 and Figure 4.16 present comparisons of the exit coefficient Ce between the CIP calculations and the experiments by Miao (1989). Here Ce is defined in the same way as the slamming coefficient Cs; see Eq. (4.1). The overall agreement is good. The cylinder was initially at rest at Vt/R=-5.5, and was accelerated harmonically by using a function of $\sin \omega t$ to a constant velocity V at Vt/R=-5 in the numerical simulations. Here, Vt/R=-5.5 means that the distance between the top of the cylinder and the mean free surface is 5.5 times the radius of the cylinder.

We note large oscillations in the experimental force. This is believed to be experimental errors associated with unwanted vibrations of the test rig causing added mass and structural inertia forces on the test cylinder. The vibrations are probably connected with the automatic control of the hydraulic system used to force the test cylinder out of the water. The control system was based on the position measurements. However, small deviations in the position can cause large accelerations. Let us illustrate this by an example based on the data in Figure 4.16. There is from Vt/R=-4.5 to -3.2 a large amplitude oscillation of Ce which we denote as Ce_0. We use a harmonic approximation, i.e. $Ce_0 \sim Ca\sin(\omega t+\alpha)$, where ω is estimated as 60(rad/s). We neglect the structural mass and approximate the oscillatory force amplitude as $\rho\pi R^2\omega^2 A$, where A is the amplitude of the oscillations of the test rig. Using the definition of Ce and estimating the amplitude Ca of the oscillatory part Ce_0 of Ce as 2.4 gives A/R=0.03, i.e. A is a small value as we anticipated. The velocity amplitude ωA associated with this oscillatory behavior is 0.11V. We note that the oscillatory forces are largest at the start-up. Similar behavior was also seen during the water entry tests at the start- up of the cylinder above the mean free surface. This confirms our suspicion that the oscillatory forces are due to the transient effects of the hydraulic system.

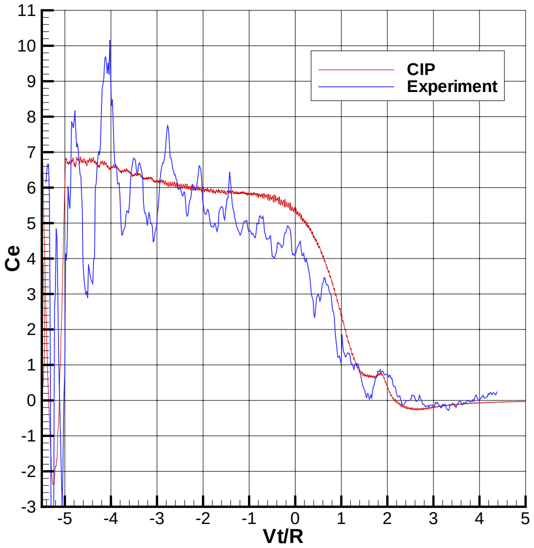

Figure 4.15 Exit coefficient Ce as a function of Vt/R for the water exit test No. 1. V=0.5124m/s. Fn=0.4627.

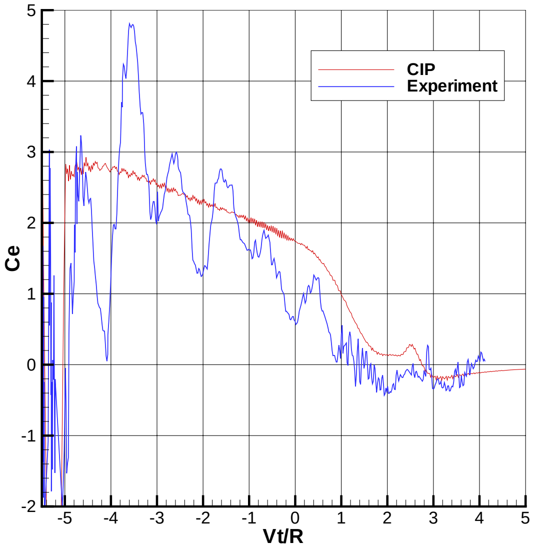

Figure 4.16 Exit coefficient Ce as a function of Vt/R for the water exit test No. 2. V=0.7644m/s. Fn=0.6903.

4.4.2 A simplified model

In order to further explain physically the results, we will introduce a simplified model that accounts for buoyancy, viscous drag and a potential flow force expressing the time rate of change of heave added mass. This model does not account for the deformation of the free surface which is important when the cylinder is close to the free surface. We believe that a rigid wall condition is a proper free surface condition for the exit problem when the cylinder is not too close to the free surface.

It follows by the time rate of change of the kinetic fluid energy, the "rigid-wall" free surface condition and potential flow theory that there is a vertical hydrodynamic force

$$F = \frac{1}{2} V \frac{dA_{33}(t)}{dt} + A_{33} \frac{dV}{dt}$$

acting on the cylinder. We notice that the structure of this expression differs from the force expression $d(A_{33}V)/dt$ used in the simplified water entry calculations. The reason is the difference in the free surface conditions. For constant exit velocity,

$$F = \frac{1}{2} V^2 \frac{dA_{33}}{dz} \tag{4.4}$$

Here $z = 0$ is the mean free surface and the vertical z-coordinate is positive downwards. F is positive upwards. Because this formula for water exit is not well known, in the following we will give a detailed derivation by using conservation of kinetic energy. An alternative derivation based on Lagrange's equations may be found in Moyo (1996).

Assume zero gravity and incompressible fluid in irrotational motion, the rate of change of kinetic energy in a fluid domain Ω can be expressed by Eq. (3.19) and (3.20) in Faltinsen (1990) as

$$\frac{dE_k(t)}{dt} = -\rho \iint_S \left(\frac{\partial \varphi}{\partial t} \frac{\partial \varphi}{\partial n} - \left(\frac{p - p_0}{\rho} + \frac{\partial \varphi}{\partial t} \right) U_n \right) ds \tag{4.5}$$

where S is the boundary surface to Ω and $\partial / \partial n$ is the derivative along the normal unit vector $\vec{n}$ to S. Positive direction of $\vec{n}$ is into the fluid domain. U_n denotes the normal velocity of S and p_0 is the atmospheric pressure.

Further, because $\nabla^2 \varphi = 0$,

$$E_k(t) = \frac{\rho}{2} \iiint_\Omega \nabla \varphi \cdot \nabla \varphi d\tau = \frac{\rho}{2} \iiint_\Omega \nabla \cdot (\varphi \nabla \varphi) d\tau \tag{4.6}$$

Applying the divergence theorem to Eq. (4.6) gives

$$E_k(t) = -\frac{\rho}{2}\iint_S \varphi \frac{\partial \varphi}{\partial n} ds \tag{4.7}$$

Let the bounding surface S consist of the wetted body surface S_B, the "rigid-wall" S_W, two vertical control surfaces S_∞ and $S_{-\infty}$ at $y = \infty$ and $y = -\infty$ respectively and finally a surface S_0 far down in the fluid between S_∞ and $S_{-\infty}$ (see Figure 4.17), i.e. $S = S_B + S_W + S_\infty + S_{-\infty} + S_0$, we write

$U_n = \partial\varphi / \partial n = Vn_3$ on S_B
$U_n = \partial\varphi / \partial n = 0$ on S_W , $S_{\pm\infty}$ and S_0

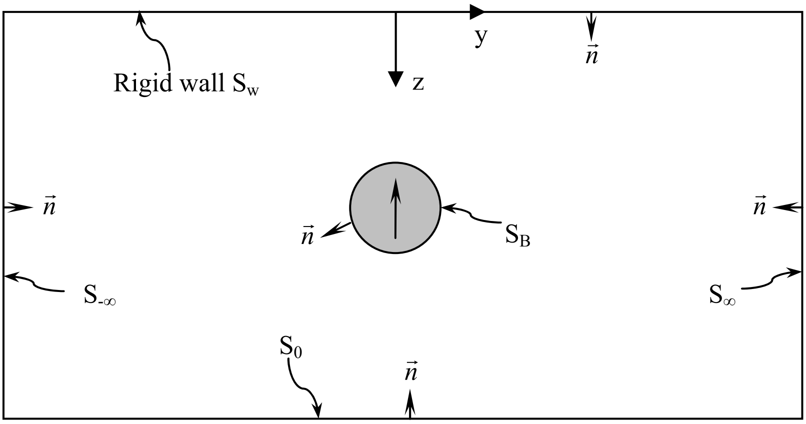

Figure 4.17 The fluid domain and its control surface

Because the contributions from S_W , $S_{\pm\infty}$ and S_0 disappear and we can write $\varphi = \varphi_3 V$, Eq. (4.7) can be simplified to by using the definition of the added mass

$$E_k(t) = -\frac{\rho}{2}V^2 \iint_{S_B} \varphi_3 \frac{\partial \varphi_3}{\partial n} ds \tag{4.8}$$

We can rewrite Eq. (4.8) in terms of heave added mass A_{33} . The linearized pressure $p = -\rho\,\partial\varphi/\partial t$ can be written as $p = -\rho\,\varphi_3 dV/dt$ where φ_3 satisfies $\partial\varphi_3 / \partial n = n_3$ on the body surface. Here n_3 is the z-component of the normal vector. The resulting vertical force is

$$F_3(t) = -\iint_{S_B} p n_3 ds = \rho \frac{dV}{dt} \iint_{S_B} \varphi_3 n_3 ds$$

which by definition is equal to $-A_{33}\dfrac{dV}{dt}$. Then we have $A_{33} = -\rho \iint_{S_B} \varphi_3 n_3 ds$. It follows that

$$E_k(t) = \frac{1}{2} A_{33} V^2 \tag{4.9}$$

On the right hand side of Eq.(4.5), we have no contribution from S_W, $S_{\pm\infty}$ and S_0, so

$$\frac{dE_k(t)}{dt} = \iint_{S_B} (p - p_0) V n_3 ds = -V F_3 \tag{4.10}$$

Substituting Eq. (4.9) into the left hand side of Eq. (4.10), we have

$$\frac{d}{dt}\left(\frac{1}{2} A_{33} V^2\right) = -V F_3 \tag{4.11}$$

or

$$F_3 = -\frac{1}{2}\frac{dA_{33}}{dt} V - A_{33}\frac{dV}{dt} \tag{4.12}$$

Because $\dfrac{dA_{33}}{dt} = \dfrac{dA_{33}}{dz}\dfrac{dz}{dt} = \dfrac{dA_{33}}{dz} V$ and V is constant, we finally get

$$F_3 = -\frac{1}{2}\frac{dA_{33}}{dz} V^2 \tag{4.13}$$

This is consistent with the Eq. (4.4) by noting that F_3 is positive downwards.

The 2D heave added mass A_{33} for the circular cylinder satisfying the rigid-wall condition is estimated by generalizing the asymptotic formula for large z/R by Sun (2004), i.e.

$$\frac{A_{33}(z)}{\rho \pi R^2} = \frac{\alpha^4 - 1}{\alpha^4 - 2\alpha^2} \tag{4.14}$$

where $\alpha = 2p/R$ and z=p means the z-coordinate of the cylinder axis. This agrees well even for small (p/R-1) with the asymptotic expression for small (p/R-1) by Walton (1986). Since Walton's formula is not good for large (p/R-1), we have used Eq. (4.14) in our calculations even though it is not exact for very small (p/R-1). Since our objective is only to show the trend in the force for small (p/R-1), this is sufficient. The free surface will in reality not be a wall when the cylinder is close to the free surface.

The viscous drag coefficient was estimated by curve-fitting the experimental data by Sarpkaya (1966) as

$$C_D = p_1 t^{*5} + p_2 t^{*4} + p_3 t^{*3} + p_4 t^{*2} + p_5 t^{*} + p_6 \tag{4.15}$$

Here $t^* = Vt'/R - 0.351 \geq 0$ and the time $t' = 0$ is the start of the flow. The non-dimensional p_i-coefficients are given as follows:

$$p_1 = 2.4805 \cdot 10^{-7}$$
$$p_2 = -3.647 \cdot 10^{-5}$$
$$p_3 = 1.9058 \cdot 10^{-3}$$
$$p_4 = -4.4173 \cdot 10^{-2}$$
$$p_5 = 4.3146 \cdot 10^{-1}$$
$$p_6 = 7.3386 \cdot 10^{-2}$$

When $0 \leq Vt'/R \leq 0.351$, C_D equals to zero. These results are for subcritical flow, i.e. the boundary layer flow is laminar. This is appropriate for the model tests. However, the boundary layer flow upstream of the separation points on the cylinder surface may be turbulent in full scale conditions. This has an important effect on C_D. Further, Sarpkaya's results are for an infinite fluid and nearly constant velocity V. Both the presence of the free surface and the time variation of V will influence C_D.

Then, the total vertical hydrodynamic force including the contributions due to the buoyancy force is expressed as follows:

$$F_3 = \rho g \pi R^2 - 1/2 \rho C_D D V^2 + 0.5 V^2 dA_{33}/dz \tag{4.16}$$

Figure 4.18 shows the calculations with this simple formula. It demonstrates that the buoyancy and viscous forces dominate when $Vt/R \leq -1$. When $-1 < Vt/R \leq 0$, there is a dominant effect due to the time rate of change of the kinetic fluid energy.

Figure 4.19 shows the comparisons between the simplified formula and the CIP calculations. It demonstrates a good agreement when $Vt/R \leq -1$. This means implicitly that the CIP calculations are consistent with Sarpkaya's experiments for the time variation of the viscous drag coefficient. A major effect of the viscous force is due to viscous flow separation. This can implicitly be seen from Figure 4.20 which shows numerically predicted vorticity in the fluid and demonstrates that the vorticity is not concentrated in the boundary layer along the cylinder as it was for our water entry studies. The agreement between the simplified formula and the CIP calculations is not good for $-1 < \mathrm{Vt/R} \le 0$. However, since a significant deformation of the free surface occurs then, this should not be expected.

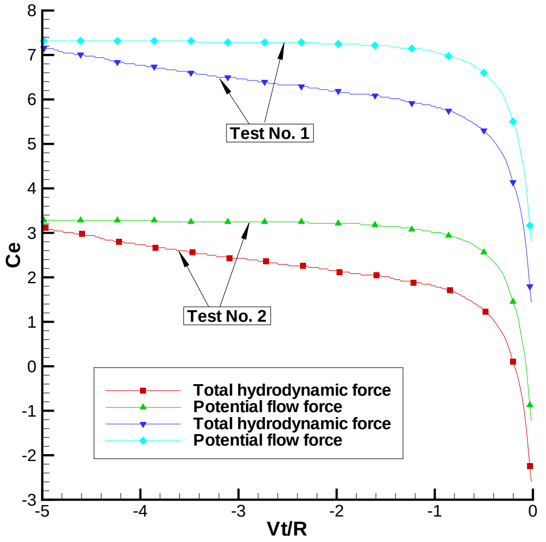

Figure 4.18 Simplified calculations of the exit coefficient $Ce=F_3/(0.5\rho V^2 2R)$ by Eq. (4.16) with and without the effect of viscous drag force as a function of Vt/R for the two water exit tests.

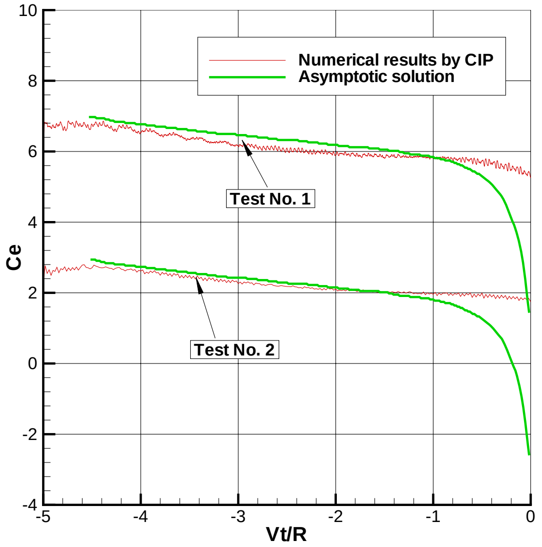

Figure 4.19 Comparisons between the simplified formula Eq. (4.16) and the CIP calculations for the two water exit tests. $Ce=F_3/(0.5\rho V^2 2R)$.

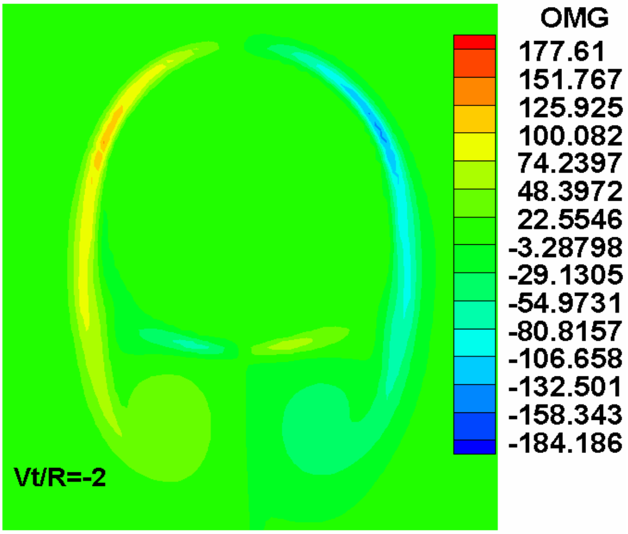

Figure 4.20 Numerically predicted vorticity field for the water exit test No. 1. Fn=0.4627. OMG means the vorticity with dimension s^{-1}.

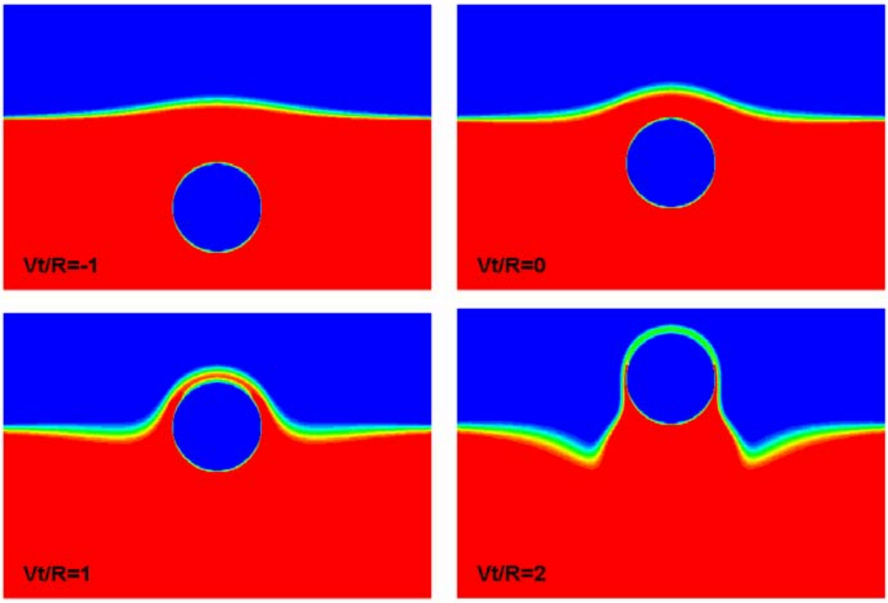

Figure 4.21 Visualization of free surface deformation for the water exit test No. 2. The pictures present the density function φ_1 *which is theoretically one for water and zero for the body and the air. Red=1. Blue=0. Fn=0.6903.*

The time dependent free surface elevation is illustrated in Figure 4.21, by showing the density function φ_1 which is theoretically one for water and zero for the body and the air. Red and blue colors mean one and zero, respectively. The presence of other colors is caused by numerical errors and illustrates that the interfaces between the water and the air and the body are not sharp in the numerical simulations.

However, returning now to Figure 4.15 and Figure 4.16, we then see both in the experiments and in the CIP calculations that a significant change in the vertical force occurs when the cylinder is close to the free surface. We can, based on the calculations with the simplified formula, say that this rapid change in force is in a qualitative way associated with the large rate of change of the kinetic fluid energy. We believe that at the final stage of the water exit when the total force becomes close to zero, ventilation in the fluid below the cylinder and above the mean free surface occurs. This will be made evident later in the text.

The numerical results for Vt/R<-1 should be compared with the experimental data obtained after filtering out the oscillatory force behavior. We explained the oscillations earlier as an experimental error due to the hydraulic system. The averaged experimental data are in fair agreement with the numerical simulations. However, the oscillations of the cylinder will influence the time development of the drag coefficient through changes in the time history of the separation points. This will require further studies.

4.4.3 Numerical prediction for Fn=1.0

The 2D water exit of a circular cylinder with the Froude number of 0.4627 and 0.6903 is studied in detail by the CIP method in the previous sections and good agreement is documented with the experimental results by Miao (1989) for forced constant vertical velocity. We will present another case with forced constant vertical velocity, with a Froude number of 1.0.

Figure 4.22 presents the computed exit coefficient *Ce* as a function of *Vt/R* for the three Froude numbers. Figure 4.23 shows the comparisons between the simplified formula and the CIP calculations. The time-dependent-free-surface elevation is illustrated in Figure 4.24, by showing the density function $\varphi_1=0.5$. The water above the cylinder is lifted by the cylinder and a thin layer of water is formed subsequently on the top of the cylinder. The numerically predicted pressure showed that cavitation does not occur. However, the predicted total pressure in the water can be lower than the atmospheric pressure below the cylinder at the final stage of the water exit. This suggests that ventilation occurs.

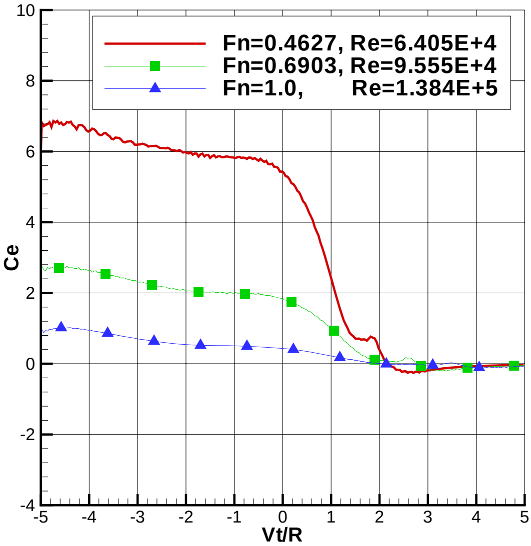

Figure 4.22 The exit coefficient Ce as a function of the non-dimensional time Vt/R.

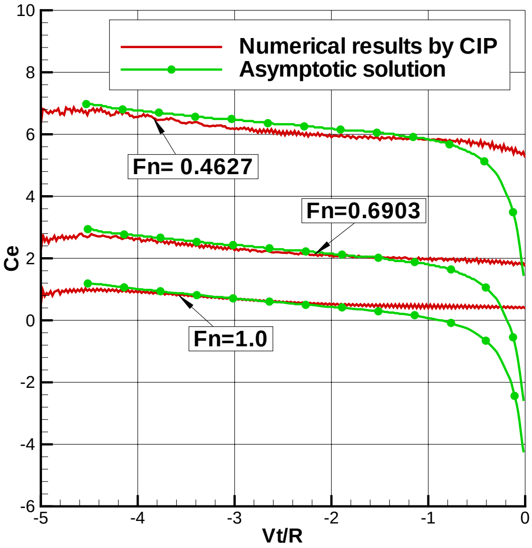

Figure 4.23 Comparisons between the simplified formula (Eq. (4.16) and the CIP calculations for water exit tests. $Ce=F_3/(0.5\rho V^2 2R)$.

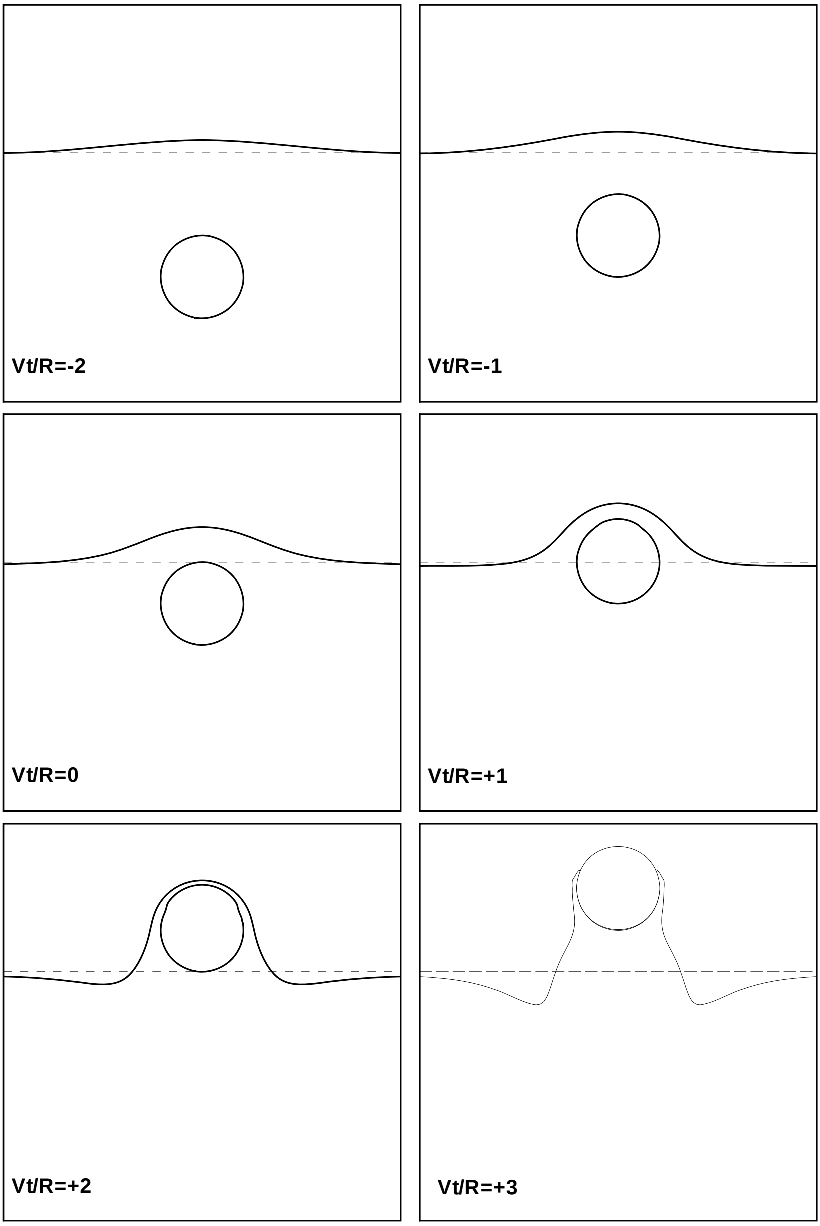

Figure 4.24 Visualization of free surface deformation for water exit simulation with Fn=1.0. The free surface denotes the density function $\varphi_1 = 0.5$.

4.5 Summary

The slamming coefficient Cs as a function of Vt/R has no apparent convergence at the early stage of the impact of a circular cylinder. The reason is believed to be that the numerical time integration method (Euler method) used in the code does not recognize the singular behavior at t=0. However, the initial impact phase results by using the time-averaged Cs during a small submergence are in reasonable agreement with the empirical formulas by Miao (1989) and Campbell & Weynberg (1980).

For water entry, possible parameters influencing Cs, i.e. the Froude number Fn, the Reynolds number Re, the roughness number k/D, the Weber, Euler and Cauchy numbers are investigated. Non-viscous flow separation and wave generation are important factors during water entry after an initial penetration phase. Viscous effects have a minor influence on the water entry force. Experimental error sources are discussed.

For water exit, a simplified model is introduced to explain physically the results of exit coefficient. The predicted vorticity associated with viscous flow separation, the time rate of change of kinetic fluid energy and the free surface deformation give a reasonable explanation of the phenomena observed during water exit.

The CIP calculations give a good overall agreement with the experiments by Miao (1989) for water entry and water exit with constant velocity.

CHAPTER 5

Water entry and exit of a circular cylinder with vertical free motion

---

This chapter presents the fully nonlinear free-surface deformation of an initially calm water caused by water-entry and exit of a horizontal circular cylinder with free vertical motion by using a CIP-based finite difference method.

5.1 Water entry with vertical free motion

Now we consider the free surface profiles caused by a circular cylinder dropped into initially calm water. A half-buoyant and a neutrally buoyant circular cylinder with a radius of 5.5cm are used in the calculations. The depth of water is 0.30m. The cylinder was dropped from a height of 0.5m between the lowest point of the cylinder and the mean free surface. Numerical results are compared with the experiments conducted by Greenhow & Lin (1983).

5.1.1 Half-buoyant cylinder

Figure 5.1 shows the free surface deformation during water entry of a half-buoyant circular cylinder. As one can see, after the cylinder reaches the free surface, two jets are thrown up on both sides of the cylinder and move away from the cylinder, leaving the upper part of the cylinder dry even when $h/R>2$, where h is the submergence of the lowest point on the cylinder relative to the mean free surface. The non-viscous flow separation from the cylinder is by no means trivial to numerically predict. The author is aware of other CFD methods having difficulties with this. Obviously the prediction of the non-viscous flow separation can be influenced by the grid size. Relatively small grids were used at the areas of flow separation in our numerical simulations.

Figure 5.2 shows the depth of penetration of the cylinder. Fairly good agreements can be obtained between the numerical results and experimental data for a half-buoyant cylinder.

t=0.305s

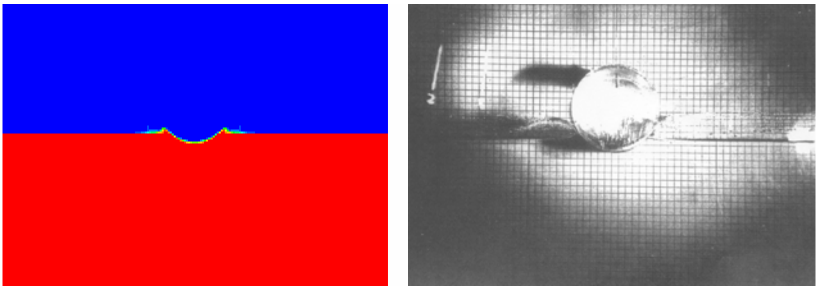

t=0.330s

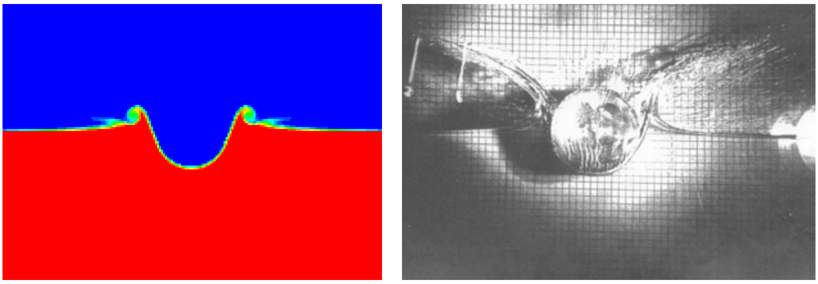

t=0.385s

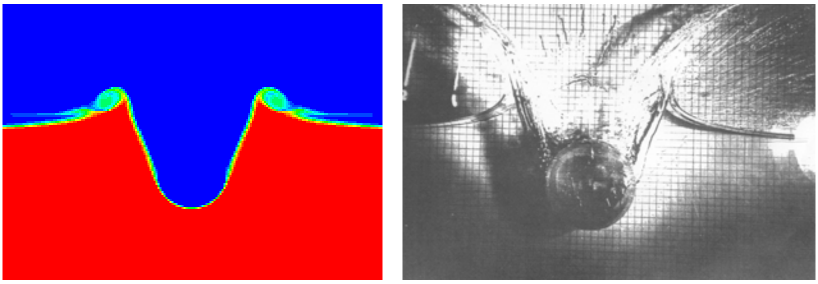

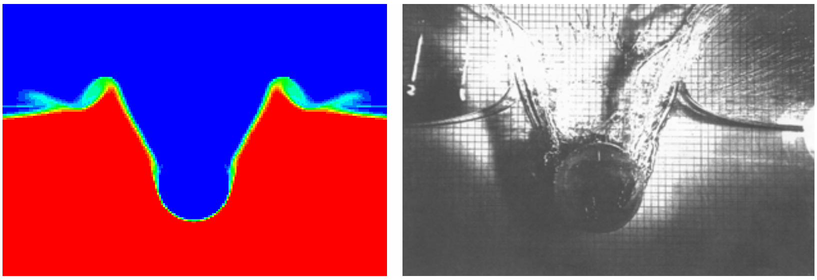

t=0.420s

Figure 5.1 Free surface deformation during water entry of a half-buoyant circular cylinder with a radius of 5.5cm. CIP simulations (left) and experiments by Greenhow & Lin (right). The pictures present the density function φ_1 which is theoretically one for water and zero for the body and the air. Red=1. Blue=0.

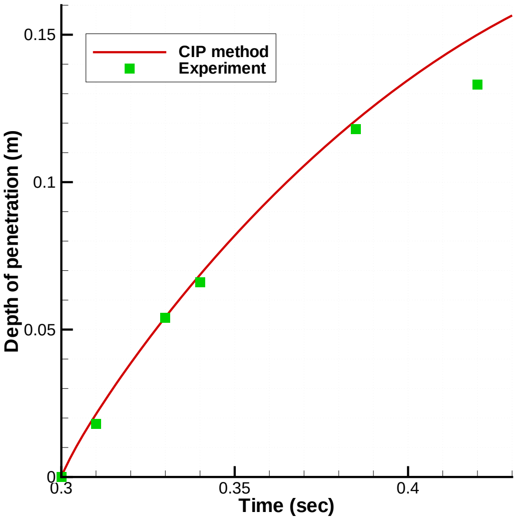

Figure 5.2 Depth of penetration during water entry of a half-buoyant circular cylinder with a radius of 5.5cm.

5.1.2 Neutrally buoyant cylinder

Figure 5.3 shows the free surface deformation during water entry of a neutrally buoyant cylinder at several time instants. Similar to the half buoyant cylinder, after the cylinder reaches the free surface, two jets are thrown up on both sides of the cylinder and move away from the cylinder, leaving the upper part of the cylinder dry even when h/R>2. The free surfaces on the two sides of the air cavity eventually become unstable and the cavity formed behind the cylinder collapses. The free surfaces of the open air cavity above the cylinder impact first against each other at the cylinder surface. The impact throws up another jet. Some air bubbles can be seen along the cylinder moving upwards to the free surface.

At t=0.50s, the cylinder reaches the bottom of the tank and bounces up. Because the bottom of the tank is not modeled in this computation, we used the same treatment as Xing-Kaeding et al. (2004), i.e. the velocity of the cylinder is simply reversed at this time instant to simulate a loss-free re-bounce.

Figure 5.4 shows the time history of the penetration depth of the neutrally buoyant cylinder. At t=0.34s, the experimental data is clearly larger than the numerical result. However, Greenhow & Lin (1983) put a question mark over this point.

t=0.315s

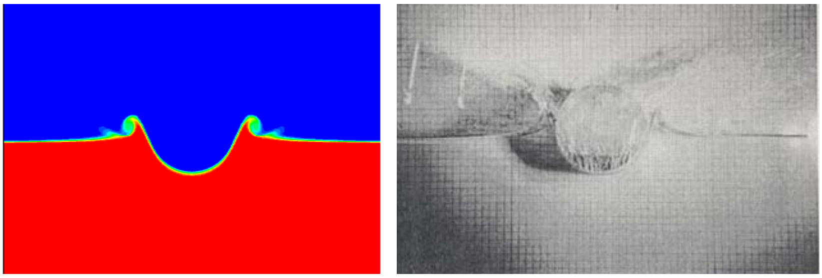

t=0.410s

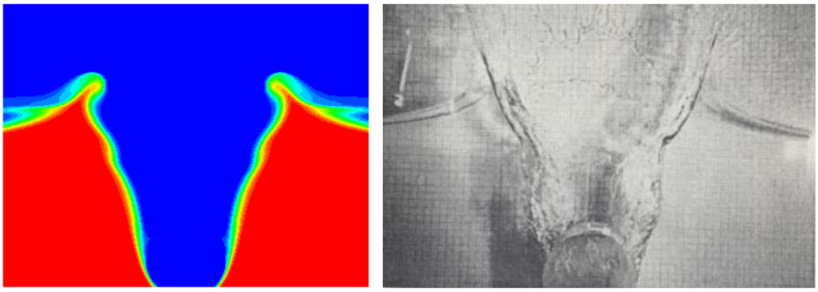

t=0.50s

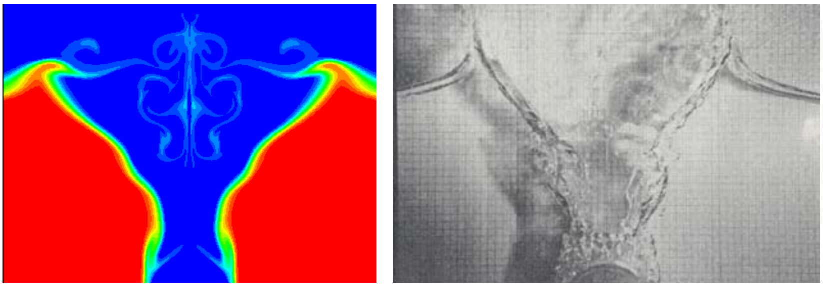

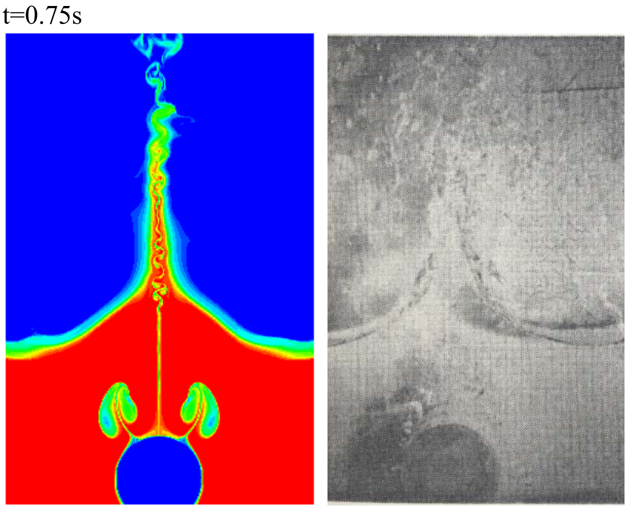

Figure 5.3 Free surface deformation during water entry of a neutrally buoyant circular cylinder with a radius of 5.5cm. CIP simulations (left) and experiments by Greenhow & Lin (right). The pictures present the density function φ_1 *which is theoretically one for water and zero for the body and the air. Red=1. Blue=0.*

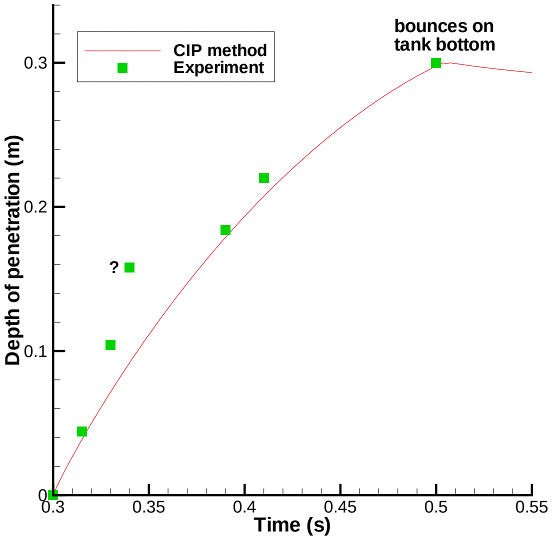

Figure 5.4 Depth of penetration during water entry of a neutrally buoyant circular cylinder with a radius of 5.5cm.

Figure 5.3 and Figure 5.4 show in general satisfactory agreement between the numerical results and experimental data for the neutrally buoyant circular cylinder.

5.2 Water exit with constant force

We study now a neutrally buoyant circular cylinder which rests on the tank bottom and is lifted by applying a constant force equal to the cylinder weight. Numerical results are compared with the experiments conducted by Greenhow & Lin (1983).

t=0.072s

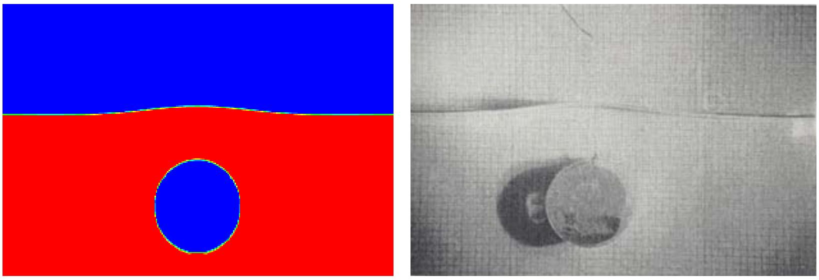

t=0.165s

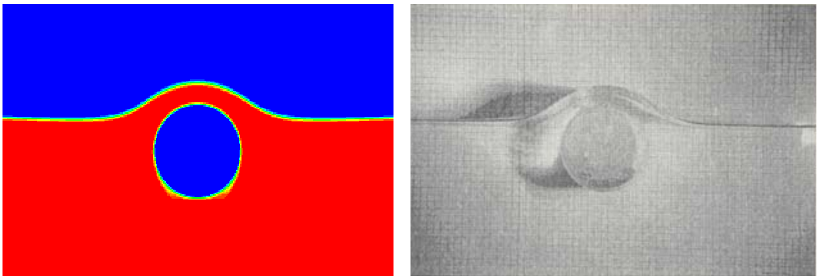

t=0.220s

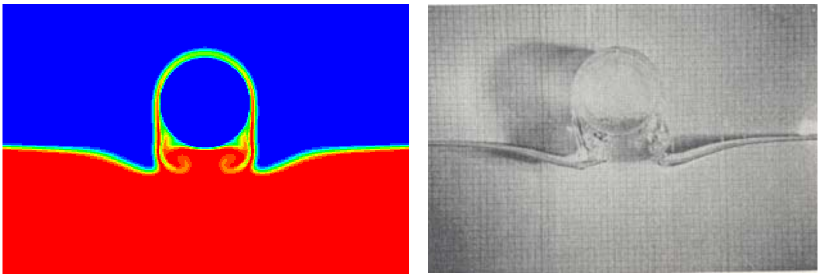

t=0.248s

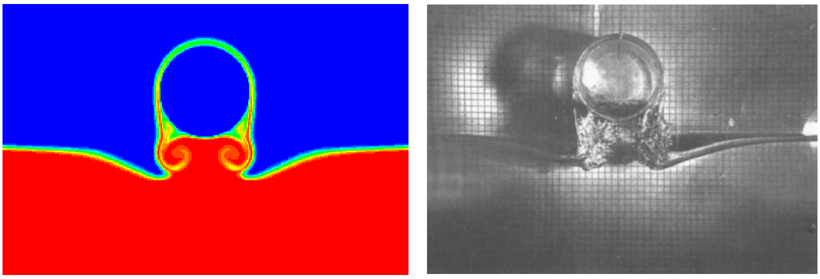

t=0.280s

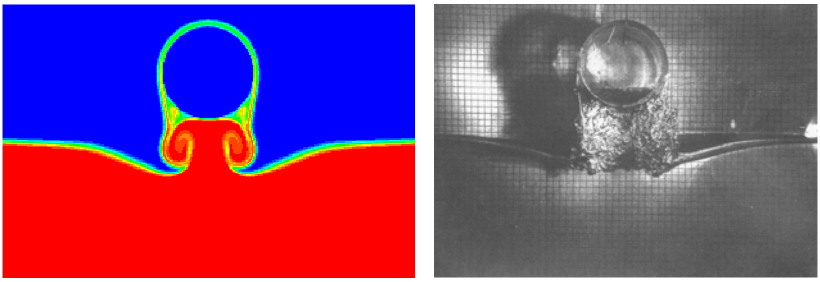

Figure 5.5 Free surface deformation during water exit of a neutrally buoyant circular cylinder with a radius of 5.5cm. CIP simulations (left) and experiments by Greenhow & Lin (right). The pictures present the density function φ_1 *which is theoretically one for water and zero for the body and the air. Red=1. Blue=0.*

Figure 5.5 shows the free surface deformation at several time instants. The numerical simulations predicted the dominating phenomena during the water-exit of a cylinder: the water above the cylinder is lifted by the cylinder and thin layers of water are formed subsequently on the top of the cylinder. When the cylinder further rises up, the thin water layer is drawn down along the cylinder and causes the breaking of the free surface. The fact that viscous flow separation has occurred (see Figure 4.20) lowers the pressure below the cylinder. The numerically predicted pressure distribution at time instant t=0.248s is illustrated in Figure 5.6. Because the total pressure in the water is clearly higher than the vapor pressure (e.g. 2336.9Pa at 20°C), cavitation does not occur. However, the predicted pressure in the water is lower than the atmospheric pressure in the vicinity of the free surface below the cylinder. This suggests that ventilation happens and is confirmed by the experimental results showing a mixture of the water and the air below the cylinder. The numerical simulations in Figure 5.6 show two large eddies below the cylinder with a yellow-like color. This color implies a mixture between the water and the air. However, the fine details of how ventilation occurs require future studies. Moyo & Greenhow (2000) associate the break-down of the free surface and resultant ventilation with the fundamental fluid-mixing mechanism connected with the Rayleigh-Taylor instability. This occurs when a light fluid (e.g. air) is accelerated into a heavy fluid (e.g. water).

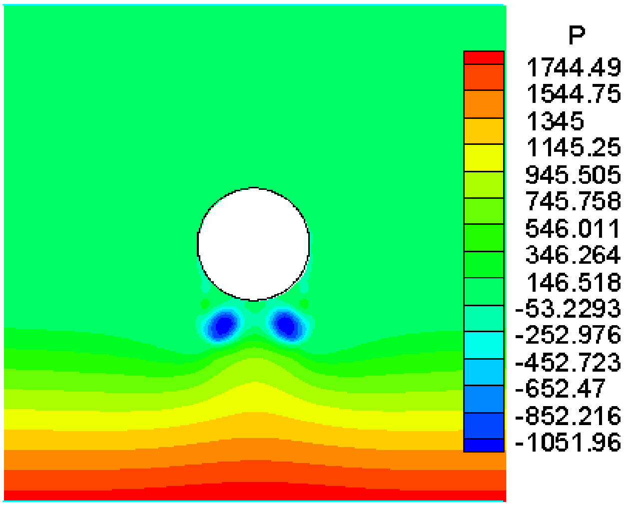

Figure 5.6 Predicted pressure distribution in Pascal at t=0.248s for the water exit described in Figure 5.5. The atmospheric pressure has to be added to obtain the total pressure.

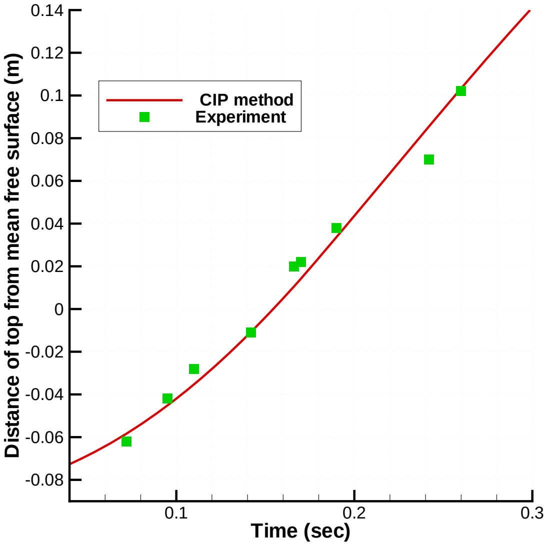

Figure 5.7 Distance from the cylinder top to mean free surface during water exit of a neutrally buoyant circular cylinder with a radius of 5.5cm.

Figure 5.7 shows the distance from the cylinder top to the mean free surface. From these figures, we can see that the simulations and experiment agree well.

5.3 Summary

The complicated free surface deformation during water entry and exit of a circular cylinder is simulated by CIP method with good agreement to the photographs taken from the experiments conducted by Greenhow & Lin (1983). During water entry with free motion, the non-viscous flow separation from the cylinder which is a difficulty for the other CFD methods is by no means trivial to predict numerically. Relatively small grids were used at the areas of flow separation since this prediction can be influenced by the grid size. The numerically predicted pressure distribution suggests that ventilation occurs but no cavitation occurs during water exit with constant force.

The motion of the circular cylinder for both water entry with free motion and water exit with constant force agrees also well with the experimental data.

CHAPTER 6

Water entry loads on ship sections

6.1 Introduction

Practical state-of-the-art computational tools for nonlinear wave-induced motions and loads on a ship handle the nonlinear effects in a simplistic way. The numerical codes typically assume potential flow with empirical viscous roll damping. Separate calculations are done for slamming loads on, for instance, a bow flare section. The state of the art in prediction of slamming loads on a symmetric ship cross-section with given vertical inflow conditions and body motions and based on 2D flow is generally satisfactory. However, water entry of a heeled section has not been extensively studied. This has, for instance, relevance for bow flare loads in bow sea with combined large roll motions and relative vertical motions; see Yamamoto et al. (1985). The motivation for their study was structural damage due to bow flare slamming. Because the heel angle decreases the relative impacting angle between the hull surface and the water surface, the maximum slamming pressures increase with the heel angle for a given relative vertical impact velocity. A challenge is to incorporate the slamming predictions in the global ship motion calculations. Because the slamming loads can be sensitive to the inflow conditions, an integrated approach is needed. This requires special considerations when the slamming duration is so short that local hydroelastic effects matter. Another application of our study is related to dynamic stability of high-speed vessels. Water entry results of a heeled wedge section can be combined with a 2D+t method to study how the steady hydrodynamic heel moment on a prismatic planing vessel on a straight course in calm water depends on the Froude number and the heel angle (Faltinsen, 2005).

6.2 Experimental setup

This chapter presents numerical and experimental results by the CIP-based finite difference method for water entry of bow flare and V-shaped sections. The experimental drop tests by Aarsnes (1996) for the ship sections shown in Figure 6.1 (see Table 6.1) are used. The test rig consists of four different parts: the vertical guide rails, the trolley, a rotable horizontal beam and the test section. The rotable beam is connected to the trolley using one bolt at each end of the beam. The ballast weights are located within the rotable beam. The trolley is engaged with the vertical guide rail. The test sections are mounted directly to the horizontal, rotable beam. The test sections are connected to the trolley during the entire drop. Any rotation of the test section is suppressed even during the impact phase. The free-falling rig is mounted in a small towing tank. The trolley is raised using a winch fitted with a quick-release hook. The hook is connected to an automatic release mechanism. After the test section has hit the water surface, the trolley is stopped, using two elastic ropes. The total drop section is divided into three parts, one measuring section with a dummy section on each side.

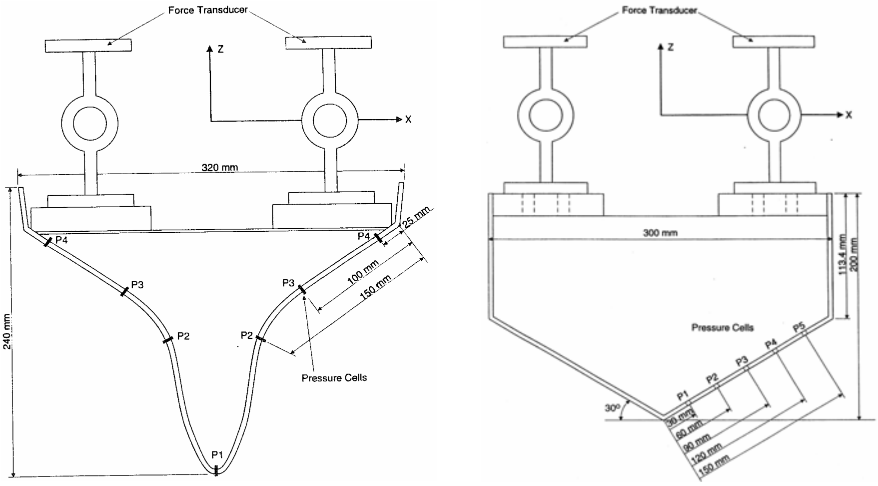

Figure 6.1 Details of the ship sections used in Aarsnes' (1996) experimental drop tests.

Three-dimensional flow effects at the measuring section are roughly estimated to cause an error of less than 5% relative to the assumed 2D flow. This was done by considering symmetric impact at the time instant when the spray roots are at the knuckles. The body boundary condition is transferred to a rectangular plate. The infinite-frequency free surface condition is assumed on the horizontal plane exterior to the plate. Tank wall effects are neglected. The problem is then equivalent to cross-flow without flow separation past a rectangular plate in an infinite fluid. Using information from the potential flow calculations by Meyerhoff (1970) gives the desired result.

Table 6.1 Data related to the experimental drop tests of the ship sections in Figure 6.1.

Cross-section	V-shaped	Bow flare
Breadth of section	0.300m	0.320m
Draft of section	0.200m	0.240m
Length of measuring section	0.100m	0.100m
Length of each dummy section	0.450m	0.450m
Total weight of drop rig	288kg	261kg
Weight of measuring section	10.3kg	6.9kg

The water entry problem of two ship sections is solved by using Newton's 2nd law, the CIP-based finite difference method and accounting for the total weight of the rig. Frictional forces along the guide rails are negligible. In this section, the free drop tests of these two ship sections with zero and non-zero heel angle are investigated.

6.3 Bow flare section

6.3.1 Zero heel angle

Comparisons between the drop test results and the CIP calculations of the vertical acceleration, velocity and hydrodynamic force *Fz* of the bow flare section at zero heel angle are presented in Figure 6.2. The maximum vertical hydrodynamic force occurs at the time when the spray roots are at the knuckles. The agreement is generally satisfactory. The experimental results contain an acceleration component oscillating with a frequency of about 100 Hz. This is associated with a natural frequency of the test rig and cannot be modeled in our numerical simulations. This oscillating acceleration part affects in particular the added mass force and represents an experimental error source.

Figure 6.3 presents comparisons of the time history of the pressures at the four points P1, P2, P3 and P4 defined in Figure 6.1. The pressure gauges have a diameter of 5 mm. The initial pressures at P1 are not well described by the numerical method. This is associated with the singular nature of the initial impact and has earlier been discussed for the initial impact force on a circular cylinder. A better way to theoretically predict the initial impact pressure at P1 is to use Wagner's theory and average the predicted pressure over the pressure measurement area. There is otherwise a reasonable agreement between the numerical and experimental pressure results. Zhao et al. (1996) used a nonlinear BEM without gravity and compared with Aarsnes (1996) drop test results for the bow flare section with another drop height. The experimental vertical velocity was used as input to the numerical simulation. The BEM predicted very well the vertical hydrodynamic force while the agreement in the pressure predictions was less satisfactory. A reason may be that the BEM calculations did not include gravity. This needs further investigations.

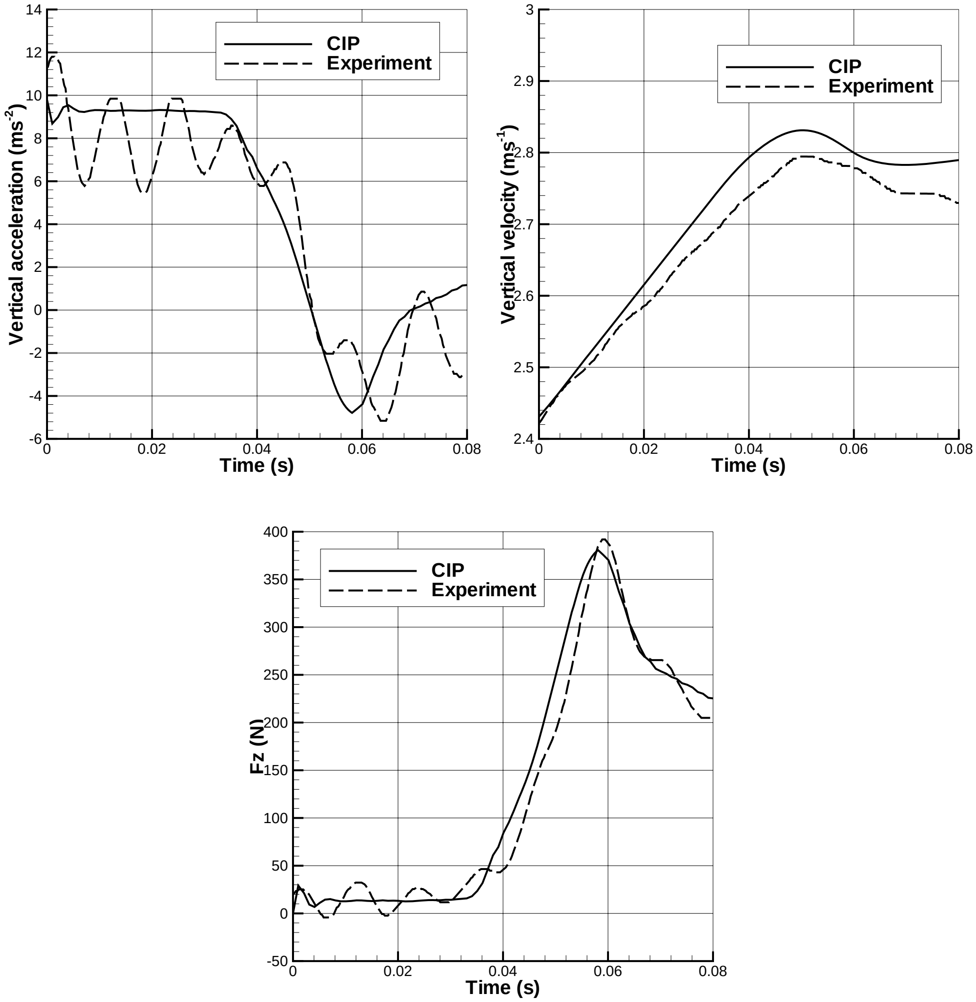

Figure 6.2 Comparisons between numerical and experimental time histories of vertical acceleration, velocity and hydrodynamic force Fz during drop test of bow flare section with zero heel angle. Drop height H=0.318m. t=0 corresponds to the initial impact time.

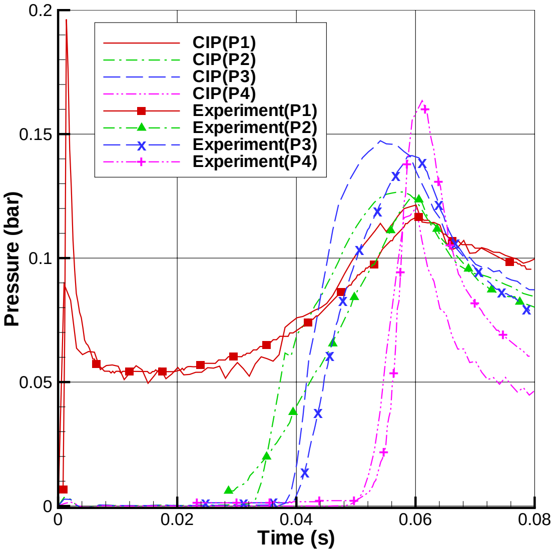

Figure 6.3 Comparisons between numerical and experimental time histories of pressure at P1, P2, P3 and P4 defined in Figure 6.1 during drop test of bow flare section with zero heel angle. Velocity, acceleration and vertical force are shown in Figure 6.2.

6.3.2 Non-zero heel angle

Figure 6.4 to Figure 6.8 present numerical and experimental drop test results when the bow flare section has a heel angle β of 4.8˚, 9.8˚, 14.7˚, 20.3˚ and 28.3˚, respectively. The vertical distance H between the initial position of the keel and the free surface is indicated in the figures. The initial impact time t=0 was experimentally determined by wave gauge tape mounted on the surface of the test section.

The measured results have been lowpass filtered using a cutoff frequency of 300 Hz. The experimental results contain an acceleration component oscillating with a governing frequency of about 100 Hz. This is due to eigenfrequency oscillations of the test rig. The high frequency acceleration oscillations have a small influence on the drop velocity, but are evident as added mass forces in the experimental force results. A large influence of the test rig oscillations is apparent on the horizontal water entry force for the small heel angles. The vibrations of the test rig are present even before the section hits the calm water surface and are probably excited during the release of the test section. The test rig vibrations affect the initial impact time. The numerical simulations before the impact are very similar to a ‘free fall’ behavior with negligible influence of air resistance. There is a small difference in the experimental and numerical initial impact velocity for the bow flare section.

We note a phase lag between the numerical and experimental force results, i.e. the time when the water entry force is maximum, differs in the experiments and the CIP simulations. The maximum numerically predicted force occurs when the spray root is at the knuckle on the windward side.

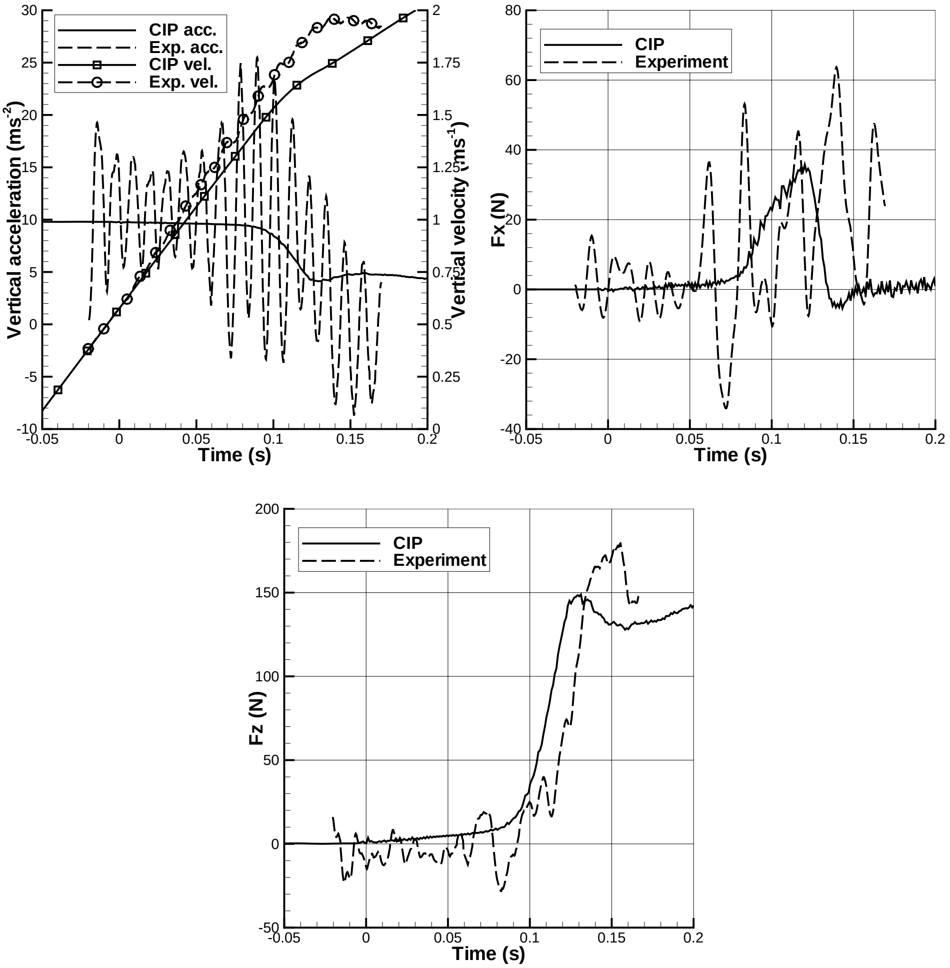

Figure 6.4 Acceleration, velocity, horizontal (Fx) and vertical (Fz) hydrodynamic force during drop test of bow flare section. t=0 initial impact time. Drop height H=0.017m. Heel angle β=4.8°.

No ventilation occurred at the leeward hull side in the numerical predictions. This is consistent with the experimental results except when the heel angle is 28.3°. No cross-flow and viscous flow separation that could trigger ventilation were apparent at the keel in the numerical simulations. The fact that ventilation occurred in the experiments on the leeward side of the bow flare section at the heel angle 28.3° may be affected by the test rig vibrations. Let us as a simplification decouple this effect of the test rig vibrations from the water entry problem. We then have the body oscillating with high frequency. Let us as a further simplification assume that the oscillation only causes an added mass force. This added mass force is a consequence of the hydrodynamic pressure which will be oscillating in time. It can be negative or positive, depending on the sign of the acceleration. If the pressures on the body associated with the added mass force is negative relative to atmospheric pressure during part of an oscillation cycle and if this occurs close to the free surface, ventilation may be triggered.

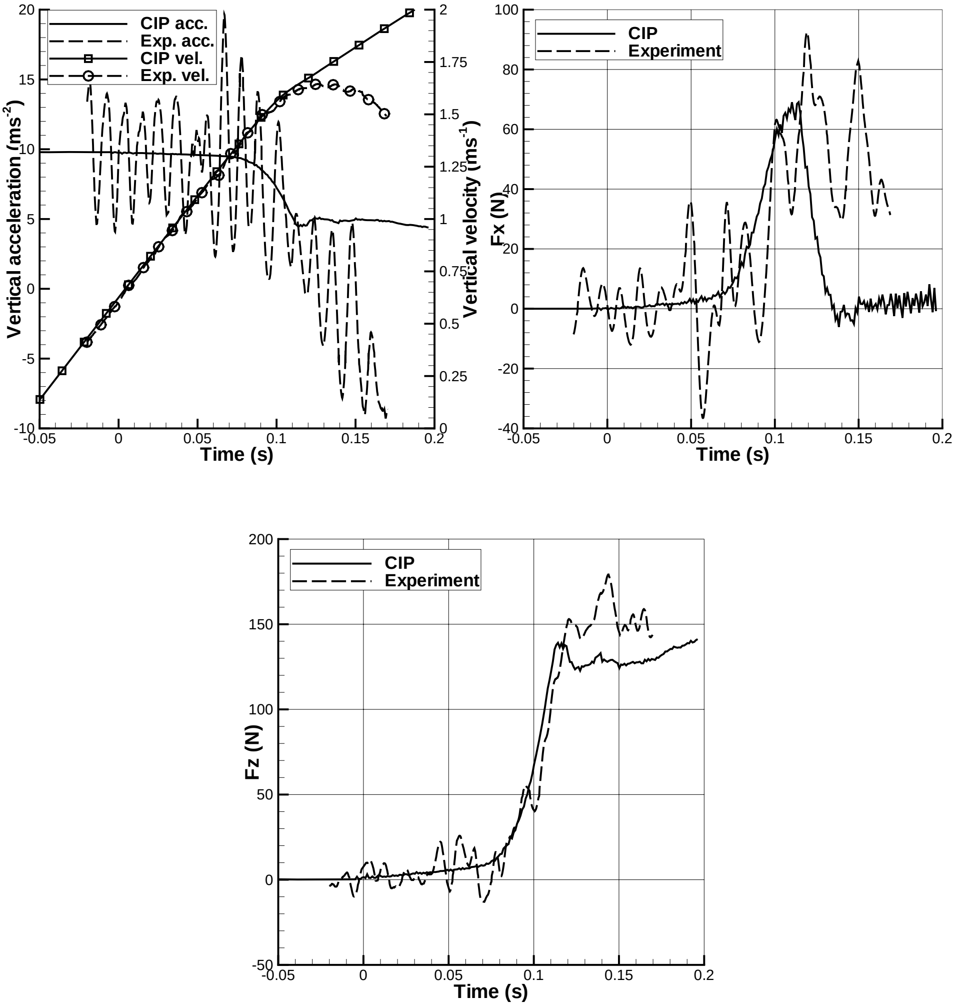

Figure 6.5 Acceleration, velocity, horizontal (Fx) and vertical (Fz) hydrodynamic force during drop test of bow flare section. t=0 initial impact time. Drop height H=0.02m. Heel angle β=9.8°.

The elastic ropes used to stop the model, cause an experimental bias error at the later stage of the water entry. An indication when this bias error matters can be found by comparing experimental and numerical predictions of vertical velocity and acceleration. For instance, the CIP calculations for the heel angle 9.8˚ (see Figure 6.5) deviate significantly from the experiments when the time is larger than 0.12s. We could say by accounting for the presence of experimental errors that there is a reasonable agreement between experiments and theory. The largest difference in the peak value of the vertical force occurs for the largest heel angle. One reason is that the leeward side ventilated in the experiments, while the leeward side was wet in the numerical simulations.

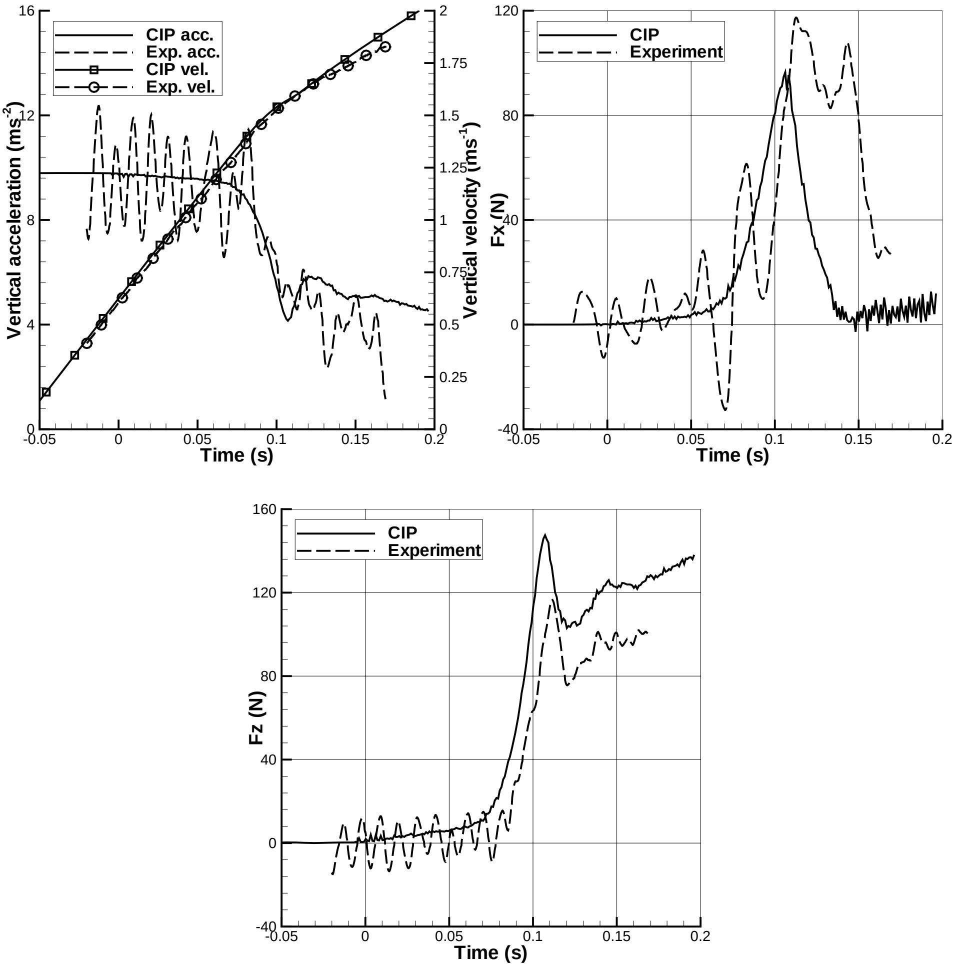

Figure 6.6 Acceleration, velocity, horizontal (Fx) and vertical (Fz) hydrodynamic force during drop test of bow flare section. t=0 initial impact time. Drop height H=0.02m. Heel angle β=14.7˚.

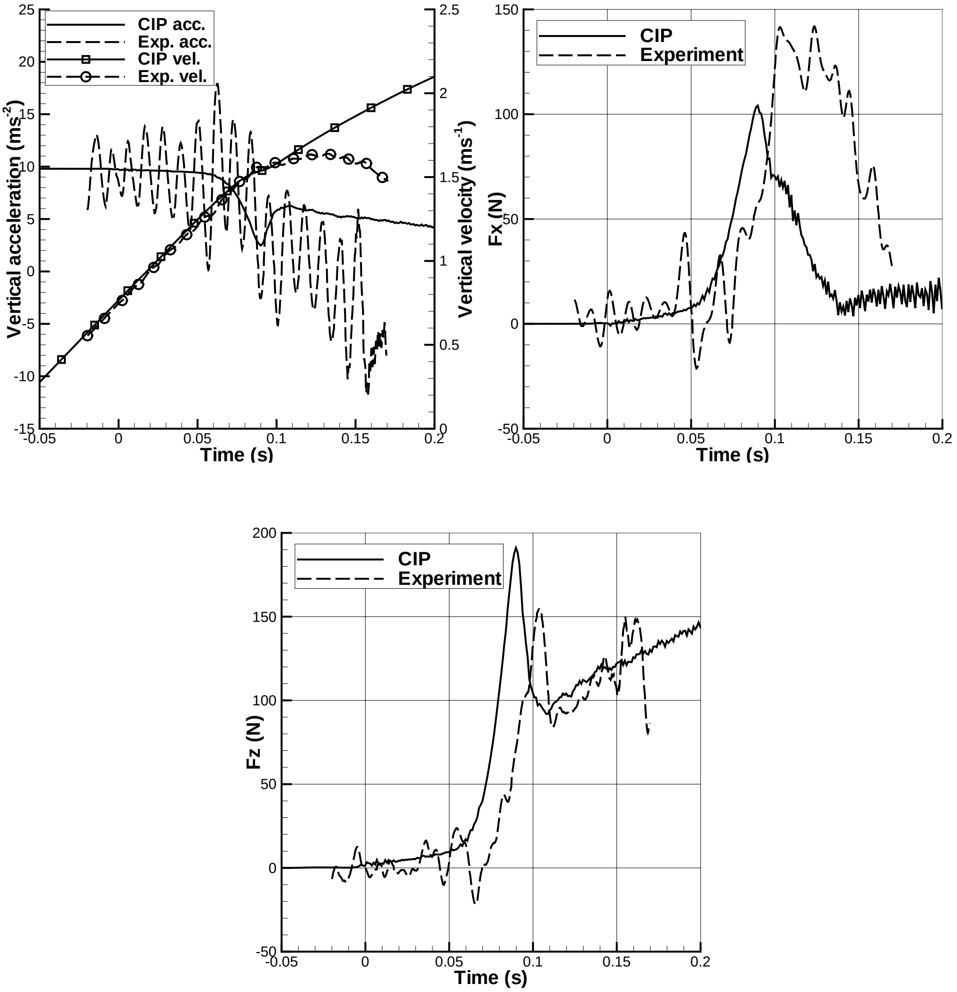

Figure 6.7 Acceleration, velocity, horizontal (Fx) and vertical (Fz) hydrodynamic force during drop test of bow flare section. t=0 initial impact time. Drop height H=0.03m. Heel angle β=20.3˚.

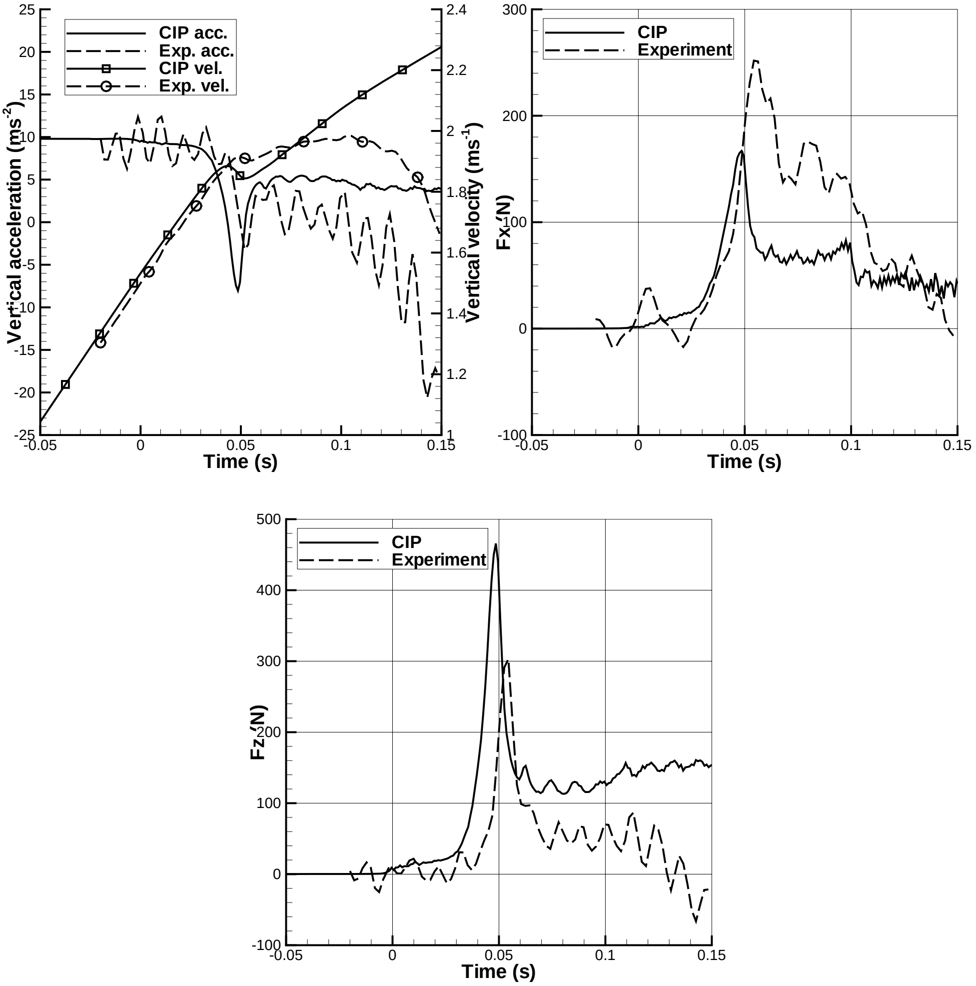

Figure 6.8 Acceleration, velocity, horizontal (Fx) and vertical (Fz) hydrodynamic force during drop test of bow flare section. t=0 initial impact time. Drop height H=0.12m. Heel angle β=28.3°.

6.4 V-shaped section

6.4.1 Zero heel angle

The free drop test results of the V-shaped section with zero heel angle are presented in Figure 6.9 to Figure 6.11, including time histories of vertical acceleration, velocity and hydrodynamic force Fz. The test model was freely dropped from different height H of 0.50m, 0.313m and 0.195m, respectively. The experimental results of acceleration contain a component oscillating with a frequency of about 250 Hz. This is associated with a natural frequency of the test rig and cannot be modeled in our numerical simulations as previously stated for the bow flare section. This oscillating acceleration part affects in particular the added mass force and represents an experimental error source. The numerical vertical velocity is 4-5% larger than the experimental results. The agreement of vertical force is generally satisfactory.

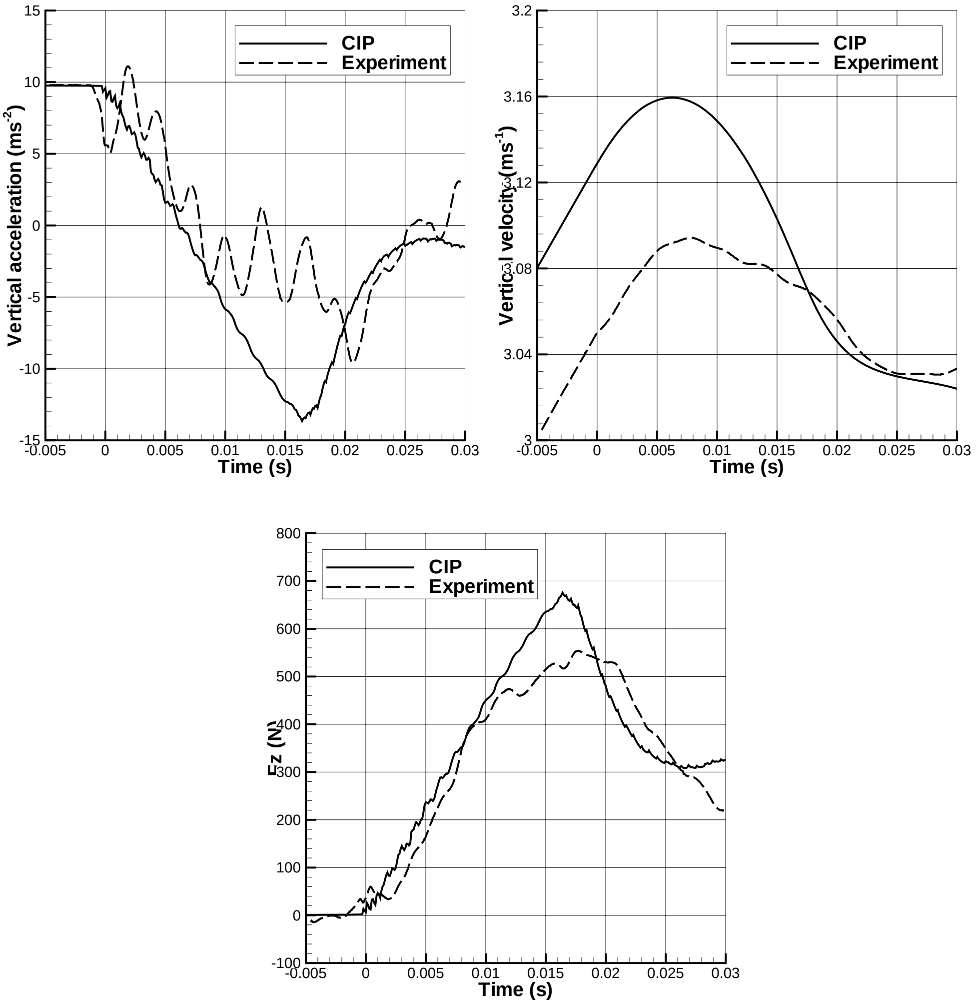

Figure 6.9 Vertical acceleration and velocity, and vertical hydrodynamic force Fz during drop test of V-shaped section with zero heel angle. Drop height H=0.50m. t=0 initial impact time.

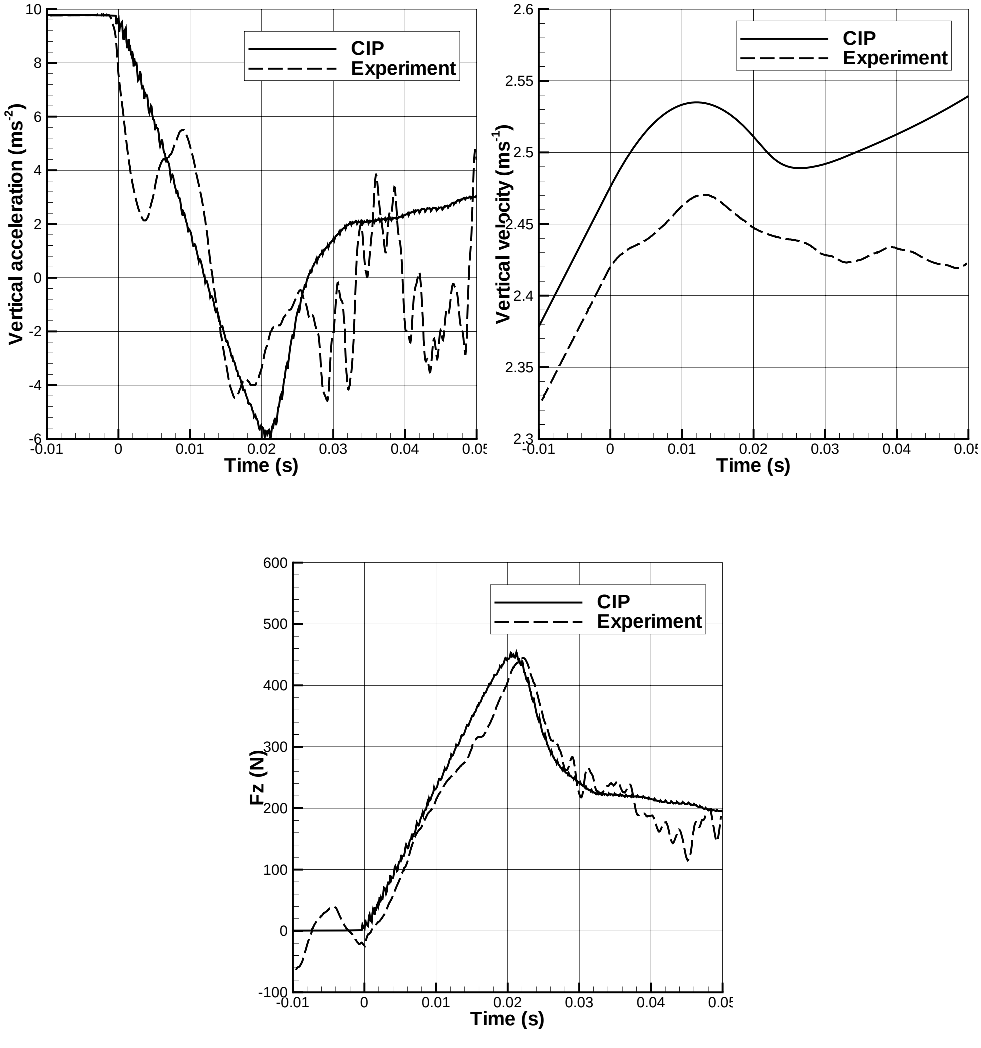

Figure 6.10 Vertical acceleration and velocity, and vertical hydrodynamic force Fz during drop test of V-shaped section with zero heel angle. Drop height H=0.313m. t=0 initial impact time.

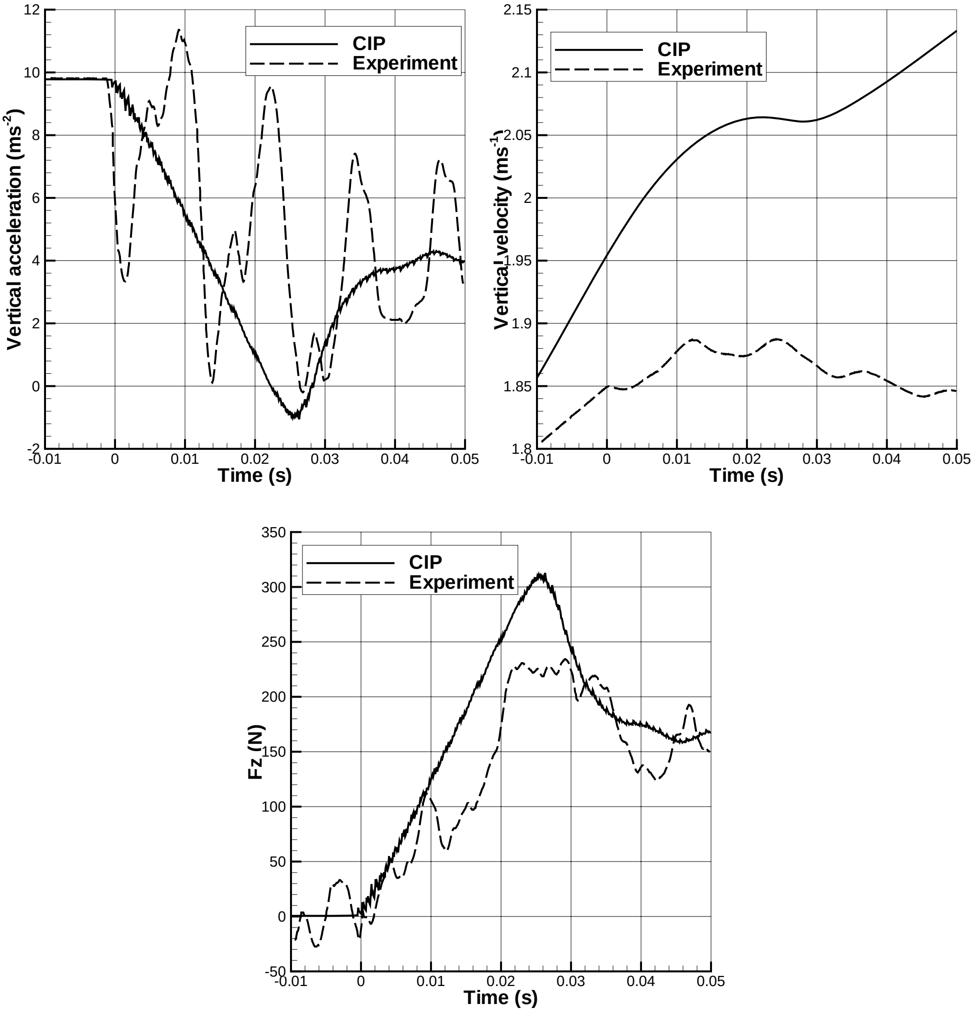

Figure 6.11 Vertical acceleration and velocity, and vertical hydrodynamic force Fz during drop test of V-shaped section with zero heel angle. Drop height H=0.195m. t=0 initial impact time.

6.4.2 Non-zero heel angle

Figure 6.12 to Figure 6.15 show the comparisons between the numerical and experimental time histories of vertical acceleration, velocity and hydrodynamic force *Fz* during the drop tests of the V-shaped section with finite heel angle. The measured results for accelerations and forces have been lowpass filtered using a cutoff frequency of 700 Hz. The oscillations with frequency about 250 Hz are due to an eigenfrequency of the drop rig. As noted earlier, the vibrations are present even before the section hit the calm water surface and influence the initial impact condition. The numerical vertical velocity which is consistent with the result of the free falling body without air resistance is about 4-5% larger than the experimental result. The overall agreement of the vertical force is good.

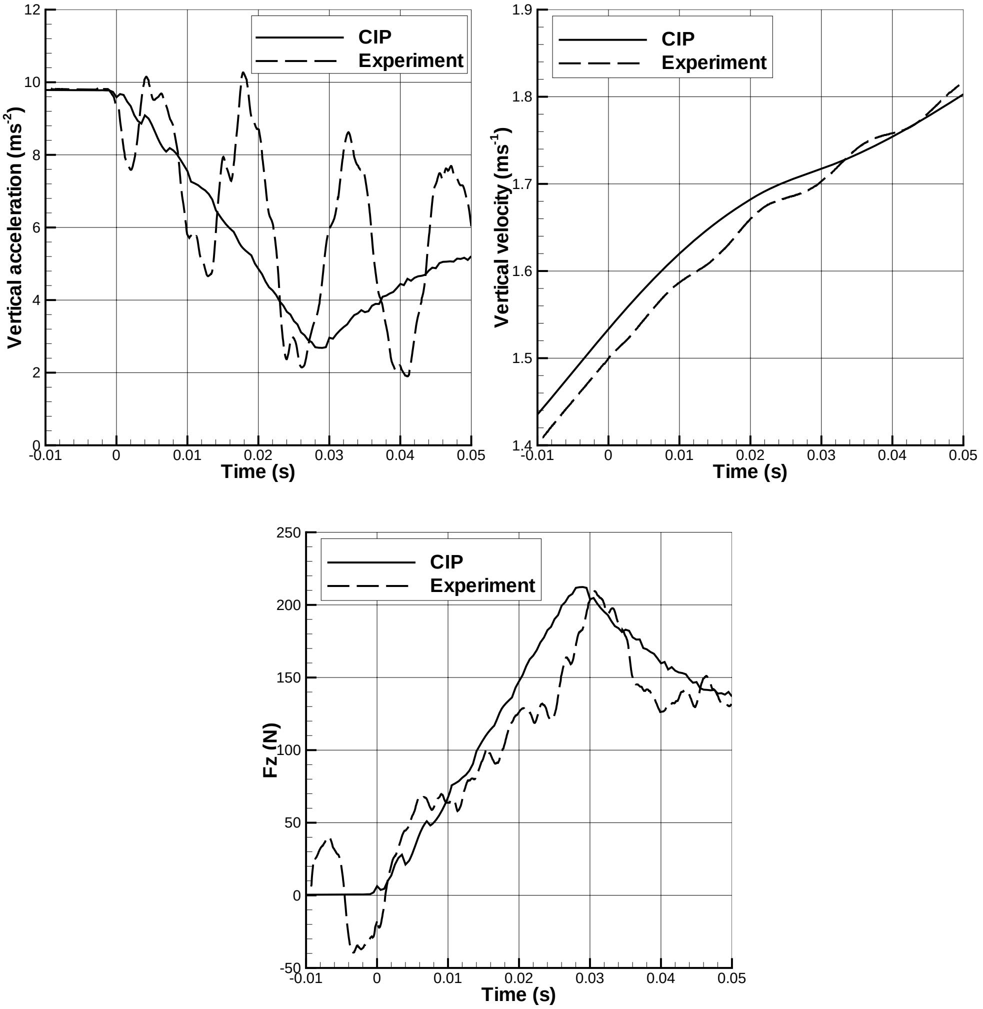

Figure 6.12 Vertical acceleration and velocity, and vertical hydrodynamic force Fz during drop test of V-shaped section. t=0 initial impact time. Drop height H=0.12m. Heel angle β=4.8°.

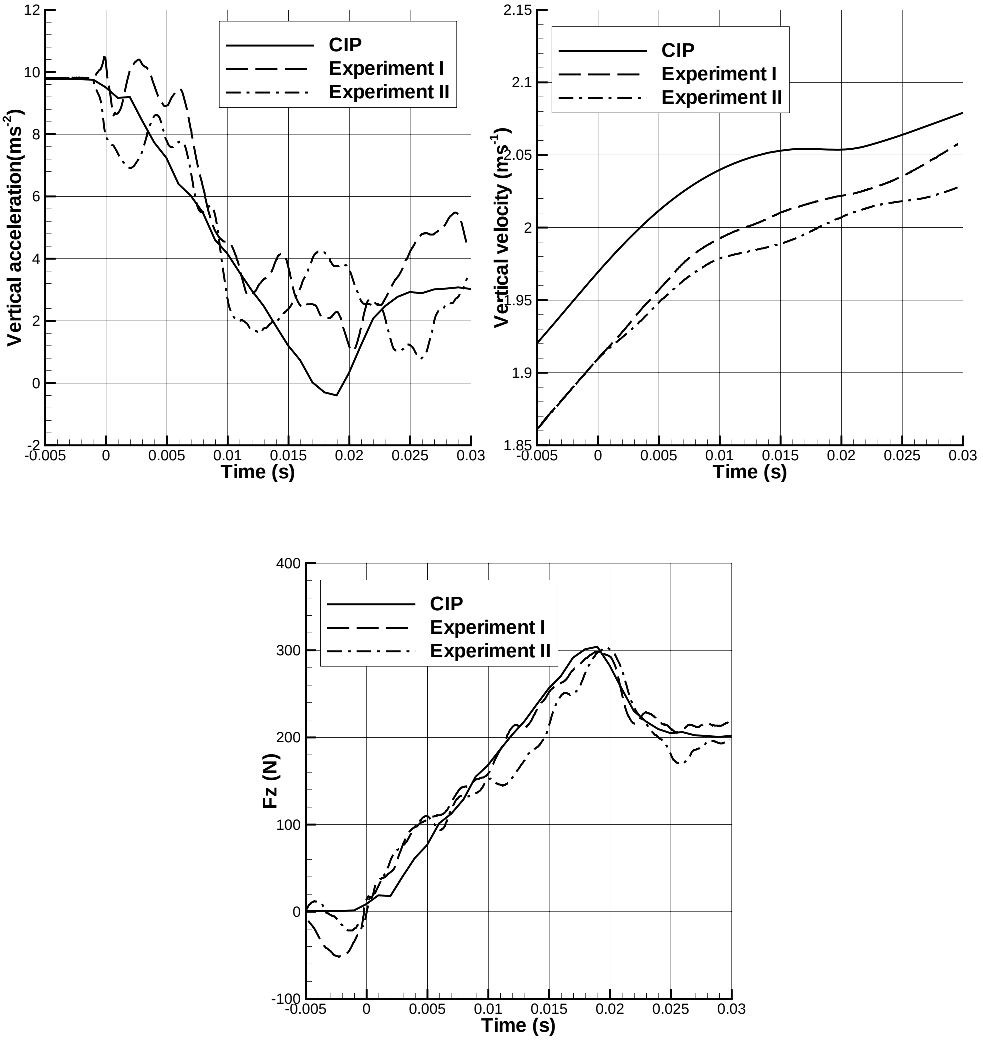

Figure 6.13 Vertical acceleration and velocity, and vertical hydrodynamic force Fz during drop test of V-shaped section. t=0 initial impact time. Drop height H=0.198m. Heel angle β=9.8°.

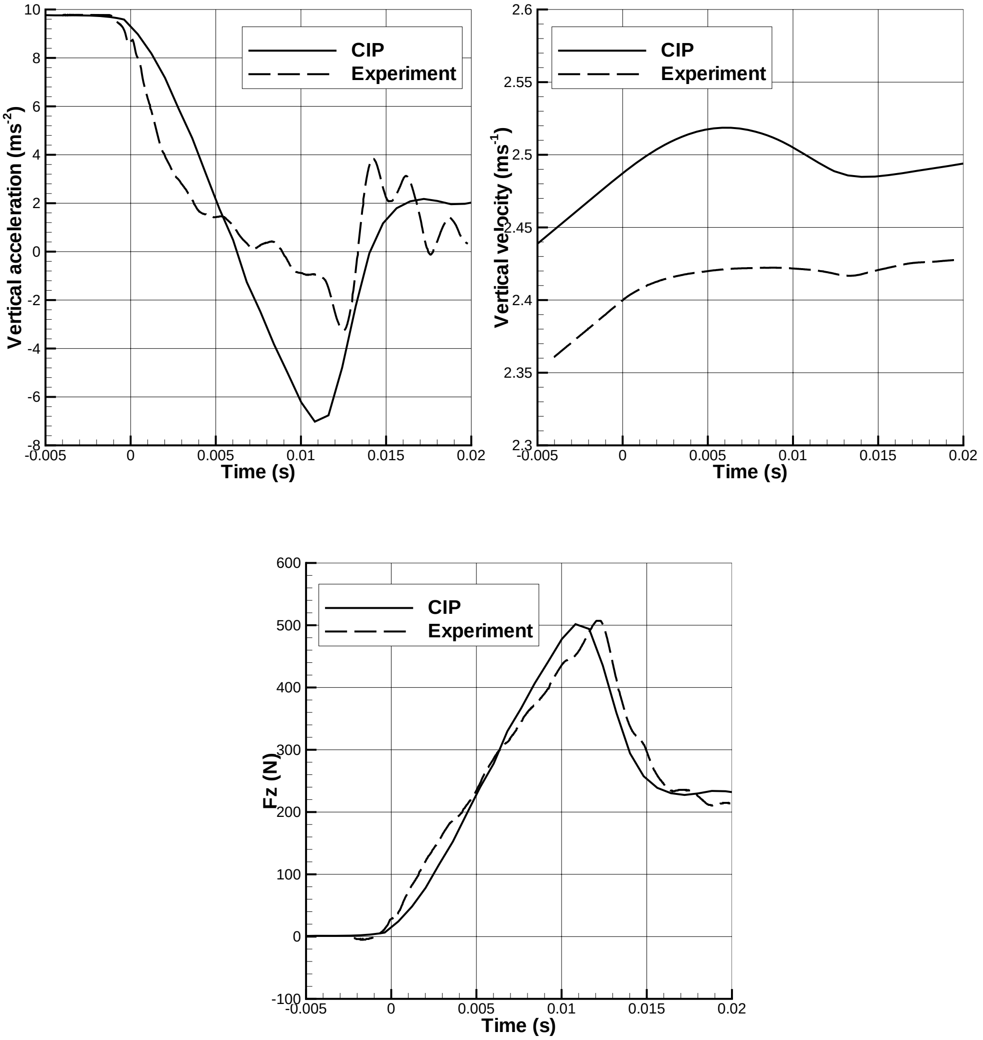

Figure 6.14 Vertical acceleration and velocity, and vertical hydrodynamic force Fz during drop test of V-shaped section. t=0 initial impact time. Drop height H= 0.316m. Heel angle β=14.7°.

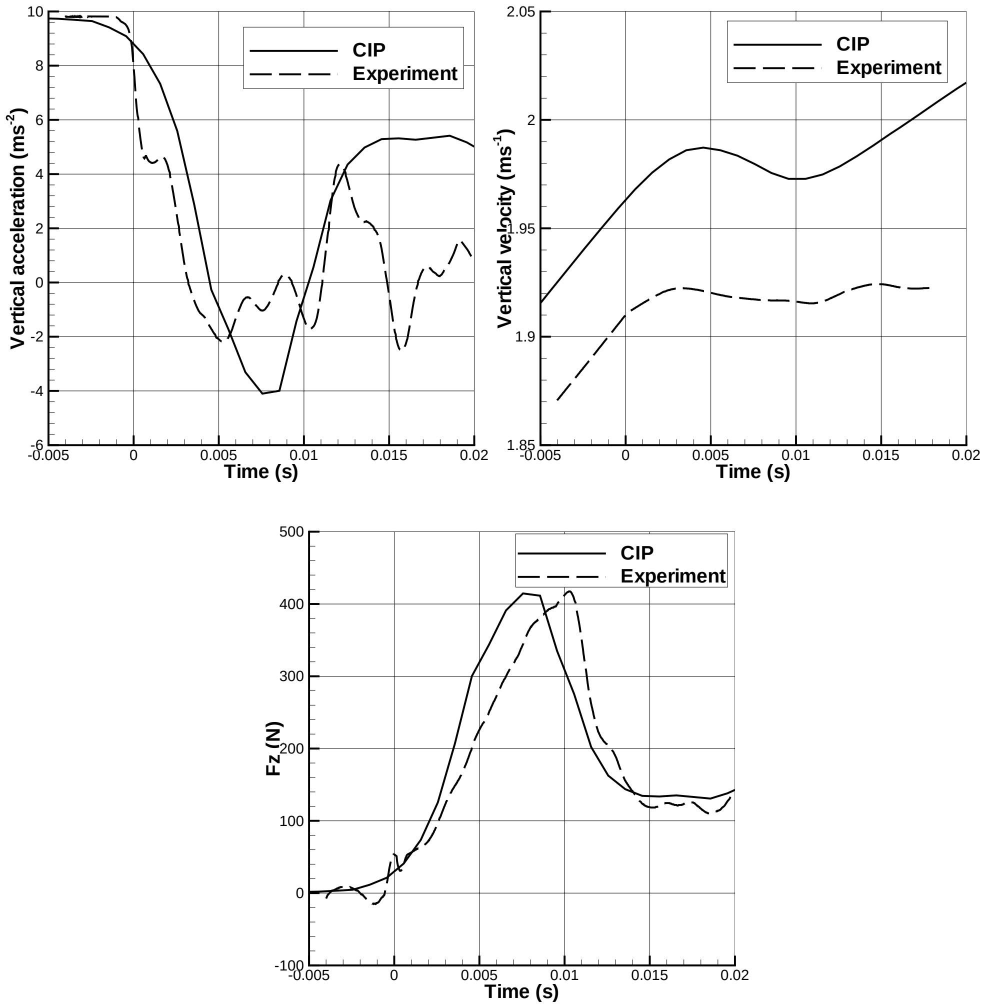

Figure 6.15 Vertical acceleration and velocity, and vertical hydrodynamic force Fz during drop test of V-shaped section. t=0 initial impact time. Drop height H=0.197m. Heel angle β=20.3˚.

6.4.3 Critical heel angle

Both the numerical simulations and the experiments showed that the leeward side was wetted for the heel angles β equal to 4.8˚, 9.8˚, 14.7˚ and 20.3˚. This is consistent with the theoretical results by Judge et al. (2004) who presented critical angles at which ventilation occurs off the vertex of a wedge as a function of deadrise angle, heel angle and the ratio U/W between the horizontal and vertical water entry velocity components.

We compared our numerical results with the experimental results by Judge et al. (2004) when U/W=0.75 and the deadrise angle is 37˚. The critical heel angle in the experiments is between 25˚ and 30˚ while their theoretical estimate was 22˚. Figure 6.16 shows our numerical predictions of the free surface elevation when the heel angle is 30˚. Our numerical procedure does not predict a sharp interface between the water and the air. The density function φ_1 is theoretically 1 in the water and zero in the air. However, φ_1 varies continuously between 1 and 0 in the grid cells close to the interface in the numerical simulations. The free surface prediction in Figure 6.16 is based on $\varphi_1 = 0.5$ and is consistent with the fact that ventilation occurs. Further, the free surface shape is in overall agreement with a picture presented by Judge et al. (2004). However, the fine details of the free surface at the vertex are not correct. This deficiency of our numerical method was more evident when studying a heel angle of 34˚.

The free surface may, according to the local potential flow analysis by Faltinsen (2005), be expressed as $Z=AX^{3/2}$. The origin of the Cartesian coordinate system X-Z is at the vertex. The X-axis coincides with windward wedge side and is pointing in the down-stream direction. The constant A must be determined by a global flow analysis. The consequence of the local flow analysis is that the water flow leaves tangentially at the vertex, i.e. the free surface is parallel to the windward wedge side at the vertex. This is not consistent with our numerical predictions. One reason may be associated with the fact that the theoretical pressure gradient on the windward wedge side is infinite at the vertex. The numerical scheme does not account for this singular behavior. There is also the possible effect of viscosity.

Our numerical results gave no ventilation at the heel angle of 25˚. This is consistent with the experiments. Even though we predicted ventilation at a heel angle of 34˚, the numerically predicted free surface was not in satisfactory agreement with a picture presented by Judge et al. (2004). The predicted length of the hollow on the leeward side was too small.

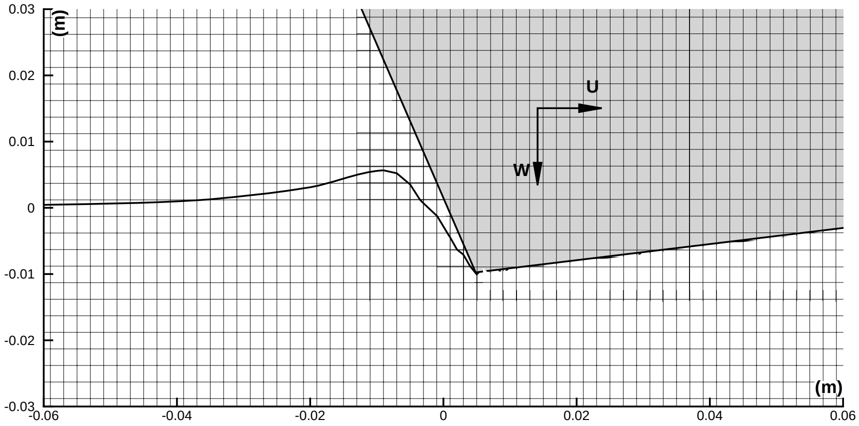

Figure 6.16 Numerically predicted free surface elevation during drop test of V-shape section with deadrise angle 37˚. U/W=0.75. Heel angle β=30˚. W=1.0 ms^{-1}. The rectangular grid system used in the calculations is indicated.

The numerical code failed to predict the water entry force on the V-shaped section in Aarsnes' (1996) experiments when the heel angle is 28.3°. Because the angle between the windward hull side and the calm free surface is only 1.7° at the initial impact, an air cushion is probably generated (Koehler & Kettleborough, 1977). This requires that air compressibility is accounted for in the numerical method. Further, hydroelasticity may matter when the relative impact angle is only 1.7° (Faltinsen, 2005). Muthu (2003) demonstrated that hydroelasticity may influence hydrodynamic loads when the relative impact angle is small. Because no detailed structural data were documented by Aarsnes (1996), we did not try to include structural elasticity in the numerical code.

6.5 Maximum impact force vs. heel angle

The numerically calculated non-dimensional maximum impact force $F_{max}/(0.5\rho V^2BL)$ as a function of the heel for the considered bow flare and V-shaped sections starts to increase significantly with the heel angle when the heel angle is larger than 10°; see Figure 6.17. Here F_{max} is the maximum force, V is the velocity at maximum force; B is the maximum breadth; L is the length of the measuring section. The results are dependent on the Froude number $V/\sqrt{gB}$ and the time history of the water entry velocity. Viscous forces and Reynolds number matter only when viscous flow separation occurs at curved surfaces. This is not evident in the numerical simulations.

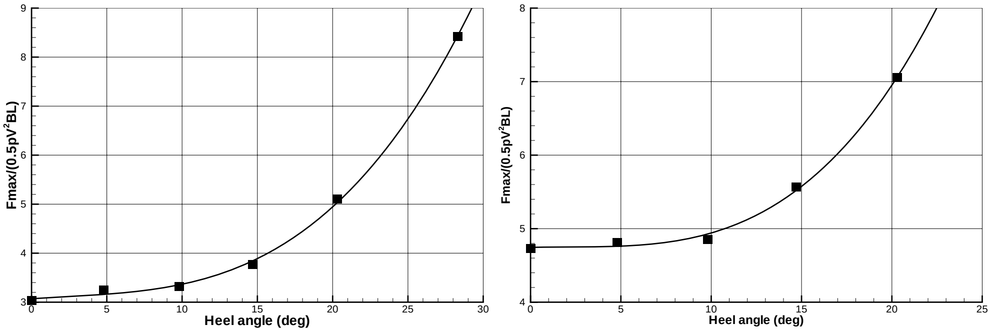

Figure 6.17 The non-dimensional maximum impact force as a function of heel angle β for bow flare section (left) and V-shaped section (right) for the considered test cases.

6.6 Summary

The CIP-based finite difference method has been applied to 2D water entry of vertical and heeled bow flare and V-shaped sections. The results for the bow flare section have relevance for slamming loads on a ship in bow sea with large roll oscillations and relative vertical motions. The results for the heeled V-shaped section can be combined with a 2D+t numerical method to study how the steady heel moment on a prismatic planing hull on a straight course in calm water depends on the Froude number (Faltinsen, 2005).

A generally satisfactory agreement with experimental drop test results of vertical water entry velocity, vertical and horizontal hydrodynamic forces as a function of time is demonstrated. This includes the effect of flow separation from the knuckle. The experiments, but not the numerical simulations, show ventilation of the leeward side of the bow flare section at the largest examined heel angle 28.3°. The leeward side is wetted in all other conditions in the experiments and the numerical simulations.

Bias errors due to eigenfrequency oscillations of the test rig and the use of elastic ropes to stop the models affect the results. An important effect of the eigenfrequency oscillations is their effect on the added mass forces.

The CIP method fails in the experimental test case when the angle between the windward hull side of the V-shaped section and the free surface is 1.7°. This small relative impact angle causes probably an air cushion extending from the keel to the knuckle on the windward side. Local hydroelastic effects are important to consider at low relative impact angles (Faltinsen, 2005). This requires modeling of structural elasticity effects. Because the local structural elasticity properties of the experimental models are unknown and our numerical model presently assumes a rigid body, the hydroelastic slamming effect could not be studied.

Because the slamming loads are sensitive to the inflow conditions, the slamming calculations should be integrated in the global ship motion calculations. Our studies are a step towards developing rational CFD methods for predicting strongly nonlinear wave-induced motions and loads on a ship.

CHAPTER 7

3D study of green water on the deck of a ship

7.1 Introduction

The 3D version of the CIP code has been applied to green water on deck in Faltinsen, Zhu & Hu (2005). A Wigley model was selected in the simulations. The main particulars are described in Table 7.1. The ratio between the freeboard and the ship length is only 0.03. The deck house height-to-ship length ratio is also 0.03. However, one would have chosen the freeboard and the deck house height to be larger for a real ship. The Froude number $F_n = V/\sqrt{gL}$ is 0.25 where L is the ship length, and head sea incident regular waves are assumed. Second-order Stokes waves were used to describe the incident wave field. The wavelength is the same as the ship length and the wave height is 0.1m. When the wave steepness is 1/10 as in this case, a second-order wave theory is not perfect but can be considered as a reasonable approximation relative to an infinite-order Stokes wave, see Faltinsen (2005). A sketch of the 3D numerical wave tank is shown in Figure 7.1.

The predicted heave (η_3) of the centre of the gravity and the pitch (η_5) motions are shown as a function of t/Tw in Figure 7.2. Tw is the wave period. Positive heave is upwards and positive pitch corresponds to bow down. We note that steady-state conditions have not been obtained in the considered time interval. The ratio between maximum absolute value of heave and half the incident wave height is 0.5, i.e. we are not in the resonant conditions for the vertical motions. This will occur for a longer wavelength.

Table 7.1 Data for a Wigley hull in a 3D numerical wave tank

Ship model	Length at waterline	1.0 *m*
	Beam at midships	0.2 *m*
	Draft	0.0625 *m*
	Displaced volume	0.00555 m^3
	Freeboard	0.03 *m*
	Centre of gravity above base	0.0551 *m*
	Gyration radius in pitch	0.225 *m*
	Froude number	0.25
	Reynolds number	$1.174\text{x}10^6$
Incident waves	Wave theory	Second-order Stokes
	Wavelength λ	1.0 *m*
	Wave height H	0.1 *m*
	Water depth h	4.0 *m*
Grid number	$165(x) \times 80(y) \times 80(z)$	
Min grid space	$0.006\text{m}\ (x) \times 0.005\text{m}\ (y) \times 0.005\text{m}\ (z)$	

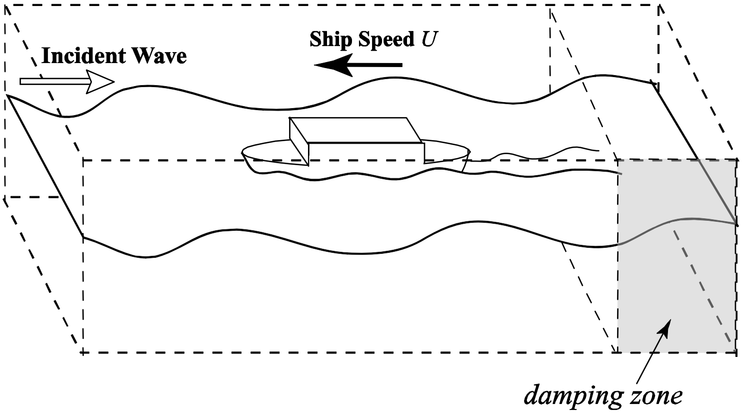

Figure 7.1 Sketch of the 3D numerical wave tank.

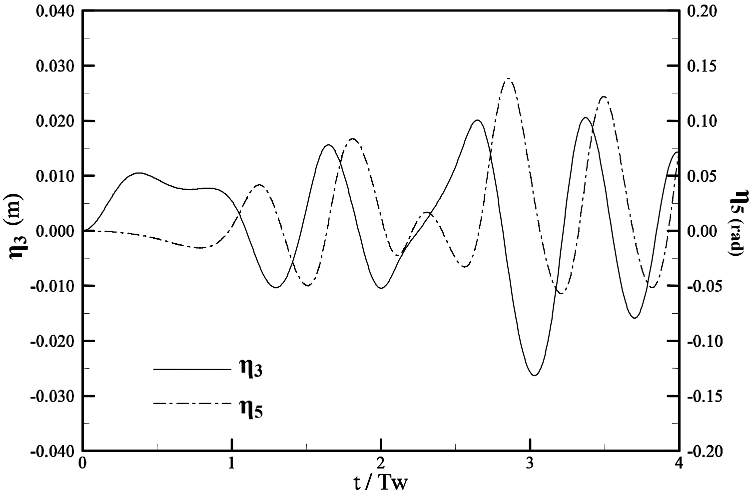

Figure 7.2 Predicted pitch (η_5) and heave (η_3) of the center of the gravity as a function of non-dimensional time t/Tw for a Wigley hull in regular head sea waves with wave height-to-wavelength ratio 0.1 and wavelength-to-ship length ratio 1.0. Fn=0.25. Tw=wave period.

7.2 3D water-on-deck simulations for a Wigley hull

The wave-induced ship motions and the free surface configuration during one encounter period are illustrated in Figure 7.3. We note severe green water on the deck impacting against the deck house and causing water even on the top of the deck house. When t/Tw=3.4, the rise of a vertical wall of water at the sides of the deck in the bow has started. The bow part of the deck is totally wetted at t/Tw=3.5 and a 3D nearly vertical wall of water is propagating along the deck. This behavior differs from the well-known dam-breaking phenomenon associated with green water on the deck. The vertical wall of water created along the sides of the deck will then not continue being a vertical wall as the water propagates with the largest velocity along the deck.

We see a tendency to a dam-breaking behavior of the water on deck at t/Tw=3.6 in Figure 7.3, i.e. the water moves with the largest velocity at the deck. The flow from the sides meets at the centre plane where the free surface elevation is increased. It looks as a tongue of water. The largest longitudinal velocity at the deck is associated with this tongue of water at the centre plane. A tongue of water was also shown in the experimental studies by Barcellona et al. (2003) for a stationary ship restrained from oscillating.

t/Tw=3.0

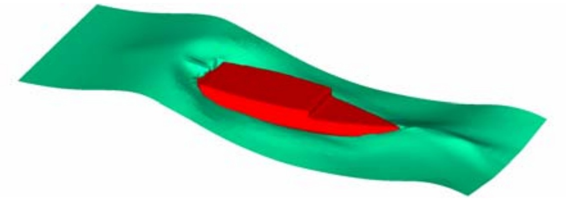

t/Tw=3.1

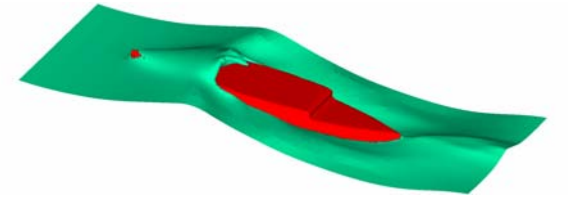

t/Tw=3.2

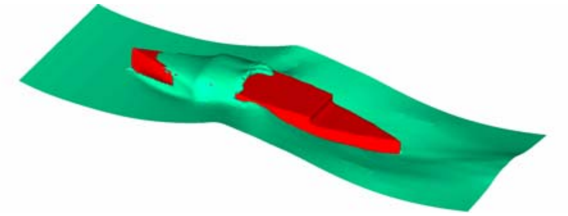

t/Tw=3.3

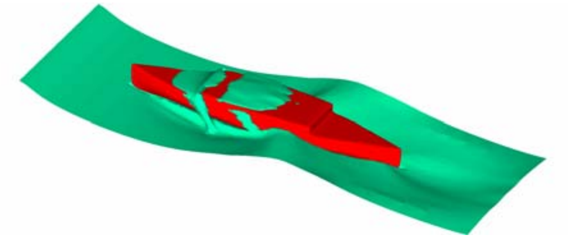

t/Tw=3.4

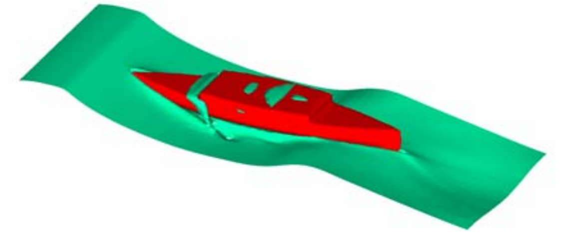

t/Tw=3.5

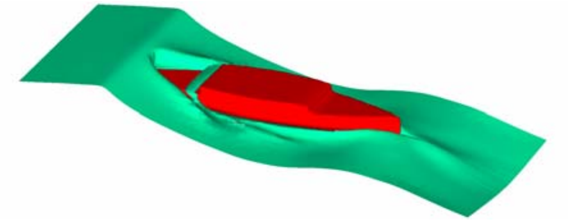

t/Tw=3.6

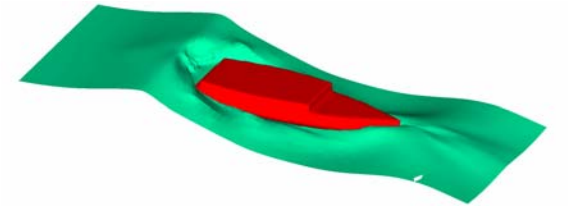

t/Tw=3.7

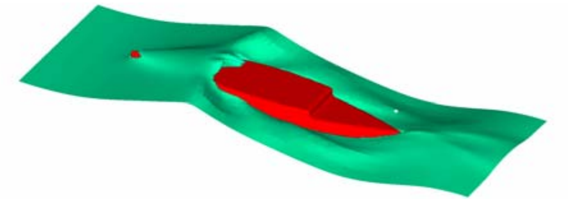

t/Tw=3.8

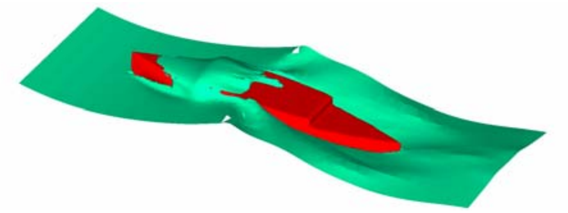

t/Tw=3.9

Figure 7.3 3D water-on-deck simulations for a Wigley hull in regular head sea waves with wave height-to-wavelength ratio 0.1 and wavelength-to-ship length ratio 1.0. Fn=0.25. Tw=wave period.

7.3 Detailed Flow in the centre plane and at the bow of the Wigley hull

The reason for the difference in behavior of how the water comes on the deck at the bow is believed to be associated with the ratio between the relative vertical velocity W_{RB} and the relative longitudinal velocity U_{RB} in the bow. If this ratio is large, we expect a dam-breaking type of water on deck. When W_{RB}/U_{RB} is order one or smaller, the water may enter the deck as a plunging wave impacting against the deck. This is clearly illustrated in Figure 7.4 by 2D experimental results with a stationary ship-like body that was restrained from oscillating. Similar behavior was experimentally confirmed by Barcellona et al. (2003) for 3D stationary ship models with blunt bow that were restrained from oscillating. At the later stages of the water flow on the deck, i.e. after the break-down of the cavity created by the impacting plunging breaker, the flow has similarities with the dam-breaking flow. This means that the flow velocity is largest at the deck.

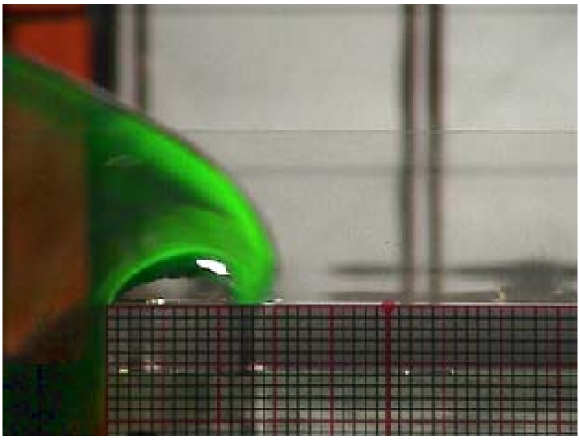

Figure 7.4 The initial phase of water on the deck of a 2D ship-like body that was restrained from oscillating. A plunging wave impacts against the deck and an air cushion is created (Greco, 2001).

The ratio W_{RB}/U_{RB} is not very large when the water enters the deck in our case. This can be seen from the calculated results in Figure 7.5, where we present the detailed flow pictures in the centre plane with t/Tw from 3.4 to 3.9. A relative-frame moving with the forward velocity of the ship is used. The relative-frame flow velocity vectors in the centre plane and the vertical velocities of the bow are indicated. This confirms that we should not expect a dam-breaking behavior when the water enters the deck. However, the water does not enter the deck as a plunging breaker, i.e. as in Figure 7.4. A reason may be insufficient grid discretization.

Another reason may be that our case is with a sharp bow and small bow entrance angle while the cases by Barcellona et al. (2003) and in Figure 7.4 correspond to blunt bows. The free surface profile at t/Tw=3.45 appears as the start of a plunging breaker, but the water velocity at the deck will subsequently increase so that a nearly vertical wall of water propagates along the deck at t/Tw=3.5. A similar behavior was observed experimentally by Buchner (1995) for a stationary free-floating FPSO with a blunt bow. The water has started to move with largest velocity at the deck at t/Tw=3.55. The velocity at the deck is then larger than 2ms^{-1}, which by using Froude scaling to be a full scale condition with a 100m long vessel corresponds to a velocity larger than 20ms^{-1}. An object exposed to this impact velocity will experience severe loads that depend on the slope of the free surface at the front of the propagating water; see Greco (2001) for more details. The fact that the interior angle of the water front along the deck is much larger than for a dam-breaking flow causes a much larger impact loads for a given impact velocity.

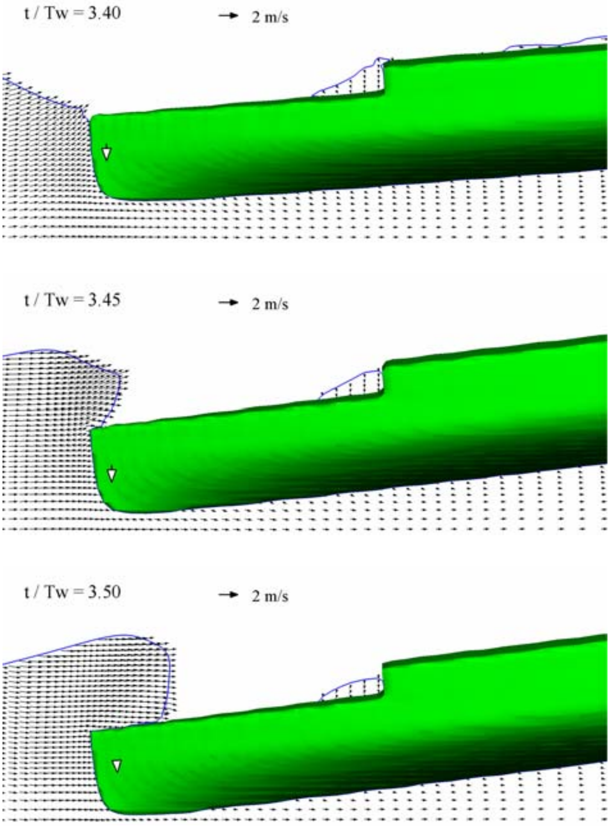

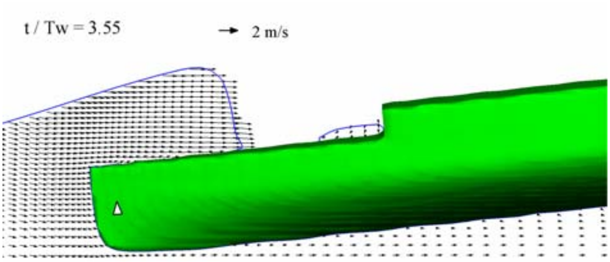
t / Tw = 3.55
2 m/s

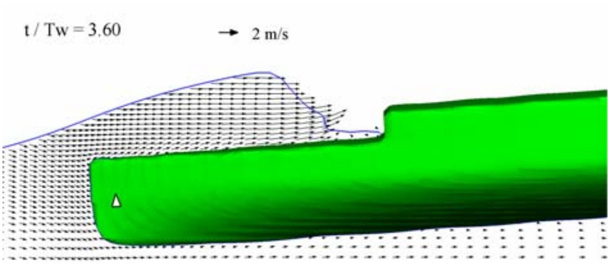
t / Tw = 3.60
2 m/s

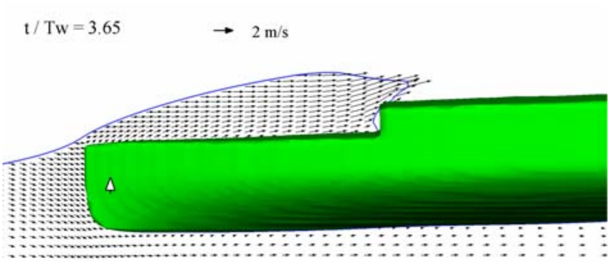
t / Tw = 3.65
2 m/s

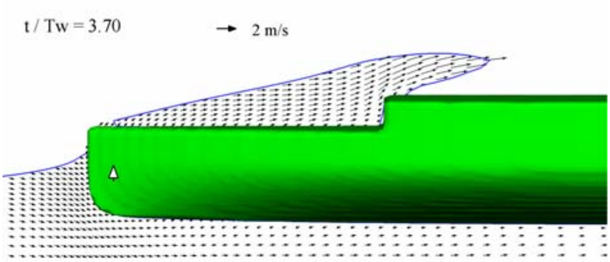
t / Tw = 3.70
2 m/s

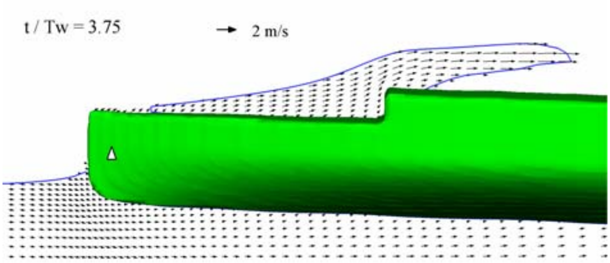
t / Tw = 3.75
2 m/s

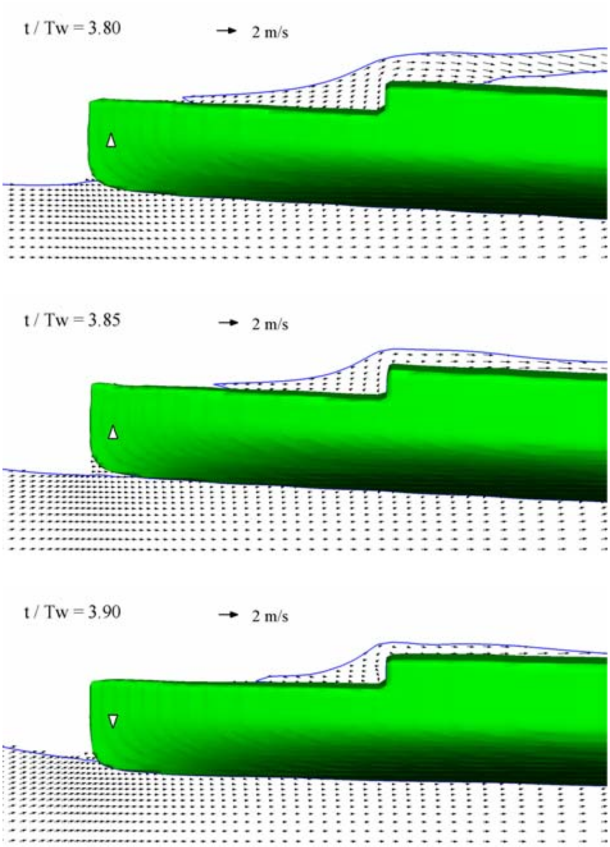

Figure 7.5 Detailed view of the flow velocities in the centre plane and at the bow of the Wigley hull in a relative frame moving with the ship speed U=0.78ms^{-1}. The magnitude of the velocities can be estimated by comparing with the reference vector representing a magnitude of 2ms^{-1}. The vertical ship velocity at the bow is also indicated. The conditions are similar to Figure 7.3. The ship length is 1m.

We note the presence of a lump of nearly stagnant water in front of the deck house at t/Tw ≤3.55. This is due to water on deck from a previous green water event. The results at t/Tw=3.60 show that the collision between the new and previous green water on deck diverts the path of the new water on deck. When the water on the deck has impacted on the deck house, it continues to move upwards. This is different from the studies by Greco (2001) and Barcellona et al. (2003), where the vertical fluid motion along the vertical wall on the deck finally stopped with the result that a backwards plunging breaker impacted on the underlying water. This phenomenon causes important loads on the deck and the deck house. This behavior is obviously a function of the deck house height, which is relatively low in our case. The water engulfs the top of the deck house as the result of a plunging breaker with a peculiar elongated shape.

Our case study has shown many new interesting flow phenomena associated with green water on deck. However, the results need to be verified and validated by experiments. For instance, the influence of grid size and the size of the computational domain should be investigated. Further, a realistic wavemaker has to be included for comparisons with experiments. This can be done as already explained in connection with our 2D Numerical Wave Tank.

CHAPTER 8

Summary and future perspectives

8.1 Summary

It has been demonstrated by extensive verification and validation tests that the 2D CIP code can in many cases adequately predict:

- The fully nonlinear free-surface deformation.
- Flow characteristics such as vorticity fields and viscous flow separations.
- The hydrodynamic loads acting on the body in the Earth-fixed Cartesian grid system in a very simple and robust way.
- The motion of the body during water entry and exit.
- The non-viscous flow separation.

On the other hand, the 2D CIP code has the following difficulties:

- The predicted force at the early stage of the impact of a circular cylinder with the free surface does not converge. This is due to the singular nature of the problem. However, the force impulse during a small initial time converges.

- To simulate the cases when the angle between the impacting wedge side and the free surface is small. A reason is that the code did not account for the air compressibility. This small relative impact angle probably causes an air cushion extending from the keel to the knuckle on the windward side.

- To apply the boundary condition at the exact location of the boundary. The interface is not explicitly tracked but is reconstructed from the field variables on an Earth-fixed grid. The location of the interface can be determined based on the volume fraction information, i.e. the density function, unavoidably resulting in an uncertainty of one grid cell. Topological changes are easy to handle, but some accuracy can be lost when details of the interface can not be covered by the grid.

- The CIP method is shown to give generally satisfactory prediction of heave added mass and damping of a nearly rectangular cross-section for linear problems. However, difficulties occur in accurately predicting drag coefficients when the heave amplitude becomes too small.

We have illustrated the capability of a 3D CIP code to predict green water phenomena. However, this needs further verification and validation.

8.2 Future perspectives

In order to make the calculation more accurate and fast, future work is needed. In particular we need to develop:

- An efficient solver for the Poisson equation. The solver for the Poisson equation used in this thesis is successive over-relaxation (SOR) which is a stationary method easy to understand and implement but quite time-consuming to reach a favorable convergent condition.

- A more accurate treatment of the body boundary condition. According to the description of the CIP method in Chapter 2, we can see that the body boundary condition is of importance to the accurate calculation of the density function φ_3 and therefore for the calculation of the hydrodynamic forces on the floating body and the motion of the body.

- An account of compressibility and local elastic deformation of the structure as a consequence of local phenomena of slamming (Faltinsen, 2000). As discussed in Chapter 5, the small relative impact angle causes probably an air cushion extending from the keel to the knuckle on the windward side. Local hydroelastic effects are important to consider at low relative impact angles (Faltinsen, 2005). This requires modeling of structural elasticity effects.

- Methods/checks for ensuring global conservation of mass, momentum and energy. Proper description of sloshing in a tank is for instance sensitive to how well liquid mass is conserved. However, the original CIP scheme has difficulty with this. In order to overcome this difficulty, establishing an exact conservative semi-Lagrangian scheme is a challenging task. Therefore, a CIP-based interface capturing method, so-called CIP-CSL3 (CIP-Conservative semi-Lagrangian scheme with 3rd-order polynomial function) scheme should be incorporated in the numerical code. Instead of the spatial derivatives in the CIP method, this scheme uses cell-integrated value as the additional constraint to construct a cubic polynomial. Because this scheme introduces a slope control parameter, the sharpness of the density function variation across the interface can be retained in the calculation. Detailed description of the scheme can be found in Xiao & Yabe (2001) and Xiao & Ikebata (2003). The biggest merit of this scheme is the good mass conservation which is beneficial to long-time computations. Hu et al. (2004) applied this scheme for violent sloshing computations.

- An account of surface tension. A continuum surface force (CSF) model (Brackbill et al., 1992) can be incorporated in the computation code to approximate the effect of surface tension, in which the surface tension is considered as a continuous, three-dimensional effect across the interface. The surface tension force is included in the body force term f_i of Eq. (2.12) as follows:

$$f_s = -\frac{\sigma_s}{\rho}\nabla \cdot \left(\frac{\nabla \varphi_1}{\left| \nabla \varphi_1 \right|} \right) \nabla \varphi_1$$

  where σ_s is the surface tension coefficient. By applying this model, no extra treatment is needed even when the interface is topologically distorted. However, the practical importance of including surface tension in full scale conditions is limited.

From the water entry study in Chapter 4, we can foresee there exists a threshold Froude number where the air cushion starts to occur. However, what the threshold Froude number should be needs future studies. Further, model tests are also required in order to validate the findings.

Appendix A Computational procedure

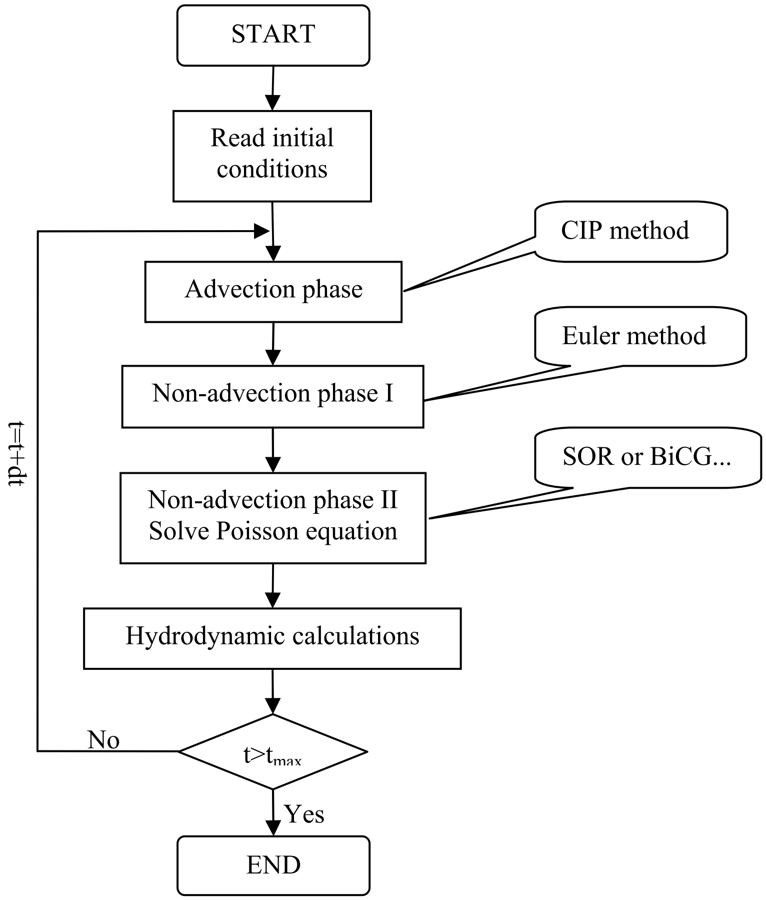

Figure A.1 Computational procedure for applying CIP to impressible flows

Figure A.1 illustrates briefly the computational procedure for applying CIP method to impressible flows. This procedure adopted in most of our computations, is proved to be very robust for incompressible multiphase computations.

References

AARSNES, J. V. (1996) Drop test with ship sections-effect of roll angle. MARINTEK, Trondheim, Norway.

AARSNES, J. V. (1997) Extreme Condition at Sea. Part II. 4: Wave forces on 2-dimensional sections in the free surface zone. MARINTEK, Trondheim, Norway.

BAARHOLM, R. J. (2001) Theoretical and experimental studies of wave impact underneath decks of offshore platforms. Dr. ing thesis. Dept. of Marine Technology, NTNU, Trondheim, Norway.

BARCELLONA, M., LANDRINI, M., GRECO, M. & FALTINSEN, O. M. (2003) An experimental investigation on bow water shipping. *J. Ship Research*, Vol. **47**, No. **4**, pp: 327-346.

BEARMAN, P. W., GRAHAM, J. M. R., OBASAJU, E. D. & DROSSOPOULOS, G. M. (1984) The influence of corner radius on the forces experienced by cylindrical bluff bodies in oscillatory flow. *Applied Ocean Research*, **6**, pp: 83-89.

BEST, J. P. (1993) The formation of toroidal bubbles upon the collapse of transient cavities. *J. Fluid Mech*., **251**, pp: 79-107.

BRAATHEN, A. (1987) Application of a vortex tracking method to the prediction of roll damping of a two-dimensional floating body. Ph. D thesis, Dept. of Marine Hydrodynamics, NTNU, Trondheim, Norway.

BRACKBILL, J. U., KOTHE, D. B. & ZEMACH, C. (1992) A continuum method for modeling surface tension. *Journal of Computational Physics*, **100**, pp: 335-354.

BUCHNER, B. (1995a) The impact of green water on FPSO design. *OTC paper 7698*, OTC1995, Houston.

BUCHNER, B. (1995b) On the impact of green water loading on ship and offshore unit design. *PRADS'95*, Seoul.

BUCHNER, B. (2002) Green water on ship-type offshore structure. Ph. D thesis. Technische Universiteit Delft. Netherlands.

CAMPBELL, I. M. C. & WEYNBERG, P. A. (1980) Measurement of parameters affecting slamming. Final Report, Rep. No. 440, *Technology Reports Center No. OT-R-8042*. Southampton University: Wolfson Unit for Marine Technology.

CHEZHIAN, M. (2003) Three-dimensional analysis of slamming. Dr.ing thesis. Dept. of Marine Technology, NTNU, Trondheim, Norway.

CHRISTAKIS, N. , CROFT, T. N. & PATEL, M. K. (2002) A new unstructured algorithm based on the Volume of Fluid method for tracking material interfaces in a finite-volume framework, In: R. Herbin & D. Kroner (Eds) *Finite Volumes for Complex Applications III* (Third International Symposium on Finite Volumes for Complex Applications , Porquerolles, France), pp: 487-494, Hermes Penton Ltd.. London UK.

COLICCHIO, G., GRECO, M. & FALTINSEN, O. M. (2005) A BEM-Level Set Domain Composition Strategy for nonlinear and fragmented interfacial flows. Submitted for publication.

ENRIGHT, D., FEDKIW, R., FERZIGER, J. & MITCHELL, I. (2002) A hybrid particle level set method for improved interface capturing. *J. Comp. Phys.*, **183**, pp: 83-116.

ERSDAL, G. & KVITRUD, A. (2000) Green water on Norwegian production ships. Proceedings of the International Offshore and Polar Engineering Conference, Vol. **1**, pp. 211-218.

FADLUN, E. A., VERZICCO, R., ORLANDI, P. & MOHD-YUSOF, J. (2000) Combined immersed boundary finite difference methods for three dimensional complex flow simulations. *J. Comp. Phys.*, **161**, pp: 30-60.

FALTINSEN, O. M. (1990) *Sea Loads on Ships and Offshore Structures*. Cambridge, England: Cambridge University Press.

FALTINSEN, O. M. (2000) Hydroelastic slamming, *J. Marine Science and Technology* 5 (2).

FALTINSEN, O. M. (2005) *Hydrodynamics of High-Speed Marine Vehicles.* New York: Cambridge University Press.

FALTINSEN, O. M., ROGNEBAKKE, O. F., LUKOVSKY, I. A. & TIMOKHA, A. N. (2000) Multidimensional modal analysis of nonlinear sloshing in rectangular tank with finite water depth. *J. Fluid Mech.*, **407**, pp.201-234.

FALTINSEN, O. M. & TIMOKHA, A. N. (2001) Adaptive multimodal approach to nonlinear sloshing in a rectangular tank. *J. Fluid Mech.*, Vol. **432**, pp. 167-200.

FALTINSEN, O. M. & TIMOKHA, A. N. (2002) Asymptotic modal approximation of nonlinear resonant sloshing in a rectangular tank with small water depth. *J. Fluid Mech.*, Vol. **470**, pp. 319-357.

FALTINSEN, O. M., ROGNEBAKKE, O. F. & TIMOKHA, A. N. (2003) Resonant three-dimensional nonlinear sloshing in a square base basin. *J. Fluid Mech.*, **487**, pp. 1-42.

FALTINSEN, O. M., ROGNEBAKKE, O. F. & TIMOKHA, A. N. (2005) Resonant three-dimensional nonlinear sloshing in a square base basin, II: Effect of higher modes. *J. Fluid Mech.*, **523**, pp. 199-218.

FALTINSEN, O. M., ROGNEBAKKE, O. F. & TIMOKHA, A. N. (2005a) Classification, simulation and validation of three-dimensional nonlinear sloshing in a squared-base tank with finite depth. *J. Fluids and Structures*, **20**, **1**, pp. 81-103.

FALTINSEN, O. M., ZHU, X. Y. & HU, C. -H. (2005b) Strongly nonlinear flows in seakeeping. Keynote lecture, ICMRT'05, Naples, Italy.

FEKKEN, G. (2004) Numerical Simulation of Free-Surface Flow with Moving Rigid Bodies. Ph.D thesis. The faculty of Mathematics and Natural Sciences, University of Groningen.

GERRITS, J. (2001) Dynamics of fluid-filled spacecraft. Ph. D thesis, University of Groningen, The Netherland.

GINGOLD, R. A. & MONAGHAN, J. J. (1977) Smoothed particle hydrodynamics: theory and application to non-spherical stars. Monthly notices of the Royal Astronomical Society, Vol. **181**, pp: 375-389

GRAHAM, J. M. R. (1980) The forces on sharp-edged cylinder in oscillatory flow at low Keulegan-Carpenter numbers. *J. Fluid Mech.*, **97**, pp: 331-346.

GRECO, M. (2001) A two-dimensional study of green-water loading. Ph. D thesis, Dept. of Marine Hydrodynamics, NTNU, Trondheim, Norway.

GREENHOW, M. & LIN, W. M. (1983) Nonlinear free-surface effects: experiments and theory. Report, MIT, Department of Ocean Engineering, Cambridge, USA, pp. 83-119.

GREENHOW, M. & MOYO, S. (1997) Water entry and exit of a horizontal circular cylinders. *Phil. Trans. R. Soc. Lond. A.,* **355**, pp: 551-563

HIRT, C. W. & NICHOLS, B. D. (1981) Volume Of Fluid (VOF) Method for the Dynamics of Free boundaries. *J. Comput. Phys*., Vol. **39**, No. **1**, pp: 201-225.

HU, C.-H & KASHIWAGI, M. (2004) A CIP-based method for numerical simulation of violent free-surface flows. *J. Mar Sci Tecnol.* Vol. **9**, No. **4**, pp. 143-157.

HU, C.-H, FALTINSEN, O. M. & KASHIWAGI, M. (2004) Development and Validation of CIP based Cartesian Grid Mehtod for Nonlinear Wave-Body Interactions. 7th Numerical Towing Tank Symposium, Hamburg, Germany.

HU, C.-H, FALTINSEN, O. M. & KASAWAGI, M. (2005). 3-D Numerical simulation of freely moving floating body by CIP method. ISOPE, June 19-24, Seoul, Korea.

HU, C.-H (2005) *CIP method*. Lecture Note for MR8300 Hydrodynamic aspects of marine structures 1 at the Department of Marine Technology, NTNU, Trondheim, Norway.

HU, C.-H, KASHIWAGI, M. & KISHEV, Z. (2004) Numerical simulation of violent sloshing by CIP method. Proc. 19th International Workshop on Water Waves and Floating Bodies, Cortona, Italy, pp. 67-70.

JAMES, A. J. & LOWENGRUB, J. (2004) A surfactant-conserving volume-of-fluid method for interfacial flows with insoluble surfactant. *J. of Comp. Phys*., **201**, pp: 685–722

JENSEN, J. J., BECK, R. F, DU, S., FALTINSEN, O. M., FONSECA, N., RIZZUTO, E., STREDULINSKY, D. & WATANABE, I. (2000) Extreme hull girder loading. ISSC, Nagasaki, Japan.

JONG, B. DE (1967) Berekening van de hydrodynamische coëfficiënten van oscillerende cylinders. Report no. 174 of the Shipbuilding Laboratory, Technological University Delft.

JONG, B. DE (1973) Computation of the hydrodynamic coefficients of oscillating cylinders. Report no. 145S/174A of the Shipbuilding Laboratory, Delft University of Technology.

JUDGE, C., TROESCH, A. & PERLIN, M. (2004) Initial water impact of a wedge at vertical and oblique angles. *J. Eng. Math*., **48**, pp.279-303.

KARNI, S. (1994) Multicomponent flow calculations by a consistent primitive algorithm. *J. Comput. Phys*., **112**, 31.

KAWASAKI, J. (2005) Numerical Model of 2-D Multiphase Flow with Solid-Liquid-Gas Interaction. *International Journal of Offshore and Polar Engineering* (ISSN 1053-5381), Vol. **15**, No. 3, pp: 198-203.

KEULEGAN, G. H. & CARPENTER, L. H. (1958) Forces on cylinders and plates in an oscillating fluid. *J. Res. National Bureau of Standards*. **60**, 5, pp: 423-440.

KIM, Y. (2000) Numerical analysis of sloshing problem. 15th International Workshop on Water Waves and Floating Bodies, Dan Caesarea, Israel.

KLEEFSMAN, K. M. Theresa, FEKKEN, G., VELDMAN, Arthur E.P. & IWANOWSKI, B. (2004) Improved Volume-of-Fluid Method for Wave Impact Problems, ISOPE 2004, pp: 334-341.

KOEHLER, B. R. & KETTLEBOROUGH (1977) Hydrodynamics of a falling body upon a viscous impressible fluid. *J. Ship Res*., **20**, pp.190-198.

LAFAURIE, B., NARDONE, C., SCARDOVELLI, R., ZALESKI, S. AND ZANETTI, G. (1994) Modelling Merging and Fragmentation in Multiphase Flows with SURFER. *J. Comp. Phys.* **113**, pp: 134-147.

LANDRINI, M. (2003) Strongly nonlinear phenomena in ship hydrodynamics. Weinblum Lecture. To be published in Journal of Ship Research.

LANDRINI, M., CALAGROSSI, A. & FALTINSEN, O. M. (2003) Sloshing and slamming in 2-D flows by the SPH Method. 8th Int. Conf. on Num. Ship Hydrodynamics, Busan, Korea.

LEONARD, B.P. (1979) A stable and accurate convective modelling procedure based on quadratic upstream interpolation. *Comp. Math. in Appl. Mech. and Engrng*., Vol. **19**, pp: 59-98.

LUCY, L. (1977) A numerical approach to the testing of the fission hypothesis. *Astronomical Journal*, Vol. **82**, pp: 1013-1024.

LUGNI, C., COLAGROSSI, A., LANDRINI, M. & FALTINSEN, O. M. (2004) Numerical and experimental investigations on semi-displacement monohull and catamaran in calm water and incident waves. 25th Symp. on Naval Hydrodynamics, St. John's, Canada.

LUGT, H. J. (1983) Vortex flow in nature and technology. John Wiley and Sons.

MARONNIER, V., PICASSO, M. & RAPPAZ, J. (1999) Numerical simulation of free surface flows. *J. Computational Physics*, **155**, pp: 439-455.

MEYERHOFF, W. K. (1970) Added mass of thin rectangular plates calculated from potential theory. *Journal of Ship Research*, pp: 100-110.

MIAO, G. (1989) Hydrodynamic forces and dynamic responses of circular cylinders in wave zones. Dr. ing thesis, Dept. of Marine Hydrodynamics, NTH, Trondheim, Norway.

MONAGHAN, J. J (1988) An introduction to SPH. *Computer Physics Communications*, Vol. **48**, No. **1**, pp: 89-96.

MONAGHAN, J. J. (1994) Simulating free surface flows with SPH. *J. Comp. Phys.,* **110**, pp: 399-406.

MONAGHAN, J. J. & KOS, A. (1999) Solitary waves on a Cretan Beach. *J. Waterway, Port, Coastal, and Ocean Engrg*, ASCE, **125**, **3**.

MONAGHAN, J. J., KOS, S. & ISSA, N. (2003) Fluid Motion Generated by Impact. *J. Waterway, Port, Coastal, and Ocean Engrg*, ASCE, **129**, **6**, pp: 250-259.

MORISON, J. R., O'BRIEN, M. P., JOHNSON, J. W. & SCHAAF, S. A. (1950) The force exerted by surface waves on piles. *Pet. Trans*., **189**, pp: 149-154.

MOYO, S. & GREENHOW, M. (2000) Free motion of a cylinder moving below and through a free surface. *Applied Ocean Research* **22**, pp.31-44.

MOYO S. (1996) Hydrodynamic interaction of horizontal circular cylinders with a free surface. PhD thesis, Department of Mathematics and Statistics, Brunel University, London, UK

MUTHU, C. (2003) Three-dimensional analysis of slamming. Ph. D thesis. Department of Marine Technology, NTNU, Trondheim, Norway.

NEWMAN, J. N. (1977) *Marine Hydrodynamics*. Cambridge: The MIT Press.

NEWMAN, J. N. & SCLAVOUNOS, P. (1981) The unified theory of ship motions. 13th Symp. On Naval Hydrodynamics, Tokyo, Japan: The Shipbuilding Research Association of Japan.

NICHOLS, B. D., HIRT, C. W. & HOTCHKISS, R. S. (1980) SOLA-VOF: A solution algorithm for transient fluid flow with multiple free boundaries. Los Alamos National Lab Report LA-8355.

NIELSEN, K. B. (2003) Numerical Prediction of Green Water Loads on Ships. Ph. D thesis. Department of Mechanical Engineering, Technical University of Denmark.

OSHER, S. (2002) Dynamic Visibility and the Level Set Method, *SIAM News*, Vol. **35**, No. **4**.

OSHER, S. & FEDKIW, R. (2001) Level Set Methods: An Overview and Some Recent Results. *J. Comp. Phys.,* **169**, 463–502.

OSHER, S. & FEDKIW, R. (2002) *The Level Set Method and Dynamic Implicit Surfaces*. Springer-Verlag, New York.

OSHER, S. & SETHIAN, J. A. (1988) Fronts propagating with curvature dependent speed: algorithms based on Hamilton–Jacobi formulations. *J. Comput. Phys.*, **79**, pp: 12-49.

PATANKAR, S. V. & SPALDING, D. B. (1972) A calculation procedure for heat, mass and momentum transfer in three-dimensional parabolic flows. *Int. J. Heat Mass Transfer*, Vol. **15**, pp: 1787.

RITTER, A. (1892) *Die fortpflanzung der wasserwellen*, Volume **36**, Z. Ver. Deut. Ing.

ROGERS, B. D., DALRYMPLE, R. A. D., KNIO, O. & GESTERIAM, M. (2003) Smoothed Particle Hydrodynamics for naval hydrodynamics. 18th International Workshop on Water Waves & Floating Bodies (IWWWFB), Le Croisic, France.

ROGNEBAKKE, O. F. & FALTINSEN, O. M. (2005) Sloshing induced impact with air cavity in rectangular tank with a high filling ratio. 20th Int. Workshop on Water Waves and Floating Bodies, Longyearbyen, Spitsbergen.

RUDMAN, M. (1997) Volume-tracking methods for interfacial flow calculations*. Int. J. Numerical Methods Fluids*, **24**, pp: 671-691.

RUSSO, G. & SMEREKA, P. (2000) A Remark on Computing Distance Functions. *J. Comput. Phys*., **163**, pp: 51–67.

SARPKAYA, T. (1966) Separated flow about lifting bodies and impulsive flow about cylinders, *AIAA Jour*., **44**, 414-20.

SCHLICHTING, H. (1979) *Boundary-Layer Theory*. New York: McGraw-Hill Book Company.

SETHIAN, J. (1999) *Level Set Methods and Fast Marching Methods*. Cambridge University Press.

SETHIAN, J. (2001) Evolution, Implementation, and Application of Level Set and Fast Marching Methods for Advancing Fronts. *J. Comp. Phys*., **169**, pp: 503–555.

SUN, H. (2004) Solution of exercises in the book "*Hydrodynamics of High-Speed Marine Vehicles*" by Prof. O. Faltinsen. Centre for Ships and Ocean Structures, NTNU, Trondheim, Norway.

SUSSMAN, M., SMEREKA, P. AND OSHER, S. (1994) A Level Set Approach for Computing Solutions to Incompressible Two-Phase Flow. *J. Comp. Phys.* **114**, pp: 146-159.

TAKEWAKI, H., NISHIGUCHI, A. & YABE, T. (1985) The cubic-interpolated pseudo-particle (CIP) method for solving hyperbolic-type equations. *J. Comput. Phys.*, **61**, 261.

TAKEWAKI, H. & YABE, T. (1987) Cubic-interpolated pseudo-particle (CIP) method-application to nonlinear or multi-dimensional problems. *J. Comput. Phys.*, **70**, 355.

TAYLAN, M. (2003) Static and dynamic aspects of a capsize phenomenon. Ocean Engineering **30** (2003), pp: 331-350.

TULIN, M. P. & LANDRINI, M. (2000) Breaking waves in the Ocean and around Ships. Proc. 23rd ONR Symposium on Naval Hydrodynamics, Val de Reuil, France.

TYVAND, P. A. & MILOH, T. (1995a) Free-surface flow due to implusive motion of a submerged circular cylinder. *J. Fluid Mech.*, **286**, pp: 67-101.

TYVAND, P. A. & MILOH, T. (1995b) Free-surface flow generated by a small submerged circular cylinder starting from rest. *J. Fluid Mech.*, **286**, pp: 103-116.

URSELL, F. (1949) On the heaving motion of a circular cylinder on the free surface of a fluid. *Quarterly Journal of Mechanics and Applied Mathematics II* (2), pp: 218-231.

VORST, H. A. (1992) Bi-CGSTAB: A fast and smoothly converging variant of Bi-CG for the solution of nonsymmetric linear system. *SIAM J. Sci. Statist. Comput.*, **13**, 631.

VUGTS, J.H. (1968) The hydrodynamic coefficients for swaying, heaving and rolling cylinder in free surface. Netherlands Ship Research Center TNO, Report 112s, May 1968.

WAGNER, H.(1932) Über Stoss- und Gleitvorgänge an der Oberfläche von Flüssigkeiten. *Zeitschr. f. Angewandte Mathematik und Mechanik,* **12**, 4, pp. 193-235.

WALTON, P. (1986) Ph.D. thesis. University of Manchester.

WHITE, F. M. (1974) *Viscous Fluid Flow*. New York: McGraw-Hill Book Company.

WILLIAMS, M., KOTHE, D. AND PUCKETT, E. (1999a) Approximating Interfacial Topologies with Applications for Interface Tracking Algorithms. 37th AAIA Aerospace Sciences Meeting, 99-1076.

WILLIAMS, M., KOTHE, D. AND PUCKETT, E. (1999b) Convergence and Accuracy of Kernel-Based Continuum Surface Tension Models. Shyy, W., ed., Cambridge University Press: Fluid Dynamics at Interfaces, pp. 347-356.

XIAO F. (2001) Implementations of multi-fluid hydrodynamic simulations on distributed memory computer with a fully parallelizable preconditioned Bi-CGSTAB method. *Computer Physics Communications,* **137**, pp: 274–285.

XIAO, F & YABE, T. (2001) Completely Conservative and Oscillation-less Semi-Lagrangian Schemes for Advection Transportation. *J. Compu. Phys.*, **170**, pp: 498-522.

XIAO, F. & IKEBATA A. (2003) An efficient method for capturing free boundaries in multi-fluid simulations. *Int. J. Numer. Math. Fluids*, **42**, pp: 187-210.

XING-KAEDING, Y., JENSEN, G. & PERIC, M. (2004) Numerical simulation of water-entry and water-exit of a horizontal circular cylinder. Hydrodynamics VI - Theory and Application, A. A. Balkema Publisher, pp. 663-669.

YABE, T. & AOKI, T. (1991) A universal solver for hyperbolic-equations by cubic-polynomial interpolation. I. One-dimensional solver. *Comput. Phys. Commun.*, **66**, 219.

YABE, T., ISHIKAWA, T., WANG, P. Y., AOKI, T., KADOTA, Y. & IKEDA, F. (1991) A universal solver for hyperbolic-equations by cubic- polynomial interpolation. II. Two- and three-dimensional solvers. *Comput. Phys. Commun.*, **66**, 233.

YABE, T. & TAKEI, E. (1988) A new higher-order Godunov method for general hyperbolic equations. *J. Phys. Soc. Japan,* **57**, 2598.

YABE, T., XIAO, F. & UTSUMI, T. (2001) The Constrained Interpolation Profile Method for Multiphase Analysis. *Journal of Computational Physics*, **169**, pp: 556-593.

YAMAMOTO, Y., IIDA, K., FUKASAWA, T., MURATAMI, T. ARAI, M. & ANDO, M. (1985) Structural damage analysis of a fast ship due to bow flare slamming. *International Shipbuilding Progress*, **32**, 369, pp.124-136.

ZHAO, R., FALTINSEN, O. M. & AANESLAND, V. (1988) Wave-current interaction effects on large-volume structures. Proceedings of the International Conference on Behavior of Offshore Structures (BOSS'88), Trondheim, Norway, pp. 623-638.

ZHAO, R. & FALTINSEN, O. M. (1993) Water entry of two-dimensional bodies. *J. Fluid Mech*. **246**, pp. 593-612.

ZHAO, R., FALTINSEN, O.M. & AARSNES, J.V. (1996) Water entry of arbitrary two-dimensional sections with and without flow separation. 21st Symposium on Naval Hydrodynamics, Trondheim, Norway.

ZHU, X. Y., FALTINSEN, O. M. & HU, C. H. (2005a) Water entry and exit of a circular cylinder. Proceedings of 24th International Conference on Offshore Mechanics and Arctic Engineering (OMAE), Halkidiki, Greece. (Accepted by Journal of OMAE)

ZHU, X. Y., FALTINSEN, O. M. & HU, C. H. (2005b) Water entry forces on heeled ship sections. Proceedings of 16th International Conference on Hydrodynamics in Ship Design, Gdansk, Poland.

Previous reports published at the Institute of Marine Technology (previously: Faculty of Marine Technology) Norwegian University of Science and Technology

UR-79-01 Brigt Hatlestad, MK:	The finite element method used in a fatigue evaluation of fixed offshore platforms. (Dr.Ing. Thesis)
UR-79-02 Erik Pettersen, MK:	Analysis and design of celluar structures. (Dr.Ing. Thesis)
UR-79-03 Sverre Valsgård, MK:	Finite difference and finite element methods applied to nonlinear analysis of plated structures. (Dr.Ing. Thesis)
UR-79-04 Nils T. Nordsve, MK:	Finite element collapse analysis of structural members considering imperfections and stresses due to fabrication. (Dr.Ing. Thesis)
UR-79-05 Ivar J.Fylling, MK:	Analysis of towline forces in ocean towing systems. (Dr.Ing. Thesis)
UR-80-06 Nils Sandsmark, MM:	Analysis of Stationary and Transient Heat Conduction by the Use of the Finite Element Method. (Dr.Ing. Thesis)
UR-80-09 Sverre Haver, MK:	Analysis of uncertainties related to the stochastic modeling. Three-Dimensional Flow Past Lifting Surfaces and Blunt Bodies. (Dr.Ing. Thesis)
UR-85-46 Alf G. Engseth, MK:	Finite element collapse analysis of turbular steel offshore structures. (Dr.Ing. Thesis)
UR-86-47 Dengody Sheshappa, MP:	A Computer Design Model for Optimizing Fishing Vessel Designs Based on Techno-Economic Analysis. (Dr.Ing. Thesis)
UR-86-48 Vidar Aanesland, MH:	A Theoretical and Numerical Study of Ship Wave Resistance. (Dr.Ing. Thesis)
UR-86-49 Heinz-Joachim Wessel, MK:	Fracture Mechanics Analysis of Crack Growth in Plate Girders. (Dr.Ing. Thesis)

UR-86-50 Jon Taby, MK:	Ultimate and Post-ultimate Strength of Dented Tubular Members. (Dr.Ing. Thesis)
UR-86-51 Walter Lian, MH:	A Numerical Study of Two-Dimensional Separated Flow Past Bluff Bodies at Moderate KC-Numbers. (Dr.Ing. Thesis)
UR-86-52 Bjørn Sortland, MH:	Force Measurements in Oscillating Flow on Ship Sections and Circular Cylinders in a U-Tube Water Tank. (Dr.Ing. Thesis)
UR-86-53 Kurt Strand, MM:	A System Dynamic Approach to One-dimensional Fluid Flow. (Dr.Ing. Thesis)
UR-86-54 Arne Edvin Løken, MH:	Three Dimensional Second Order Hydrodynamic Effects on Ocean Structures in Waves. (Dr.Ing. Thesis)
UR-86-55 Sigurd Falch, MH:	A Numerical Study of Slamming of Two-Dimensional Bodies. (Dr.Ing. Thesis)
UR-87-56 Arne Braathen, MH:	Application of a Vortex Tracking Method to the Prediction of Roll Damping of a Two-Dimension Floating Body. (Dr.Ing. Thesis)
UR-87-57 Bernt Leira, MR:	Caussian Vector Processes for Reliability Analysis involving Wave-Induced Load Effects. (Dr.Ing. Thesis)
UR-87-58 Magnus Småvik, MM:	Thermal Load and Process Characteristics in a Two-Stroke Diesel Engine with Thermal Barriers (in Norwegian) (Dr.Ing. Thesis)
MTA-88-59 Bernt Arild Bremdal, MP:	An Investigation of Marine Installation Processes - A Knowledge-Based Planning Approach. (Dr.Ing. Thesis)
MTA-88-60 Xu Jun, MK:	Non-linear Dynamic Analysis of Space-framed Offshore Structures. (Dr.Ing. Thesis)
MTA-89-61 Gang Miao, MH:	Hydrodynamic Forces and Dynamic Responses of Circular Cylinders in Wave Zones. (Dr.Ing. Thesis)

MTA-89-62 Martin Greenhow, MH: Linear and Non-Linear Studies of Waves and Floating Bodies. Part I and Part II. (Dr.Techn. Thesis)

MTA-89-63 Chang Li, MH: Force Coefficients of Spheres and Cubes in Oscillatory Flow with and without Current. (Dr.Ing. Thesis)

MTA-89-64 Hu Ying, MP: A Study of Marketing and Design in Development of Marine Transport Systems. (Dr.Ing. Thesis)

MTA-89-65 Arild Jæger, MH: Seakeeping, Dynamic Stability and Performance of a Wedge Shaped Planing Hull. (Dr.Ing. Thesis)

MTA-89-66 Chan Siu Hung, MM: The dynamic characteristics of tilting-pad bearings.

MTA-89-67 Kim Wikstrøm, MP: Analysis av projekteringen för ett offshore projekt. (Licenciat-avhandl.)

MTA-89-68 Jiao Guoyang, MR: Reliability Analysis of Crack Growth under Random Loading, considering Model Updating. (Dr.Ing. Thesis)

MTA-89-69 Arnt Olufsen, MK: Uncertainty and Reliability Analysis of Fixed Offshore Structures. (Dr.Ing. Thesis)

MTA-89-70 Wu Yu-Lin, MR: System Reliability Analyses of Offshore Structures using improved Truss and Beam Models. (Dr.Ing. Thesis)

MTA-90-71 Jan Roger Hoff, MH: Three-dimensional Green function of a vessel with forward speed in waves. (Dr.Ing. Thesis)

MTA-90-72 Rong Zhao, MH: Slow-Drift Motions of a Moored Two-Dimensional Body in Irregular Waves. (Dr.Ing. Thesis)

MTA-90-73 Atle Minsaas, MP: Economical Risk Analysis. (Dr.Ing. Thesis)

MTA-90-74 Knut-Aril Farnes, MK: Long-term Statistics of Response in Non-linear Marine Structures. (Dr.Ing. Thesis)

MTA-90-75 Torbjprn Sotberg, MK: Application of Reliability Methods for Safety Assessment of Submarine Pipelines. (Dr.Ing. Thesis)

MTA-90-76 Zeuthen, Steffen, MP: SEAMAID. A computional model of the design process in a constraint-based logic programming environment. An example from the offshore domain. (Dr.Ing. Thesis)

MTA-91-77 Haagensen, Sven, MM: Fuel Dependant Cyclic Variability in a Spark Ignition Engine - An Optical Approach. (Dr.Ing. Thesis)

MTA-91-78 Løland, Geir, MH: Current forces on and flow through fish farms. (Dr.Ing. Thesis)

MTA-91-79 Hoen, Christopher, MK: System Identification of Structures Excited by Stochastic Load Processes. (Dr.Ing. Thesis)

MTA-91-80 Haugen, Stein, MK: Probabilistic Evaluation of Frequency of Collision between Ships and Offshore Platforms. (Dr.Ing. Thesis)

MTA-91-81 Sødahl, Nils, MK: Methods for Design and Analysis of Flexible Risers. (Dr.Ing. Thesis)

MTA-91-82 Ormberg, Harald, MK: Non-linear Response Analysis of Floating Fish Farm Systems. (Dr.Ing. Thesis)

MTA-91-83 Marley, Mark J., MK: Time Variant Reliability Under Fatigue

MTA-91-79 Hoen, Christopher, MK: System Identification of Structures Excited by Stochastic Load Processes. (Dr.Ing. Thesis)

MTA-91-80 Haugen, Stein, MR: Probabilistic Evaluation of Frequency of Collision between Ships and Offshore Platforms. (Dr.Ing. Thesis)

MTA-91-81 Sødahl, Nils, MK: Methods for Design and Analysis of Flexible Risers. (Dr.Ing. Thesis)

MTA-91-82 Ormberg, Harald, MK: Non-linear Response Analysis of Floating Fish Farm Systems. (Dr.Ing. Thesis)

MTA-91-83 Marley, Mark J., MK: Time Variant Reliability Under Fatigue Degradation. (Dr.Ing. Thesis)

MTA-91-84 Krokstad, Jørgen R., MH:	Second-order Loads in Multidirectional Seas. (Dr.Ing. Thesis)
MTA-91-85 Molteberg, Gunnar A., MM:	The application of system identification techniques to Performance Monitoring of four stroke turbocharged Diesel Engines. (Dr.Ing. Thesis)
MTA-92-86 Mørch, Hans Jørgen Bjelke, MH:	Aspects of Hydrofoil Design; with Emphasis on Hydrofoil Interaction in Calm Water. (Dr.Ing. Thesis)
MTA-92-87 Chan Siu Hung, MM:	Nonlinear Analysis of Rotordynamic Instabilities in High-speed Turbomachinery. (Dr.Ing. Thesis)
MTA-92-88 Bessason, Bjarni, MK:	Assessment of Earthquake Loading and Response of Seismically Isolated Bridges. (Dr.Ing. Thesis)
MTA-92-89 Langli, Geir, MP:	Improving Operational Safety through Exploitation of Design Knowledge - an investigation of offfshore platform safety. (Dr.Ing. Thesis)
MTA-92-90 Sævik, Svein, MK:	On Stresses and Fatigue in Flexible Pipes. (Dr.Ing. Thesis)
MTA-92-91 Ask, Tor Ø., MM:	Ignition and Flame Growth in Lean Gas-Air Mixtures. An Experimental Study with a Schlieren System. (Dr.Ing. Thesis)
MTA-86-92 Hessen, Gunnar, MK:	Fracture Mechanics Analysis of Stiffened Tubular Members. (Dr.Ing. Thesis)
MTA-93-93 Steinebach, Christian, MM:	Knowledge Based Systems for Diagnosis of Rotating Machinery. (Dr.Ing. Thesis)
MTA-93-94 Dalane, Jan Inge, MK:	System Reliability in Design and Maintenance of Fixed Offshore Structures. (Dr.Ing. Thesis)
MTA-93-95 Steen, Sverre, MH:	Cobblestone Effect on SES. (Dr.Ing. Thesis)
MTA-93-96 Karunakaran, Daniel, MK:	Nonlinear Dynamic Response and Reliability Analysis of Drag-dominated Offshore Platforms. (Dr.Ing. Thesis)

MTA-93-97 Hagen, Arnulf, MP:	The Framework of a Design Process Language. (Dr.Ing. Thesis)
MTA-93-98 Nordrik, Rune, MM:	Investigation of Spark Ignition and Autoignition in Methane and Air Using Computational Fluid Dynamics and Chemical Reaction Kinetics. A Numerical Study of Ignition Processes in Internal Combustion Engines. (Dr.Ing. Thesis)
MTA-94-99 Passano, Elizabeth, MK:	Efficient Analysis of Nonlinear Slender Marine Structures. (Dr.Ing. Thesis)
MTA-94-100 Kvålsvold, Jan, MH:	Hydroelastic Modelling of Wetdeck Slamming on Multihull Vessels. (Dr.Ing. Thesis)
MTA-94-101	(Dr.Ing. Thesis) *Ikke godkjent.*
MTA-94-102 Bech, Sidsel M., MK:	Experimental and Numerical Determination of Stiffness and Strength of GRP/PVC Sandwich Structures. (Dr.Ing. Thesis)
MTA-95-103 Paulsen, Hallvard, MM:	A Study of Transient Jet and Spray using a Schlieren Method and Digital Image Processing. (Dr.Ing. Thesis)
MTA-95-104 Hovde, Geir Olav, MK:	Fatigue and Overload Reliability of Offshore Structural Systems, Considering the Effect of Inspection and Repair. (Dr.Ing. Thesis)
MTA-95-105 Wang, Xiaozhi, MK:	Reliability Analysis of Production Ships with Emphasis on Load Combination and Ultimate Strength. (Dr.Ing. Thesis)
MTA-95-106 Ulstein, Tore, MH:	Nonlinear Effects of a Flexible Stern Seal Bag on Cobblestone Oscillations of an SES. (Dr.Ing. Thesis)
MTA-95-107 Solaas, Frøydis, MH:	Analytical and Numerical Studies of Sloshing in Tanks. (Dr.Ing. Thesis)
MTA-95-108 Hellan, øyvind, MK:	Nonlinear Pushover and Cyclic Analyses in Ultimate Limit State Design and Reassessment of Tubular Steel Offshore Structures. (Dr.Ing. Thesis)

MTA-95-109 Hermundstad, Ole A., MK: Theoretical and Experimental Hydroelastic Analysis of High Speed Vessels. (Dr.Ing. Thesis)

MTA-96-110 Bratland, Anne K., MH: Wave-Current Interaction Effects on Large-Volume Bodies in Water of Finite Depth. (Dr.Ing. Thesis)

MTA-96-111 Herfjord, Kjell, MH: A Study of Two-dimensional Separated Flow by a Combination of the Finite Element Method and Navier-Stokes Equations. (Dr.Ing. Thesis)

MTA-96-112 Æsøy, Vilmar, MM: Hot Surface Assisted Compression Ignition in a Direct Injection Natural Gas Engine. (Dr.Ing. Thesis)

MTA-96-113 Eknes, Monika L., MK: Escalation Scenarios Initiated by Gas Explosions on Offshore Installations. (Dr.Ing. Thesis)

MTA-96-114 Erikstad, Stein O.,MP: A Decision Support Model for Preliminary Ship Design. (Dr.Ing. Thesis)

MTA-96-115 Pedersen, Egil, MH: A Nautical Study of Towed Marine Seismic Streamer Cable Configurations. (Dr.Ing. Thesis)

MTA-97-116 Moksnes, Paul O., MM: Modeling Two-Phase Thermo-Fluid Systems Using Bond Graphs. (Dr.Ing. Thesis)

MTA-97-117 Halse, Karl H., MK: On Vortex Shedding and Prediction of Vortex-Induced Vibrations of Circular Cylinders. (Dr.Ing. Thesis)

MTA-97-118 Igland, Ragnar T., MK: A Thesis Submitted in Partial Fulfilment of the Requirements for the Degree of "Doktor Ingeniør". (Dr.Ing. Thesis)

MTA-97-119 Pedersen, Hans-P., MP: Levendefiskteknologi for fiskefartøy. (Dr.Ing. Thesis)

MTA-98-120 Vikestad, Kyrre, MK: Multi-Frequency Response of a Cylinder Subjected to Vortex Shedding and Support Motions. (Dr.Ing. Thesis)

MTA-98-121 Azadi, Mohammad R.E., MK: Analysis of Static and Dynamic Pile-Soil-Jacket Behaviour. (Dr.Ing. Thesis)

MTA-98-122 Ulltang, Terje, MP:	A Communication Model for Product Information. (Dr.Ing. Thesis)
MTA-98-123 Torbergsen, Erik, MM:	Impeller/Diffuser Interaction Forces in Centrifugal Pumps. (Dr.Ing. Thesis)
MTA-98-124 Hansen, Edmond, MH:	A Descrete Element Model to Study Marginal Ice Zone Dynamics and the Behaviour of Vessels Moored in Broken Ice. (Dr.Ing. Thesis)
MTA-98-125 Videiro, Paulo M., MK:	Reliability Based Design of Marine Structures. (Dr.Ing. Thesis)
MTA-99-126 Mainçon, Philippe, MK:	Fatigue Reliability of Long Welds Application to Titanium Risers. (Dr.Ing. Thesis)
MTA-99-127 Haugen, Elin M., MH:	Hydroelastic Analysis of Slamming on Stiffened Plates with Application to Catamaran Wetdecks. (Dr.Ing. Thesis)
MTA-99-128 Langhelle, Nina K., MK:	Experimental Validation and Calibration of Nonlinear Finite Element Models for Use in Design of Aluminium Structures Exposed to Fire. (Dr.Ing. Thesis)
MTA-99-129 Berstad, Are J., MK:	Calculation of Fatigue Damage in Ship Structures. (Dr.Ing. Thesis)
MTA-99-130 Andersen, Trond M., MM:	Short Term Maintenance Planning. (Dr.Ing. Thesis)
MTA-99-131 Tveiten, Bård Wathne, MK:	Fatigue Assessment of Welded Aluminum Ship Details. (Dr.Ing. Thesis)
MTA-99-132 Søreide, Fredrik, MP:	Applications of underwater technology in deep water archaeology. Principles and practice. (Dr.Ing. Thesis)
MTA-99-133 Tønnessen, Rune, MH:	A Finite Element Method Applied to Unsteady Viscous Flow Around 2D Blunt Bodies With Sharp Corners. (Dr.Ing. Thesis)
MTA-99-134 Elvekrok, Dag R., MP:	Engineering Integration in Field Development Projects in the Norwegian Oil and Gas Industry. The Supplier Management of Norne. (Dr.Ing. Thesis)

MTA-99-135 Fagerholt, Kjetil, MP:	Optimeringsbaserte Metoder for Ruteplanlegging innen skipsfart. (Dr.Ing. Thesis)
MTA-99-136 Bysveen, Marie, MM:	Visualisation in Two Directions on a Dynamic Combustion Rig for Studies of Fuel Quality. (Dr.Ing. Thesis)
MTA-2000-137 Storteig, Eskild, MM:	Dynamic characteristics and leakage performance of liquid annular seals in centrifugal pumps. (Dr.Ing. Thesis)
MTA-2000-138 Sagli, Gro, MK:	Model uncertainty and simplified estimates of long term extremes of hull girder loads in ships. (Dr.Ing. Thesis)
MTA-2000-139 Tronstad, Harald, MK:	Nonlinear analysis and design of cable net structures like fishing gear based on the finite element method. (Dr.Ing. Thesis)
MTA-2000-140 Kroneberg, André, MP:	Innovation in shipping by using scenarios. (Dr.Ing. Thesis)
MTA-2000-141 Haslum, Herbjørn Alf, MH:	Simplified methods applied to nonlinear motion of spar platforms. (Dr.Ing. Thesis)
MTA-2001-142 Samdal, Ole Johan, MM:	Modelling of Degradation Mechanisms and Stressor Interaction on Static Mechanical Equipment Residual Lifetime. (Dr.Ing. Thesis)
MTA-2001-143 Baarholm, Rolf Jarle, MH:	Theoretical and experimental studies of wave impact underneath decks of offshore platforms. (Dr.Ing. Thesis)
MTA-2001-144 Wang, Lihua, MK:	Probabilistic Analysis of Nonlinear Wave-induced Loads on Ships. (Dr.Ing. Thesis)
MTA-2001-145 Kristensen, Odd H. Holt, MK:	Ultimate Capacity of Aluminium Plates under Multiple Loads, Considering HAZ Properties. (Dr.Ing. Thesis)
MTA-2001-146 Greco, Marilena, MH:	A Two-Dimensional Study of Green-Water Loading. (Dr.Ing. Thesis)

MTA-2001-147 Heggelund, Svein E., MK: Calculation of Global Design Loads and Load Effects in Large High Speed Catamarans. (Dr.Ing. Thesis)

MTA-2001-148 Babalola, Olusegun T., MK: Fatigue Strength of Titanium Risers - Defect Sensitivity. (Dr.Ing. Thesis)

MTA-2001-149 Mohammed, Abuu K., MK: Nonlinear Shell Finite Elements for Ultimate Strength and Collapse Analysis of Ship Structures. (Dr.Ing. Thesis)

MTA-2002-150 Holmedal, Lars E., MH: Wave-current interactions in the vicinity of the sea bed. (Dr.Ing. Thesis)

MTA20-02-151 Rognebakke, Olav F., MH: Sloshing in rectangular tanks and interaction with ship motions

MTA-2002-152 Lader, Pål Furset, MH: Geometry and Kinematics of Breaking Waves. (Dr.Ing. Thesis)

MTA-2002-153 Yang, Qinzheng, MH: Wash and wave resistance of ships in finite water depth. (Dr.Ing. Thesis)

MTA-2002-154 Melhus, Øyvin, MM: Utilization of VOC in Diesel Engines. Ignition and combustion of VOC released by crude oil tankers. (Dr.Ing. Thesis)

MTA-2002-155 Ronæss, Marit, MH: Wave Induced Motions of Two Ships Advancing on Parallel Course. (Dr.Ing. Thesis)

MTA-2002-156 Økland, Ole D., MK: Numerical and experimental investigation of whipping in twin hull vessels exposed to severe wet deck slamming. (Dr.Ing. Thesis)

MTA-2002-157 Ge, Chunhua, MK: Global Hydroelastic Response of Catamarans due to Wet Deck Slamming. (Dr.Ing. Thesis)

MTA-2002-158 Byklum, Eirik, MK: Nonlinear Shell Finite Elements for Ultimate Strength and Collapse Analysis of Ship Structures. (Dr.Ing. Thesis).

IMT-2003-1 Chen, Haibo, MK: Probabilistic Evaluation of FPSO-Tanker Collision in Tandem Offloading Operation. (Dr.Ing. Thesis)

IMT-2003-2 Skaugset, Kjetil Bjørn, MK	On the Suppression of Vortex Induced Vibrations of Circular Cylinders by Radial Water Jets. (Dr.Ing. Thesis)
IMT-2003-3 Chezhian, Muthu	Three-Dimensional Analysis of Slamming. (Dr.Ing. Thesis)
IMT-2003-4 Buhaug, Øyvind	Deposit Formation on cylinder Liner Surfaces in Medium Speed Engines. (Dr.Ing. Thesis)
IMT-2003-5 Tregde, Vidar	Aspects of Ship Design; Optimization of Aft Hull with Inverse Geometry Design. (Dr.Ing. Thesis)
IMT-2003-6 Wist, Hanne Therese	Statistical Properties of Successive Ocean Wave Parameters. (Dr.Ing. Thesis)
IMT-2004-7, Ransau, Samuel	Numerical Methods for Flows with Evolving Interfaces. (Dr.Ing. Thesis)
IMT-2004-8, Soma, Torkel	Blue-Chip or Sub-Standard. A data interrogation approach of identity safety characteristics of shipping organization. (Dr.Ing. Thesis)
IMT-2004-9 Ersdal, Svein	An experimental study of hydrodynamic forces on cylinders and cables in near axial flow. (Dr.Ing. Thesis)
IMT-2005-10 Brodtkorb, Per Andreas	The Probability of Occurrence of Dangerous Wave Situations at Sea.
IMT-2005-11 Yttervik, Rune	Ocean current variability in relation to offshore engineering. (Dr.Ing. Thesis)
IMT-2005-12 Fredheim, Arne	Current Forces on Net-Structures. (Dr.Ing. Thesis)
IMT-2005-13 Heggernes Kjetil	Flow around marine structures. (Dr.Ing. Thesis)
IMT-2005-14 Sébastien Fouques	Lagrangian modeling of Ocean Surface waves and Synthetic Aperture Radar wave measurements. (Dr.Ing. Thesis)
IMT-2006-15 Holm, Håvard	Numerical calculation of viscous free surface flow around Marine structures
IMT-2006-16 Bjørheim, Lars G.	Failure Assessment of Long Through Thickness Fatigue Cracks in Ship Hulls (Dr.ing. thesis)

IMT-2006-17 Hansson, Lisbeth	Safety Management for Prevention of Occupational Accidents (Dr.ing. thesis)